2016

Effect of Plastic Deformation on Friction Behaviour of Aluminum Sheets at Elevated Temperatures

Zeyuan Cui
University of Windsor

Effect of Plastic Deformation on Friction Behaviour of Aluminum Sheets at Elevated Temperatures

By

Zeyuan Cui

A Thesis
Submitted to the Faculty of Graduate Studies
through Engineering Materials
in Partial Fulfillment of the Requirements for
the Degree of Master of Applied Science at the
University of Windsor

Windsor, Ontario, Canada

2016

Effect of Plastic Deformation on Friction Behaviour of Aluminum Sheets at Elevated Temperatures

By

Zeyuan Cui

APPROVED BY:

_____

Dr. D. Green (Outside Program Reader)

Department of Mechanical, Automotive and Materials Engineering

_____

Dr. V. Stoilov (Program Reader)

Department of Mechanical, Automotive and Materials Engineering

_____

Dr. A. T. Alpas (Advisor)

Department of Mechanical, Automotive and Materials Engineering

May 19, 2016

DECLARATION OF ORIGINALITY

I hereby certify that I am the sole author of this thesis and that no part of this thesis has been published or submitted for publication whatsoever all across engineering lines.

I certify that, to the best of my knowledge, my thesis does not infringe upon anyone's copyright nor does it violate any proprietary rights and that any ideas, techniques, quotations, or any other material from the work of other people included in my thesis, published or otherwise, are fully acknowledged in accordance with the standard referencing practices. Furthermore, to the extent that I have included copyrighted materials that surpasses the bounds of fair dealing within the meaning of the Canada Copyright Act. I certify that I have obtained a written permission from the copyright owner(s) to include such material(s) in my thesis and have included copies of such copyright clearances to my appendix. I truly declare that this is a genuine copy of my thesis, including any final revisions, as approved by my thesis committee and the Graduate Studies office, and that this thesis has not been submitted for a higher degree to any other University or Institution all across the world.

ABSTRACT

This study examines the tribological behaviour of AA6061 alloy sheets at elevated temperatures including a study of the deformation mechanisms and their effects on friction behaviour. The role of the atmosphere is given particular importance when studying the surface morphology and that developed during high temperature deformation.

Friction tests were performed with an operating temperature range of 350 to 545°C, using strain rates between $1x10^{-2}$ and $4x10^{-2}s^{-1}$. The measured COF in argon was higher than that in air due to the absence of fresh oxide layer formed inside the sliding track. Junction strength tests were performed in air and argon for the AA6061 alloy. The junction strength of AA6061 in argon was higher than that measured in air as no oxide layer formed on the surface of alloy.

Deformation mechanisms were identified for AA6061. COF-deformation mechanism map established relationships between the tribological behaviour and deformation mechanisms.

DEDICATION

To my parents,

Jin Cui and Xiaohong Tang

and my grandmother

for their love, encouragement and support throughout.

ACKNOWLEDGEMENTS

My sincerest gratitude and thanks to Dr. A. T. Alpas for his dedicated supervision, valuable suggestions, guidance and patience throughout this research during M.A.Sc. at the University of Windsor.

I would also like to thank my committee members, Dr. D. Green and Dr. V. Stoilov, for their time and helpful suggestions. Technical help from Mr. A. Jenner and Mr. S. Budinsky are greatly acknowledged. Special thanks to Dr. S. Bhattacharya and Mr. O. Gali for their constant encouragement and support.

I appreciate and thank all fellow researchers at the Tribology of Materials Research Centre (TMRC) laboratory for their help, cooperation, constant support and encouragement.

TABLE OF CONTENTS

LIST OF FIGURES

CHAPTER 1 INTRODUCTION

1.1 Background

One of the most important challenges for the automotive industry is to reduce the fuel consumption along with safety improvements. These challenges can be realized by reducing the weight of body–in-white components by using lightweight materials [1]. These lightweight materials have to be processed to complex shapes, consequently, the quality of the final formed product should be high while maintaining high production rates during the forming of the alloys.

The processing of alloys, which is performed to change the shape of the workpieces, involves bulk plastic forming processes. These processes are classified into primary mechanical working processes and secondary mechanical working processes [2, 3]. The former are designed to induce significant deformation and shape changes in order to reduce an ingot to a standard shape, while the latter are performed on metal sheet products shaped by the previous stage to form a final finished shape, namely by sheet metal working processes. They include cold forming processes and hot forming processes [4]. As an important part of sheet metal hot forming process, quick plastic forming (QPF) and superplastic forming (SPF) take advantage of the metallurgical phenomenon of superplasticity to form complex and high contoured sheet metal parts [5]. During these processes the clamped sheet material is heated to a certain temperature and argon gas is applied to the back of the sheet to force a heated aluminum sheet into a certain shape by the die. Some aluminum alloys, such as aluminum-magnesium alloys have been widely used in automotive applications due to reasonable high strength, good resistance to

corrosion and suitable weldability. An attractive property of these Al-Mg alloys such as AA5083 is that they exhibit high ductility at elevated temperatures; and show a superplastic behaviour under low strain rate of about $10^{-3}s^{-1}$, where elongations in the 200-400% range can be achieved [6]. These are referred to as superplastic alloys; they possess a fine, stable grain size microstructure. Gholinia [7] studied the production of ultra-fine grain microstructures in Al-Mg alloys by conventional rolling process, and found that small second-phase particles in Al-Mg-Sc-Zr alloy stabilize the fine grain structure allowing it to be formed at high temperatures. Furthermore, good superplastic properties of the Al-Mg-Sc-Zr have been confirmed by others [8].

Hot-forming is a shaping operation that is performed at temperatures above $0.4T_M$ (where T_M is homologous temperature) of a given metal and which allows near-net forming of contoured parts [9]. It is a fast and cost effective deformation processing technique for producing lightweight structural components made of aluminum and magnesium alloys [6]. Superplastic forming (SPF) and quick plastic forming (QPF) are variants of hot forming techniques [5] and they take advantage of the superplastic properties of alloys, relying on the hot gas blowing forming process to form a heated blank into a single-sided tool with the use of pressurized air [10, 11].

SPF and QPF are quite similar; they both have a high strain rate sensitivity and occur under high forming temperatures in excess of 400^{o}C. In SPF, the materials exhibit exceptionally high tensile ductility, commonly in the range of 400 – 2000%, which provides significant design freedom. For aluminum alloys such as AA5083, SPF operates at temperature and strain rate ranges of 460 – 545 °C and 10^{-4} – 10^{-3} s^{-1} [12], respectively. QPF was developed by GM and boasts higher production volumes than SPF, this is because

SPF is performed under slow forming rates to obtain uniform final thickness distribution and occurs at temperatures ranging between 450^{o}C – 500^{o}C at strain rates of $10^{-4}s^{-1}$. The main deformation mechanism is due to grain boundary sliding. While, QPF occurs at lower temperatures and higher strain rates [5].

The success of hot forming i.e., good production rate with high workpiece quality and decreasing in maintenance cost of the tool/die surfaces lies in understanding the tribological issues occurring during the process and solving them effectively. High friction between the die and the workpiece has been observed at elevated temperatures. High friction behaviour occurring during the hot forming process is undesirable. This is accompanied by material transfer between the aluminum workpiece and the tool surface. All of these issues lead to a decrease in the quality of the final product and increase maintenance costs of the tool/die surfaces as they have to be cleaned by removing the adhered material mechanically [11]. Repeated action of the same die coming in contact with different sample blanks leads to accumulation of the transferred material on the die surface, especially in hot forming process of aluminum alloys. This is because the operating temperature for both SPF and QPF is higher than 400^{o}C where the aluminum alloys are relatively soft [13]. Adhered material transferred from the blank to the die would result in surface imperfections that reduce the surface quality.

The chemical composition and the mechanical behaviour of the surface layer on the forming material and the contacting tool determine the tribological behaviour. Furthermore, the composition of surface layers also affect the adhesive force between the workpiece and tool. The variation of the composition of the surface layers can be achieved by changing the forming atmosphere. The junction strength, i.e. the tangential force required to break

adhesive metallic junction and the fundamental theories of junction formation were first developed by McFarlane and Tabor [14]. They also examined the role of combined stresses on the contact surface. McFarlane and Tabor [14, 15] studied the relation between friction and adhesion and established a relation between the adhesion of solid material and the effect of surface films. They found that the metallic junctions formed between the metal surfaces in contact are responsible both for friction and adhesion, furthermore, if the surfaces are covered with an oxide films with an appreciable thickness, the metallic interaction is reduced which result in a reduction in the adhesion. A magnesium-rich oxide surface film has been observed to form when Al-Mg alloys are heat-treated in a temperature range of 200-600^{o}C [16]. It was summarized that the growth of the magnesium oxide layer via the diffusion of Mg in MgO-spinel and the transport of Mg vapor across voids formed between the alloy substrate and the oxide layer [16]. Since the temperature of the Al–Mg sheet reaches above 400^{o}C during the hot-forming process, the effect of magnesium oxide on the adhesion of Al–Mg sheets to the die surfaces is a significant tribological issue to address. Thus, it is necessary to study the tribological behaviour of aluminum alloys during hot forming and to understand the mechanisms of adhesion in different atmospheres.

1.2 Thesis objective

The general overview presented in **Section 1.1** indicates that there are some important issues which affect the tribological behaviour during hot-forming. There has been limited tribological work done in the area of high temperature forming for aluminum sheet products to date. AA6061 (Al-Mg-Si) which is an alternative to hot formable alloy, it is a model material with tribolayer, lager grain size than AA5083 alloy, and exhibits GBS during hot forming. The current study examines the tribological behaviours of AA6061 at

elevated temperatures which includes the effect of deformation mechanism on friction behaviour, and the role of the atmosphere and deformation mechanisms play in developing the surface morphology during high temperature deformation. Thus, the present work was carried out with the following objectives:

(1) Study the tribological behaviour of aluminum alloy (AA6061) under dynamic conditions generated by the simultaneous effect of temperature and strain rate.
(2) Investigate the deformation mechanisms that influence the metal surface conditions and the coefficient of friction (COF).
(3) Investigate the role of the atmosphere (air and Argon) on the formation of surface oxides that control the friction and material transfer
(4) Examine the microstructural basis of the tribological behavior of AA6061 at elevated temperatures.

1.3 Organization of the thesis

This thesis is arranged into six different chapters, each of which is briefly described below.

Chapter 1 introduces the thesis, giving background information into the research and the research objectives. It focuses on aluminum-magnesium alloys, its uses in today's market as well as some processing methods.

Chapter 2 provides a literature survey relating to the thesis. It describes the hot-forming process, deformation mechanisms responsible for superplasticity observed in aluminum alloys, the oxide layer on the surface of Al-Mg alloy, tribology of aluminum and alloys, and the effect of atmosphere on tribological behaviour.

Chapter 3 presents the experimental procedures undertaken. This includes the experimental setup devised for this research, the conditions under which they were carried out, the parameters that were monitored, and the materials that were used. It is divided into two parts, the first handling the simulations for hot forming, and the second, the junction strength measurement. It describes the simulators designed for the purpose of the research as well as the analytical tools used to examine the specimen surfaces.

Chapter 4 presents the experimental results including the coefficient of friction (COF) of AA6061 alloy in air and argon gas and establishes a relation between COF and deformation mechanism map (DMM). And also describes the surface oxide characteristics, quantification of surface damage.

Chapter 5 discusses the results obtained, establishes a relation between COF and deformation mechanisms of AA6061 alloy, and the surface damage caused by the deformation at high temperature in different atmospheres are also discussed. Furthermore, an interpretation of the higher COF value obtained in argon which compare with that obtained in air is given as well as a discussion on adhesive metallic junction strength of the interface generated at the first contact between the working material and counterface.

Chapter 6 is a summary of the entire thesis, and presents a summary of the results obtained from the research and the discussions made.

CHAPTER 2 LITERATURE REVIEW

2.1 Background of forming process

2.1.1 The forming process

Hot-forming is accomplished by clamping a sheet material into a die and subsequently applying gas pressure to form the sheet into the die at a specified temperature. The temperature and the gas pressure used to form Al-Mg sheets are in range of 450^{o}C to 500^{o}C and 0.45MPa to 3.1MPa [12] respectively. A schematic illustrating the process inside the hot press is show in **Figure 2.1.** The sheet is heated to between 450^{o}C and 500^{o}C for hot-forming against the forming die. The sheet is held against the tool, and the gas pressure is applied to the back of the sheet using argon gas in order to force a heated aluminum blank to stretch into a certain shape by the die.

The hot-forming operation can be improved by controlling and improving the tribological conditions between the aluminum blanks and the forming die [12]. The tribological problems that occur during these processes include metallic particle transfer to the tool, which leads to adhesion and surface damage to both the die and the work piece [17]. The most commonly used lubricants in hot – forming processes are boron nitride (BN) and graphite [18]. Although graphite offers good lubricity at low cost, it decreases the efficiency of the subsequent sheet welding process, and it must be removed from the surface after forming. The use of coatings, including thermal spray coatings based on Cr compounds, electroless nickel-based coatings, and PVD and plasma assisted CVD coating based TiAlN have also been considered [19] to contribute toward reducing die – sticking. Although low friction at temperatures above 400^{o}C has been observed, these coatings usually fall short of eliminating the problem of metal transfer.

2.1.2 Superplastic forming (SPF) and quick plastic forming (QPF)

Superplasticity is the ability of a material to undergo very large uniform tensile/compressive deformation prior to failure, at a temperature well below its melting point [20]. Superplastic behaviour occurs at $T > 0.5T_M$. SPF is one of the hot-forming techniques where the exceptionally high ductility of the working material allows for great freedom of design. The aerospace industry uses SPF of parts because there has always been a need to use high strength-to-weight materials such as aluminum and titanium [21]. SPF alloys have a high strain rate sensitivity and occurs under high forming temperature in excess of 400^{o}C and it uses slow forming rates under which maximum strain sensitivity occurs to obtain a uniform final thickness distribution. Compared with SPF, QPF takes place at higher strain rates ($>10^{-3}s^{-1}$), and QPF of aluminium sheet has enabled the production of complex body closure panels that could not be manufactured by conventional stamping, and at higher production rates than would be possible with SPF [5].

2.1.3 Friction in hot forming

During hot forming, friction occurs due to the sliding of the workpiece against the die. It influences the material flow as well as the stress and strain distribution that occur in the workpiece. Friction behaviour is quite complex, comprising interacting variables that change constantly during the forming processes. These variables include deformation magnitude, forming speed, sheet and tool material, surface roughness, and tool geometry, the most significant of these being contact pressure and sliding velocity [22]. Friction increase is observed with increasing temperature and strain rate, factors on which the SPF ($500^{o}C/10^{-4}s^{-1}$) and QPF ($450^{o}C/10^{-3}s^{-1}$) operations are quite dependent. The evolution or development of the microstructure of the workpiece during forming is dependent on the strain rate applied, which in turn depends on the friction at the interface of the tool and the

workpiece. Friction also influences the state of stress at the interface between the tool and the workpiece [23]. Friction is related to adhesion which is another mechanism detrimental to hot forming. It has been stated in the literature to be controlled by adhesive forces and deformation forces [24].

The friction behaviour of Al-Mg alloy AA5083 at warm forming temperatures has been studied by Gali, et al.[25]. COF varies with temperature has been observed see **Figure 2.2**. At the constant strain rate of $0.04s^{-1}$, the mean COF values are observed to increase with temperature. The highest COF was observed at 450^{o}C (1.45 ± 0.18) while the lowest is seen at 250^{o}C (0.49 ± 0.32). They also studied the surface morphologies of AA5083 developed during the deformation see **Figure 2.3**, at high temperatures, the formation of the surface offsets was due to the deformation by GBS which lead to the high COF, while at low temperatures of 25^{o}C to 250^{o}C, no surface offsets were observed, and surface roughening was due to the surface oxide fracture as shown in **Figure 2.3**.

Das, et al. [26] studied the friction behaviour of AA5083 at hot forming temperatures (420^{o}C to 545^{o}C). It revealed the average COF value increased with the increasing in temperature and strain rate see **Figure 2.4**. The lowest COF value occurred at low strain rate and low temperature (0.95), however, the highest COF value was observed at high temperature and high strain rate (2.09).

2.1.4 Adhesion in hot forming

Earlier work by previous researchers has shown that there is marked interaction between metal surfaces when sliding occurs. Examination of the surface damage provides direct evidence for the formation and shearing of metallic junctions formed at the regions

of intimate contact. If the surfaces are freed of oxide or other contaminant films the friction reaches very high values.

McFarlane, and Tabor [27] stated that with soft metals, large adhesions may be observed during the intimate contact. They proposed an experiment set up on friction of steel sliding on indium in air at room temperature. The results show that there is a direct relation between the friction and the adhesion which may be expressed quantitatively in terms of the plastic properties of indium. When the two solids are placed in contact plastic flow occurs at the points of real contact until the area is sufficient to support the applied load. At these regions metallic junctions are formed as a result of a process of cold welding. These junctions are largely responsible for the adhesion and for the friction. If lubricants are applied to the surface the behaviour may be profoundly affected. For example, at load of 14.5g, the COF for clean surface is μ=5 whilst in the presence of paraffin oil it is of the order of μ=0.9 and the normal adhesion is negligible small. The main effect of the lubricant film is to hinder the growth of the metallic junctions so that the maximum value of the friction is much lower. McFarlane, and Tabor [27] found that the oxide film on the surface as a solid lubricant could lower the coefficient of friction in their proposed experiment.

McFarlane, and Tabor [27] did a further investigation on the effect of oxide film on the soft metal surface. Adhesion experiments were carried out on surfaces of indium, lead and tin which had been exposed to air in a desiccator for periods up to 30 days. With indium there was a steady decrease in adhesion with time of exposure. The results illustrated that no visible change occurred in the appearance of the indium surface even after 30 days. While with lead and tin where the oxide formed more rapidly and is considerably thicker the adhesion falls off more quickly. It is apparent that oxide films formed on the soft metal

may produce a marked reduction in adhesion. This is presumably because they reduced the amount of metallic contact between the surfaces. According to the statement from McFarlane, and Tabor [14], metallic adhesion depended primarily on the nature of the surfaces or the surface film. Gwathmey, et al.[28] have shown that copper surfaces will adhere strongly if the oxide films have been removed by reduction in a stream of hydrogen at elevated temperatures. This is because the absence of the oxide film tends to increase the amount of metallic contact between the surfaces. Similarly, Holm and Kirschstein [29] found that metals outgassed in vacuum gave high frictions and often adhered together.

At elevated temperatures, adhesion, the material transfer of the softer workpiece material to the tool, which causes critical issues during hot forming operations. If the transferred material is welded to the tool/die surface, it leads to the accumulation of material on the tool surface, resulting in a decrease in surface quality of the finished products [30]. This surface damage that occurs during sliding contact due to material adhesion is often referred to as galling, scuffing, and scoring [24].

Adhesion and material transfer tend to be dependent on such factors as temperature, tool roughness and surface composition, contact pressure, and sliding velocity [24]. High friction is often associated with adhesion, it has been recorded as increasing the rate of material transfer, and an increase in friction is used as an indicator of galling [3]. Aluminium adhesion on the die surface is a crucial problem for any elevated temperature forming process. Gali, et al.[25] studied the effect of the temperature on material transfer to pin surfaces. AA5083 alloy covered with oxide layer was used in their tests, and the amount of material transfer increased with increasing temperature, see **Figure 2.5**. At temperature lower than 200^{o}C, no significant transfer could be observed. However, when

the operating temperature increased above 300°C, considerable amounts of transfer occurred, and the transferred material at high temperature covered a large area on the contact surface of the pin. Gali, et al. [31] also studied the effect of surface conditions on the elevated temperature sliding contact deformation of AA5083 alloy, and polished and tribolayer covered sample were considered in their tests. The transferred material was distributed discontinuously over an area of the pin when it slid against the tribolayer covered sample see **Figure 2.6**; material transfer was adhered however in a localised area, comprising of a circular head and a tail having a semi elliptical appearance when it slid against the polished sample see **Figure 2.7**.

Friction and adhesion behaviours during the hot forming processes were reviewed in **Section 2.1.3** and **Section 2.1.4**, and these behaviours are attributed to the surface damage during the hot forming process. However, simultaneously, the bulk material below the surface is subjected to plastic deformation. The next Section will present a review on deformation mechanisms during superplastic forming.

2.2 Deformation mechanisms for superplastic forming

2.2.1 General creep equation

The Arrhenius equation is most widely used to describe the relationship between the strain-rate, flow stress and temperature, especially at high temperatures. Deformation behaviour of the material during SPF/QPF can be described by the power law function [32]:

$$\dot{\varepsilon} = A\left(\frac{\sigma}{E}\right)^{n} \exp\left(-\frac{Q}{RT}\right) \quad (1)$$

Where A is material constant, σ is the flow stress, n is the stress exponent, E is the temperature compensated Young's modulus, Q is activation energy for deformation, and R is the universal gas constant.

The stress exponent, n, can be obtained from the slope of a $\ln\dot{\varepsilon}$ vs. $\ln\sigma$ plot. In many cases deformation behaviour of the material is also described by the inverse of stress exponent, 1/n (strain rate sensitivity, m). For example, $n = 2$ implies deformation by GBS [4].

Das, et al. [26] studied the plastic deformation behaviour of Al-Mg alloy (AA5083) at elevated temperatures and established a deformation mechanism map see **Figure 2.8**. Diffusional flow, GBS, and solute drag mechanisms were identified based on the stress exponent value within the temperature and strain rate ranges studied. It revealed how the temperature and strain rate affect the deformation mechanism during SPF/QPF process.

2.2.2 Diffusional flow

Diffusional creep may occur at low strain rate ($<1.5\text{x}10^{-2}\text{s}^{-1}$) for Al-Mg alloy through the grain boundaries [26]. Two mechanisms are accompanied by the diffusion flow: Coble creep (favoured at lower temperatures) through the grain themselves, and Nabarro-Herring creep (favoured at higher temperatures). For Nabarro-Herring creep, diffusion of vacancies through the grains from one grain boundary to another. Excess vacancies are created at grain boundaries perpendicular to the tensile axis with a uniaxial tensile stress. The constitutive equation under the diffusion of vacancies through the grain boundaries can be described as:

$$\dot{\varepsilon} = \mathrm{k}_1\left(\frac{Dgb}{d^3}\right)\left(\frac{Eb^3}{kT}\right)\left(\frac{\sigma}{E}\right) \quad \text{(grain boundary diffusion[33])} \qquad (2)$$

Where D_{gb} is the grain boundary diffusion coefficient, b is the Burgers vector, d is the grain size, E is the Young's modulus, k is Boltzmann's constant, and k_1 is a material constant.

These excess vacancies diffuse from the grain boundaries lying normal to the tensile direction towards those parallel to it, as illustrated in **Figure.2.9**. Grain boundaries act as perfect sources and sinks for vacancies. The constitutive equation for diffusional flow with a predominant diffusion through the grain interior:

$$\dot{\varepsilon} = \mathrm{k}_2\left(\frac{DL}{d^2}\right)\left(\frac{Eb^3}{kT}\right)\left(\frac{\sigma}{E}\right) \quad \text{(lattice diffusion [33])} \quad (3)$$

Where *DL* is lattice diffusion coefficient, *k* is Boltzmann's constant, and k_2 is material constant.

2.2.3 Grain boundary sliding (GBS)

GBS involves the relative translation of two grains by a shear movement parallel to their common boundary. In many well documented studies of superplasticity in fine-grained materials, it has been observed that even after large elongations, there is no appreciable change in grain shape, and the grains remain equiaxed [34]. With the application of tensile stress, diffusion occurs along the grain boundaries as grain boundary interfaces slide past each other. Thus, there is a strong dependence on the grain size. Also, the entire grain rotates during this process. This typically results in the grains remaining equiaxed and random in texture [34].

2.2.3.1 GBS mechanisms

There are two types of GBS mechanisms reported in the literature: Rachinger sliding [33] and Lifshitz sliding [35]. Rachinger sliding is a mechanism where grains retain their original shape even after large elongations, as shown schematically in **Figure 2.10a**. Rachinger sliding occurs by the movement of extrinsic dislocations along grain boundaries, and the climbing of accumulated dislocation within a grain controls the rate of sliding [33]. In Rachinger sliding, the shape change of the specimen occurred by neighbour-switching event without any permanent change in shape of the grains themselves. On the other hand,

Lifshitz sliding is considered to be due to stress-directed flow of vacancies either through the grain interiors (Nabarro-Herring creep) [36] or along the grain boundaries (Coble creep) [37]. A schematic illustration of Lifshitz sliding is shown in **Figure 2.10b**. In **Figure 2.10b**, grains become elongated in the tensile direction due to the directional flow of vacancies from grain boundaries experiencing tensile stresses to those which have compressive stresses.

During superplastic deformation, large strains are achieved with grains retaining their equiaxed shape, which is similar to Rachinger sliding. Therefore, it is considered that Rachinger sliding is involved in superplastic deformation [33].

Some microscopical models were proposed to explain the superplastic deformation behaviour. These models can be classified into two groups: GBS accommodated by diffusional flow and GBS accommodated by slip.

2.2.3.2 GBS accommodated by diffusional flow

Ashby and Verrall [36] proposed a 2-D model based on GBS with diffusional accommodation, and this can be explained by a grain-switching event for a four-grain unit without obvious deformation of grains (**Figure 2.11**). The schematic illustrates the grain switching mechanism, during the intermediate stages grains change their original shape by diffusional flow occurring by mass transfer through grain boundaries. The inter-grain distance perpendicular to the tensile direction contracts and the grain boundaries come closer and engage the grains in the lateral direction, while along the tensile direction the grains move apart.

Based on the analysis on many superplastic materials, Luthy et al. [37] confirmed that most of the GBS models developed so far have been found to correlate well with

experimental data, and led to a constitutive equation for GBS accommodated either by lattice diffusion or grain boundary diffusion as in Equations (4) and (5) respectively.

$$\dot{\varepsilon} = k_3 \left(\frac{Dgb}{d^3}\right) \left(\frac{\sigma}{E}\right)^2 \quad \text{(boundary diffusion controlled [38])} \qquad (4)$$

$$\dot{\varepsilon} = k_4 \left(\frac{DL}{d^2}\right) \left(\frac{\sigma}{E}\right)^2 \quad \text{(lattice diffusion controlled [38])} \qquad (5)$$

Where D_{gb} is grain boundary diffusion coefficient, DL is lattice diffusion coefficient, b is the Burgers vector, d is the grain size, σ is the flow stress, E is Young's modulus, k is Boltzmann's constant, and k_3, k_4 are material constants. In Equations (4) and (5), the stress dependence of the power law is given by n = 2 (also implies strain rate sensitivity m = 0.5), which corresponds to the GBS mechanism.

2.2.3.3 GBS accommodated by Slip

GBS can occur also by dislocation slip, which occurs due to dislocation pileups within the grain and also due to pileups in the grain boundary. The model of dislocation pileups in the grain interior was first proposed by Ball and Hutchinson [39] see **Figure 2.12.** based on the sliding of a group of grains. In this mode, grains whose boundaries are suitably aligned will slide as groups during deformation. The shear stress on the group becomes concentrated on any grain or protrusion that obstructs the motion of the group. Local stresses would generate dislocations in the blocking grain and dislocations would pileup at the opposite grain boundary until their back stress prevents further generation of dislocations and thus further sliding by the group.

By assuming climb is slower than glide, this model suggests climb of dislocation as the rate controlling process. Based on this, the model predicts a stress exponent of n=2 (m=0.5) arising from the stress concentration due to the dislocation pileups.

2.2.4 Viscous glide controlled creep

Creep of solid solution alloys at intermediate stresses and under certain combinations of materials parameters can often be described by three regions [33].This is illustrated in **Figure. 2.13.** With increasing stress, the stress exponent, n, changes in value from 5 to 3 and again to 5 in regions I, II, and III, respectively. The mechanism of deformation in region II is viscous-glide of dislocations and it has been observed in Al-2.2 at% Mg alloy [33]. This is due to the fact that the dislocations interact in several possible ways with the solute atoms, and their movement is impeded. Distribution of the solute atoms (interstitial or substitutional) around a moving dislocation would cause a perturbation force that acts on the dislocation opposite to the applied stress. Due to this opposing force the motion of dislocations slows down. This force can be regarded as viscous drag, which allows a steady state motion under a steady state stress, and the mechanism known as viscous glide creep mechanism. There are two competing mechanisms over this stress range, dislocation climb and viscous glide, and viscous glide is slower and thus rate controlling. The constitutive equation that describes viscous glide creep mechanism is given in the form of Equation (6).

$$\dot{\varepsilon} = \mathrm{k}_5 \left(\frac{Ds}{d^2}\right) \left(\frac{\sigma}{E}\right)^3 \tag{6}$$

Where D_s is solute atom diffusion coefficient, b is the Burgers vector, d is the grain size, ϭ is the flow stress, E is Young's modulus, k is Boltzmann's constant, and k_5 is a material constant.

There are several possible processes in region II, where n = 3 [33]. Fisher [40] suggested that in solid solution alloys with short-range order, dislocation motion destroys

the order. The generation of dislocation pileups of high density gives the possibility of pushing leading dislocations through the regions of short-range ordering. Therefore, in the course of their cooperated movement, the pileups of dislocations destroy the short-range ordering. Cottrell and Jaswon [41] proposed that the dragging process is the segregation of solute atmospheres to moving dislocations. The dislocation speed is limited by the rate of migration of the solute atoms.

2.2.5 High temperature deformation mechanisms in Al an Al-Mg alloys

Higher temperature deformation mechanisms of an aluminum alloy depend on the solute content and grain size of the alloy. To represent various deformation mechanisms that operate in pure aluminum, a deformation mechanism map (DMM) see **Figure 2.14** was constructed on stress vs. temperature axes by Frost and Ashby [42]. The zones of different mechanisms were identified, based on the stress exponent (n) value. Figure 2.14 presents the DMM generated by frost and Ashby for pure aluminum of grain size of 10μm. The range of strain rate and temperature over which the hot forming operation takes place is narrow. Another DMM was constructed by Kim et al. [43] for aluminum alloy at a temperature of 800K (527^{o}C) is shown on grain size vs. stress axes in **Figure 2.15**. Different deformation mechanisms under the circumstances where the initial grain size varies largely were identified by this map. The earlier version of the DMM constructed by Frost and Ashby [42] did not show the region of GBS. However, the DMM constructed by Kim et al. [43]shows the region of GBS as lying between the regions of diffusional flow and power-law creep.

There are two main creep mechanisms responsible for the diffusional flow. One is known as Nabarro-Herring creep, which occurs at temperatures near the melting point (T

> 0.8Tm) and very low stresses ($\sigma/E < 5 \times 10^{-7}$) as a result of vacancy diffusion and causes strain accumulation by strain elongation. This mechanism is characterized by lattice diffusion that occurs at the grain interiors [35, 44](**see Figure 2.9**). Another one is Coble creep, which is normally observed at T < 0.8Tm[42], and the grain boundaries are the preferential diffusion paths (grain boundary diffusion). In both cases, the steady-state strain (creep) rate increases linearly with the applied stress, producing a stress exponent, $n = 1$.

GBS is generally characterized by an activation energy that is equal to the activation energy for either grain boundary diffusion or lattice self-diffusion and a stress exponent of $n = 2$. GBS is favoured in alloys with equiaxed grains < 10 μm and the presence of second phase particles that inhibit grain growth.

Requena, et al. [45] studied the creep behaviour of AA6061 alloy at 573K. They found that a stress exponent of $n \approx 1$ for stresses from 15 to 25 MPa indicates the dominating diffusional creep mechanism. A stress exponent of $n \approx 3$ is found from 25 to 50 MPa concluding dominating dislocation creep as shown in **Figure 2.16**. Khamei, et al. [46] performed the hot tensile tests to study the strain rate sensitivity m (m = 1/n) of AA6061 at the temperature range of 300ºC to 500ºC. The value of strain rate sensitivity (m) was observed equal with 0.3 (n = 3) when the dominant mechanism is dislocation creep.

2.3 The disturbed layer

The surface of aluminum alloy sheets contains a tribolayer know as disturbed layer that forms during prior thermo-mechanical treatment particularly during hot rolling of the sheet. The disturbed layer was first observed by Leth-Oslsen et al [47] while researching filiform corrosion (FFC), a thread-like form of corrosion that occurs under painted and

plated surface of especially aluminum alloys. They believed that the sensitivity of aluminum alloys to corrosion is related to the disturbed layer. Its formation has been attributed to the much higher strains experienced by the surface of the alloy as compared with that of the bulk, resulting in the difference in microstructural characteristics between them [48]. The high strains observed are due to the high shear deformation that the surface bears such as sliding [49]. These layers are characterized by rolled-in oxide patches and a distribution of ultra-fine aluminum grains mixed with the comminuted fragments of fractured second phase particles [50, 51]. The schematic representation in **Figure.2.17** shows the subsurface layer containing the microcrystalline oxide mixed with small-grained metal [50].

2.3.1 The formation of the disturbed layer

The formation of these layers is dependent on the tribological conditions at tool and metal surface during rolling. The disturbed layer is formed due to the high shear experienced by contact of the tool and the metal piece under lubricated conditions [50].

During metal working, the surface and subsurface region of metal are subjected to different conditions from the bulk of the metal. Metal transfer is induced by the interactions between the workpiece and the tool, variety of mechanisms can take place, and the oxidation is accompanied by this stage. The oxidized transferred material can be retransferred back to the work piece surface and a distinct surface appearance can be observed [50]. Frolish et al. [52], from their simulation of industrial rolling proposed that the mechanism causing the disturbed layer and the mixing in of the oxide particles was from slip occurring at the interface of the roll and workpiece and the action of the roll surface asperities on the workpiece surface.

The surface/near-surface region of aluminum sheet is subjected to enhanced shear strains during rolling, resulting in the formation of near-surface deformed layers with different microstructures to the underlying bulk alloy [53]. Scamans [54] later suggested the severe surface shear experienced during hot rolling as the reason the surface of the alloy was ploughed and re-welded back together. This, he noted, caused the integration of the oxide and explained the sharp transition observed from the disturbed surface to the bulk-grained microstructure beneath it.

2.3.2 The ultra-fine grain of the sub-surface

Frolish et al.[47] noted that the diffusion of magnesium to the surface of the alloy, which was observed to occur rapidly and increase in intensity with time, was in part responsible for the formation of the subsurface layers as its oxides were observed to provide the Zener pinning of the grain boundaries thus producing the fine grain features. They suggested that the depth of the magnesium content correlated with the thickness of the subsurface layer, although noting that the subsurface layer structure depended on the alloy composition and the processing conditions [47].

Xia, [55] in his experiments observed precipitates also involved in the Zener pinning of grains which prevented subgrain growth during the hot rolling of aluminum alloys. Premendra et al. [56], also observed broken intermetallics on the surface of the metal at grain boundaries, which he suggested were involved in pinning grains.

2.3.3 Surface oxidation behaviour of Al-Mg alloy

When Al-Mg alloys are heat-treated during their production and fabrication, magnesium is lost from the bulk of the material. If heated in vacuum, the surface active magnesium is lost through evaporation. If heated in air at high temperatures, magnesium is

depleted from the bulk with the formation of nonuniform and relatively thick, dark oxide layers on the surface [16, 57]. Zayan, et al.[16] studied the oxidation behaviour of two of Al-Mg alloys which contained 0.4 and 2.0 wt. % Mg. They found that the oxidation of the alloy showed a strong tendency for Mg to diffuse outward from the base alloys. The magnesium appeared in the form of MgO and spinel ($MgAl_2O_4$) and the major constituent of the oxide was MgO. The mechanism for the growth of the oxide layer in 0.4% Mg alloy was the solid-state diffusion of Mg in the MgO-spinel constituents; for alloys of higher Mg content, the growth of the oxide layer would therefore be controlled by the transport of Mg vapor across voids formed between the alloy metal and oxide layer [16].

Lea and Ball [57] provided a schematic model (see **Figure 2.18**) of the growth of the oxide film on Al-Mg alloys during the heat treatment. The alloy is protected by a very thin self-healing amorphous film of Al_2O_3. When it is heat treated in air at temperatures beyond 350^oC the oxide becomes crystalline γ-Al_2O_3 and its thickness continues to increase by the diffusion of Al and Mg to the free surface. This action also promotes the formation of MgO islands on the surface and spinel $MgAl_2O_4$ at the interface. The morphology and composition of the complex oxide film can be controlled not only by time and temperature but by the humidity of the environment [57]. If alloy containing higher bulk magnesium, more magnesium diffusion and oxide formation at the surface [58]. Riahi et al. [59] showed that when the magnesium content increases from 0.7 % to 4.7 %, the thickness of oxide layer increases from 35 nm to 100 nm.

The oxide scale that forms on the metallic surface acts as a hard, protective layer in some high temperature applications. In many applications the oxides are stressed either by an externally applied load, or by oxide growth stresses. The thermal stress induced by a

mismatch of thermal expansion coefficients of the oxide layer and substrate is another mechanism of oxide failure. When the substrate is subjected to creep deformation, the surface oxide crack density initially increases with strain [60] and eventually reaches a saturation point. This behaviour has been illustrated in a model for viscous sliding of oxide segments against a substrate subject to creep [60].

2.3.4 Oxide ligament (fibre) formation within the oxide layer

The oxide ligaments within the oxide layer were able to accommodate the imposed strains and exhibited superplastic behaviour because of the nanocrystalline oxide grains of 3 – 7 nm in diameter observed in their cross-sections. The size and geometry of these grains promote superplastic behaviour by grain boundary diffusion. More information regarding the formation of the ligaments can be obtained from **Figure 2.21** [61] and **Figure 2.22** [26].

Das, S., et al. [62]. Studied the deformation and fracture of tribolayer on the surface of AA5083 sheet aluminum-magnesium alloy, they found that the oxide fibres always formed at locations of tribolayers extending above the grain boundaries of Al–Mg grains that experienced sliding during plastic deformation, and the fibres showed uniform extension to 10 times of their diameter which means superplastic behaviour of the oxide fibre.

The superplasticity of the oxide fibres could be attributed to the nanocrystalline nature of oxide grains. And the superplasticity has been observed in a number of nanocrystalline materials with grain sizes in the range of 10–100 nm tested at low temperatures ($<0.4\ T_m$) [63]. Two models have been suggested to represent deformation behaviour of nanocrystalline materials that exhibit limited ductility. One was suggested by Gleiter [64] that grain boundary diffusion (Coble creep) should be the principal

deformation mechanism in nanocrystalline materials, another one is the dislocation accommodated grain boundary sliding [65]. A schematic diagram illustrating the possible microscopic processes responsible for the large elongations of the oxide fibres is given in **Figure. 2.23** [62], where the section of the tribolayer being stretched as a result of formation of a surface step by sliding of adjacent Al-Mg grains. The oxide can accommodate the imposed strains due to the enhanced diffusional flow due to its nanocrystaline microstructure.

2.3.5 Junction strength

The maximum force required to break the asperity junction formed at the first contact is termed as 'junction strength'. The fundamental theories of a junction formation were first developed by McFarlane and Tabor [14]. They also examined the role of combined stresses on the contact surface. McFarlane and Tabor [14, 27] studied the effect of surface oxides on the strength of adhesive junctions that form between the surfaces in contact, and related a metallic material's adhesion tendency to the thickness of the surface oxide layer. It was proposed that the severity of an intimate metallic contact between the surfaces reduced as the surface oxide thickness increased, which reduced the junction strength due to adhesion. A magnesium-rich oxide surface film has been observed to form when Al-Mg alloys are heat-treated in a temperature range of 200-600^{o}C [66]. It was proposed that the diffusion of magnesium to the surface can occur through the existing surface oxide layer via two mechanisms: (i) outward magnesium ion diffusion and (ii) magnesium vapour transfer from oxide defects and voids [66]. Since the temperature of the Al–Mg sheet reaches 420^{o}C during the hot-forming process, the effect of magnesium oxide on the adhesion of Al–Mg sheets to the die surfaces is an important technological issue to address. A.R. Riahi and A. Edrisy [59] studied the effect of an aluminum alloy's

magnesium content on its adhesion tendency at high temperature. A pin-on-disc tribometer operated at a typical hot-forming temperature to systematically study the effect of the magnesium content of commercial 5000 series aluminum alloys on their adhesion to simulated steel die surfaces. The authors have determined the junction strength between the Al–Mg alloys and the steel counterface by measuring the tangential force required to break the adhesive junctions formed during initial sliding contact. The junction strength in Al-Mg alloy was found to be dependent on magnesium content of the material, as in **Figure 2.19**. Low adhesion tendency was found in the material with high magnesium content.

Das [61] studied the junction strength behaviour between AZ31 and AA5083. The result illustrated that junction strength of AZ31 is lower than the strength of AA5083 alloy due to the higher Mg content in AZ31. The existence of magnesium rich surface oxide reduced junction strength, and hence low COF is expected in AZ31 alloy [61]. Regardless of testing conditions, AZ31 magnesium alloy always showed lower COF compared to aluminum AA5083 alloy under the same homologous temperature and strain rate conditions as shown in **Figure 2.20**. In AZ31 alloy, once the surface became completely oxidized (MgO), material transfer to counterface disk was reduced. However, in AA5083 alloy, the formation of MgO was not sufficient to reduce the material transfer and COF. The junction strength experiments provided a better understanding of the COF behaviour of alloys with different magnesium content.

2.3.6 Effect of oxide ligament (fibre) formation on friction

Formation of the fibre has been discussed in **section 2.3.4**, in this section the effect of oxide fibre on friction will be discussed. Gali, et al. [31] studied the role of oxide fibres on the tribological behaviour. They found that the oxide fibres exhibit superplastic

behaviour was due to nano-crystalline grain plasticity and viscous flow of the amorphous regions, and the flattened appearance of fibres observed in the wear track **Figure.2.24 (a)** and **(b)** may have taken part in controlling the friction of AA5083 alloy. As the fibres are subjected to visco-deformation it may provide low shear during sliding. The viscous behaviour of the fibre could therefore be a factor in lowering the friction. An oxidizing environment that promotes the formation of the nano-crystalline oxides on the alloy surface could further reduce the friction. Thus further studies are needed to establish the role oxide fibres on tribological properties of Al–Mg Alloys under different atmospheres.

2.3.7 Effect of atmosphere on the tribological behaviour

The composition and the mechanical behaviour of the surface layer on the forming material and the contacting tool determine the tribological behaviour. Furthermore, the composition of surface layers also affect the adhesive force between the workpiece and tool. The variation of the composition of the surface layers can be achieved by change the forming atmosphere.

Banares and Wachs [67] found that different environments (ambient and dehydrated) could affect the molecular structures of supported metal oxide catalysts. Hung-Kuk [68] studied the influence of atmosphere humidity on the friction and wear of carbon steels and it was found that at low humidity severe wear occurs and at a high humidity mild wear can be expected. Kim [69] studied the effects of oxygen and humidity on friction and wear of diamond-like carbon films using ball-on-disk experiments. It was observed that in dry argon, the contact area of the ball was covered with material transferred from the DLC film during sliding, however, in dry and humid air, surface layers of DLC were oxidized by a tribochemical reaction and the oxides covered the contact areas on both the DLC film and

the ball. Therefore, there is a need to conduct experiments involving in-situ observations on adhesion and oxide formation of Al and Mg alloys in different atmospheres and at hot-forming temperatures.

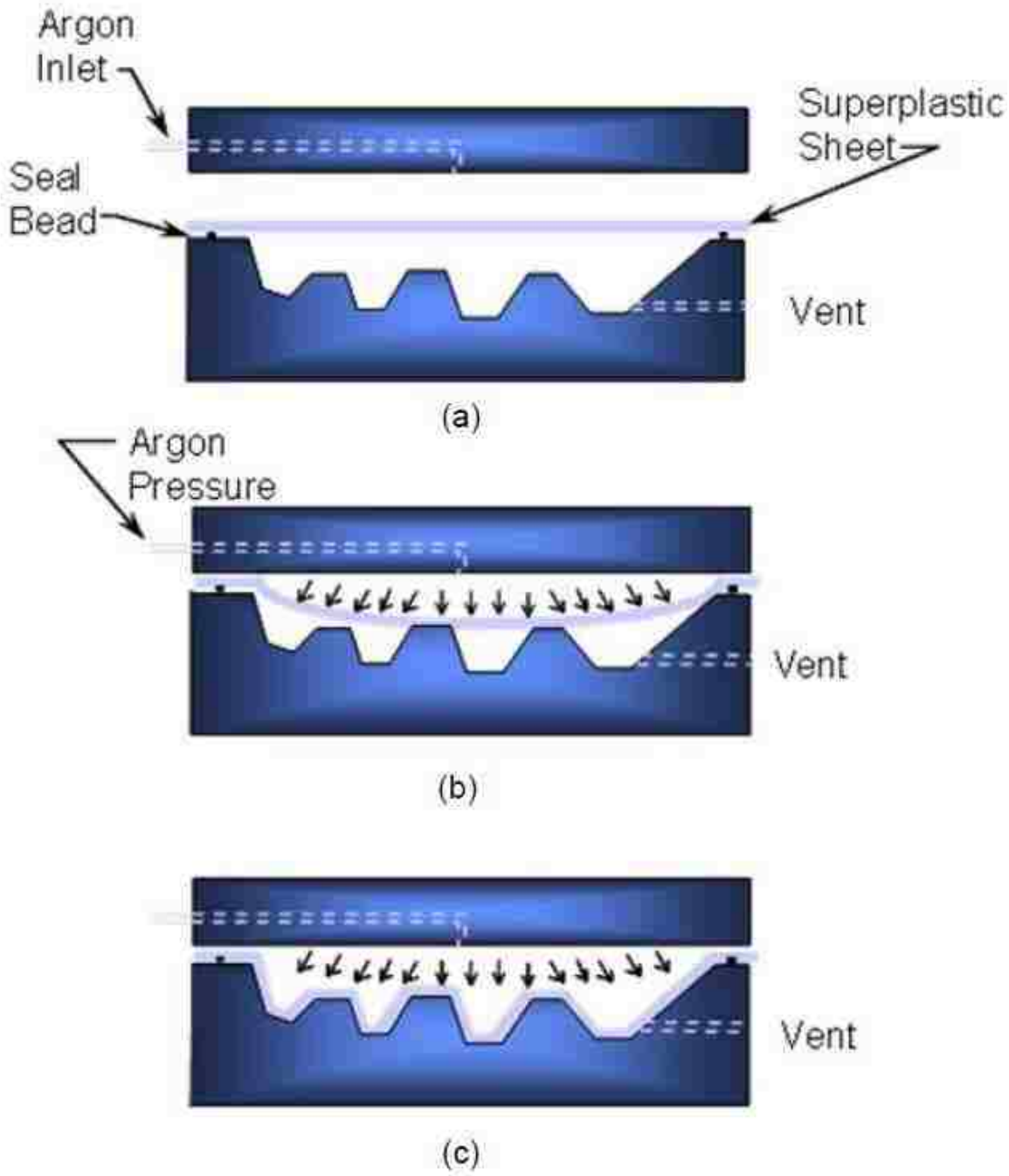

Figure 2.1 Schematic representation of the hot-forming process – (a) sheet of metal is sealed around its periphery between an upper and lower die. The dies and sheet are maintained at the SPF temperature. (b) the sheet is heated to its superplastic temperature range, gas pressure is injected through inlets in the upper die (c) the lower cavity is maintained under vacuum or can be vented to the atmosphere and at the same time gas pressure is used to form the sheet down over the tool.

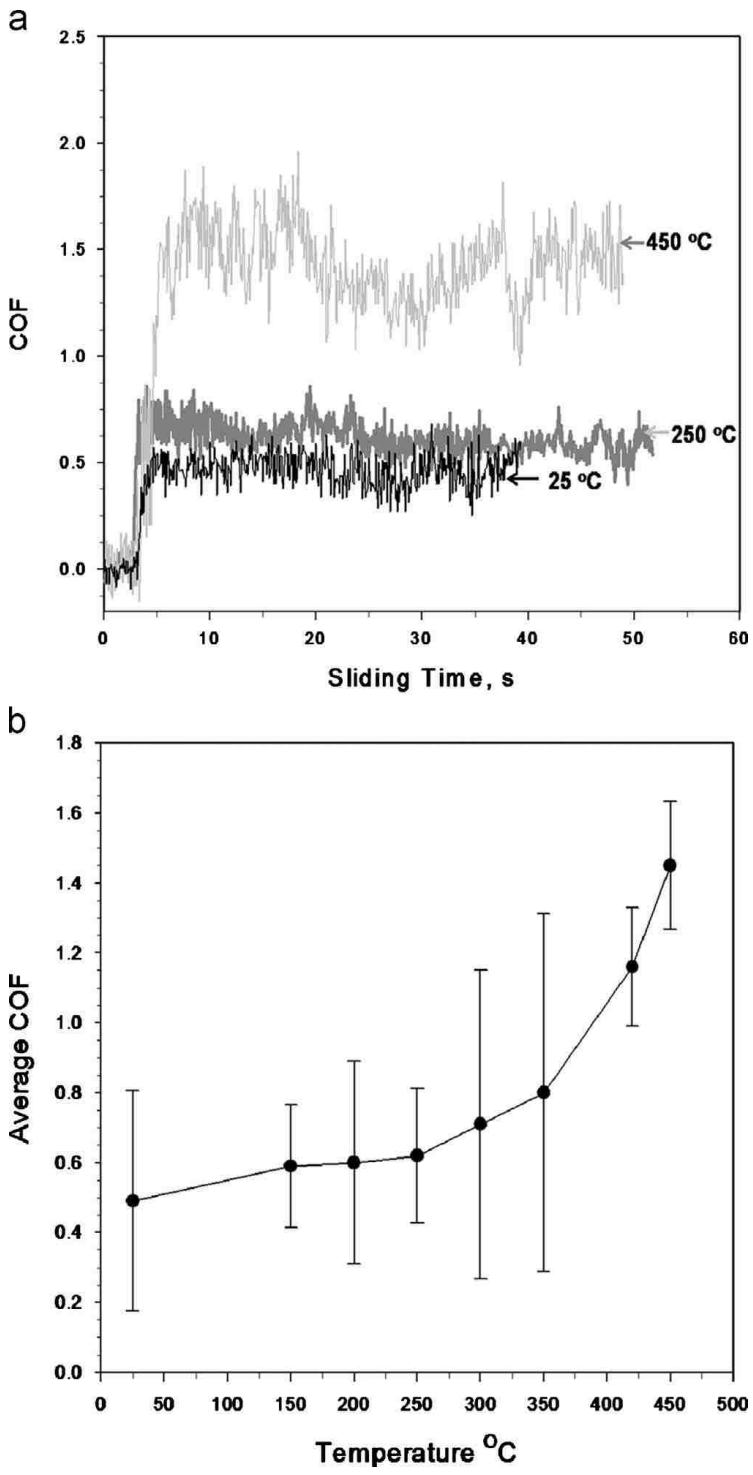

Figure 2.2 (a) COF vs. sliding time plots at25°C, 250°C and450°C that show the measured COF during experiments at 0.04 s^{-1}(b). Average COF vs. temperature plot forAA5083alloy [25].

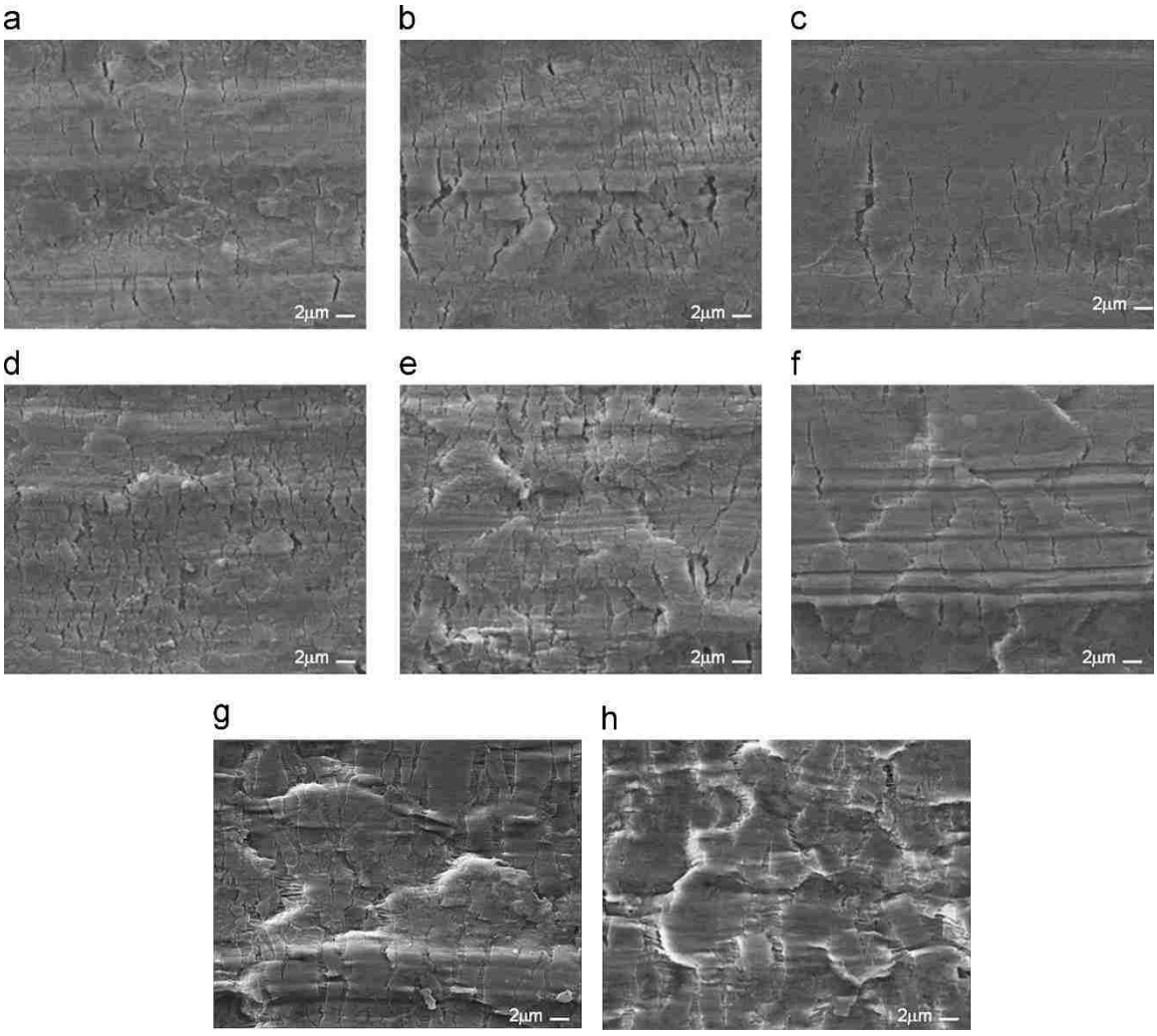

Figure 2.3 Secondary electron images of AA5083 aluminium alloy strip surface after deformation under a strain rate of 4×10^{-2} s^{-1} at (a) 25 °C, (b) 150 °C, (c) 200 °C, (d) 250 °C, (e) 300 °C, (f) 350 °C, (g) 400 °C, and (h) 450 °C [25].

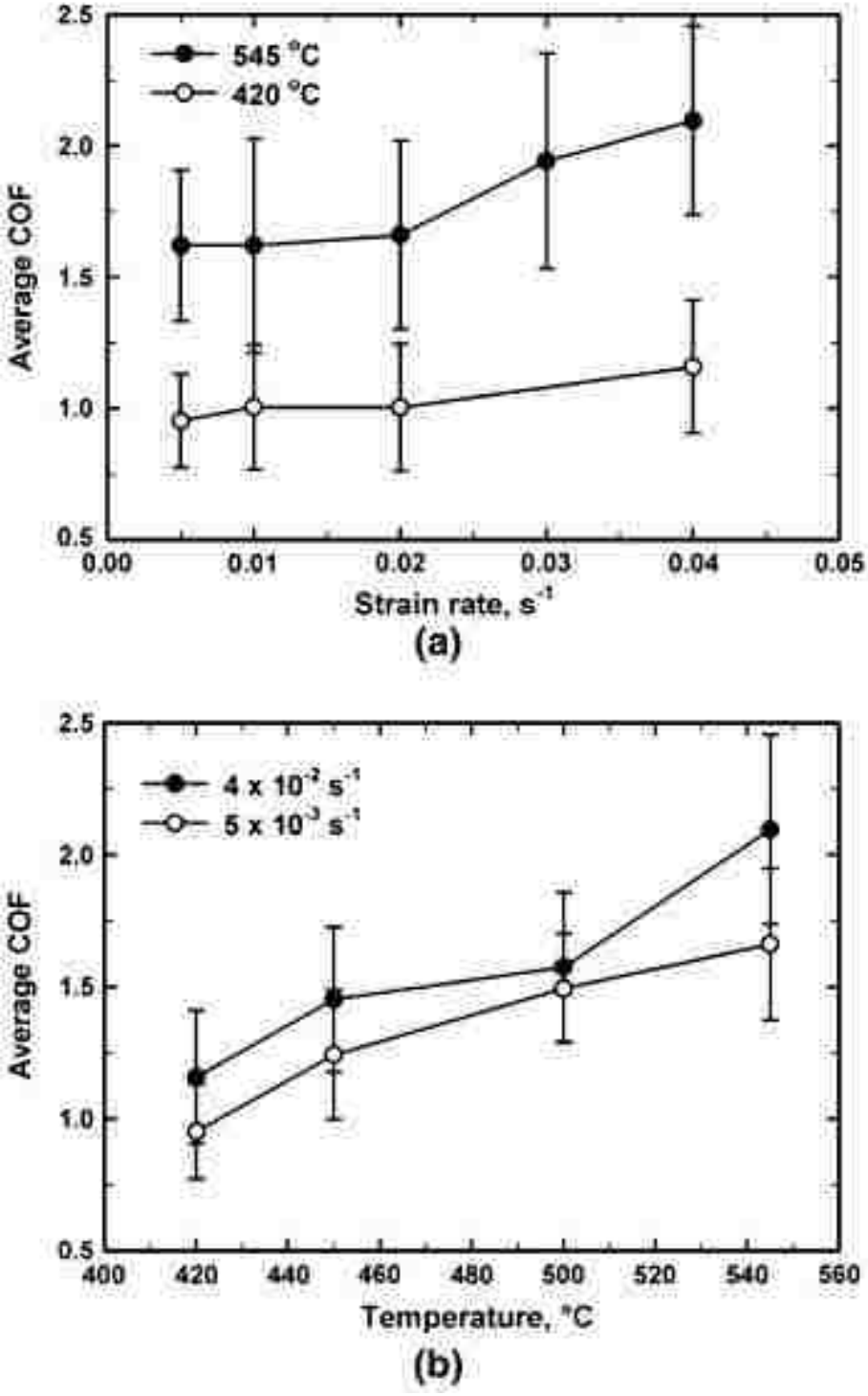

Figure 2.4 (a) Average COF vs strain rate plot. (b) Average COF vs temperature plot [26].

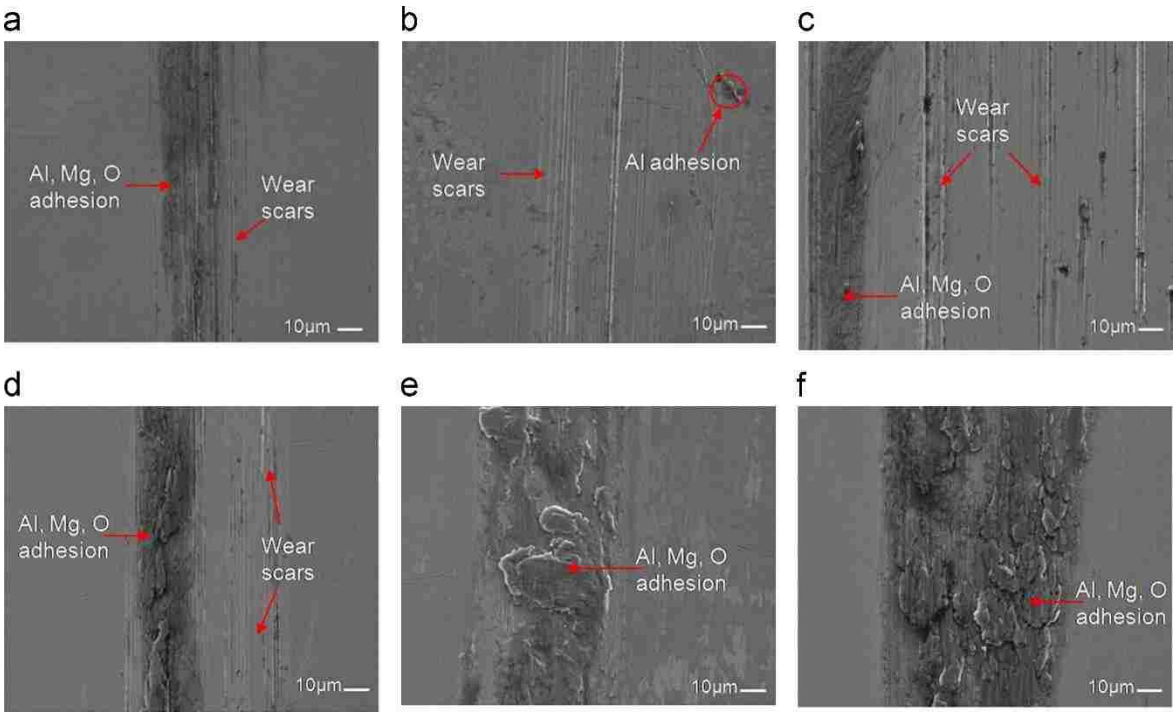

Figure 2.5 Secondary electron images of material transferred to P20 steel pin from AA5083 aluminium at (a) 25 °C, (b) 150 °C, (c) 200 °C, (d) 250 °C, (e) 300 °C, and (f) 350 °C [25].

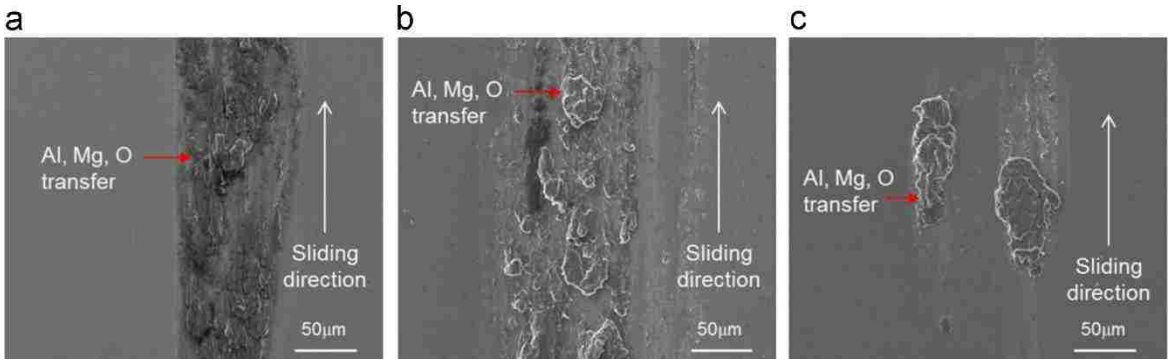

Figure 2.6 Secondary electron images of material transferred to P20 steel pin from the as-received (with tribolayer) AA5083 aluminium alloy at (a) 350 °C, (b) 450 °C and (c) 545 °C [31].

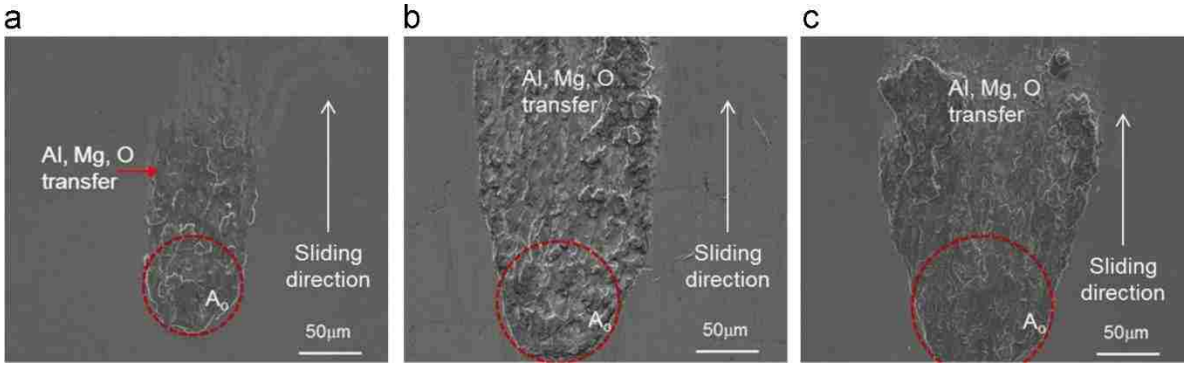

Figure 2.7 Secondary electron images of material transferred to P20 steel pin from the polished AA5083 aluminium alloy at (a) 350 °C, (b) 450 °C and (c) 545 °C illustrating the initial contact area (A_0) [31].

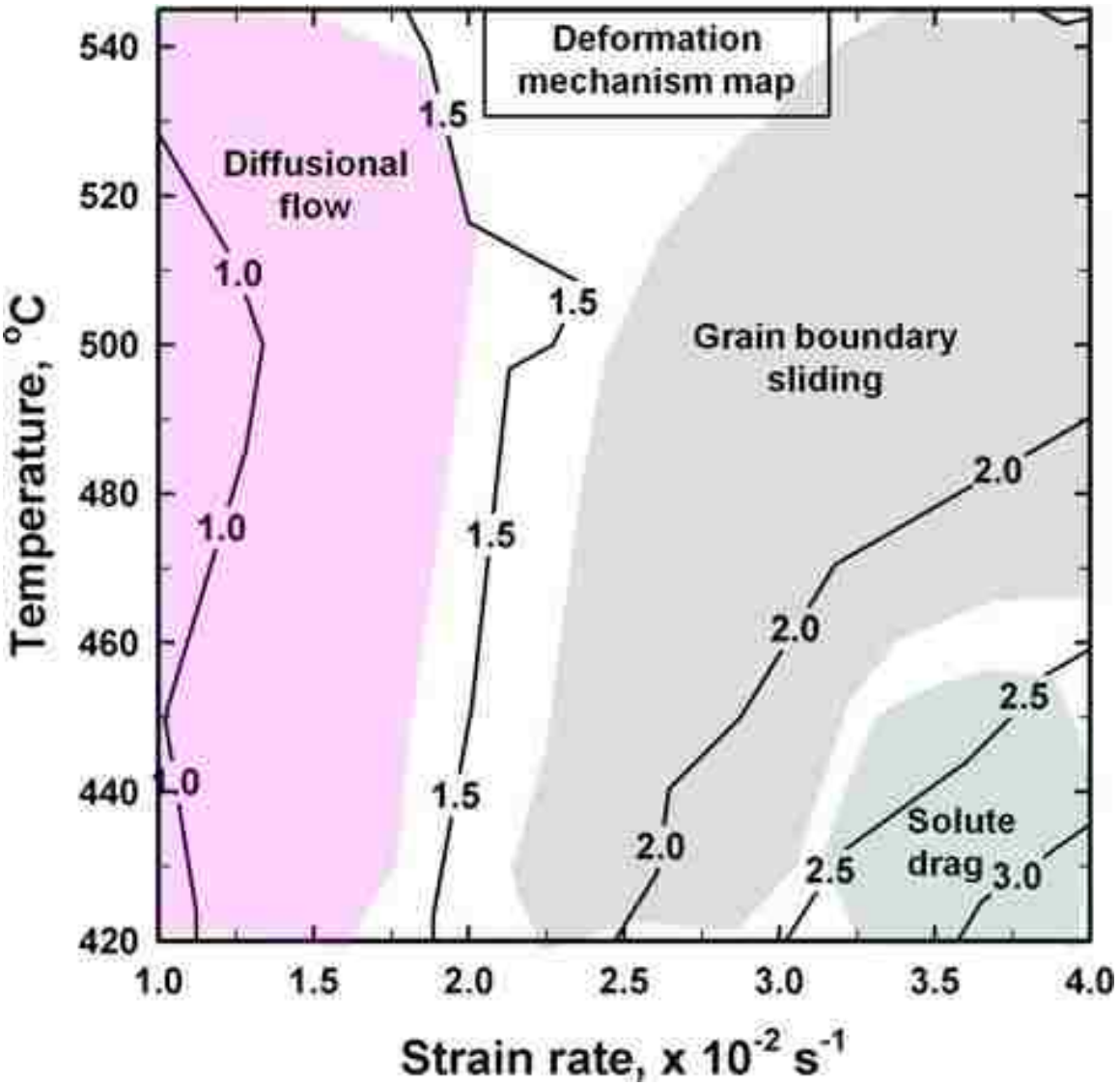

Figure 2.8 Deformation mechanism map for AA5083 plotted on temperature vs strain rate axes, where the regions of dominance for each mechanism are identified based on the stress exponent value n. The contours are for constant stress exponent values [26].

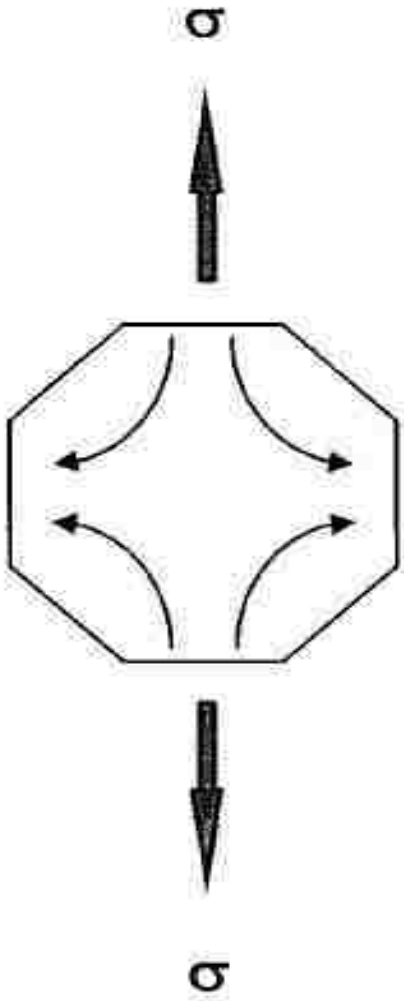

Figure 2.9 Nabarro-Herring model of diffusional flow. Arrows indicate the flow of vacancies through the grains from boundaries lying normal to the tensile direction to parallel boundaries. Thicker arrows indicate the tensile axis [35].

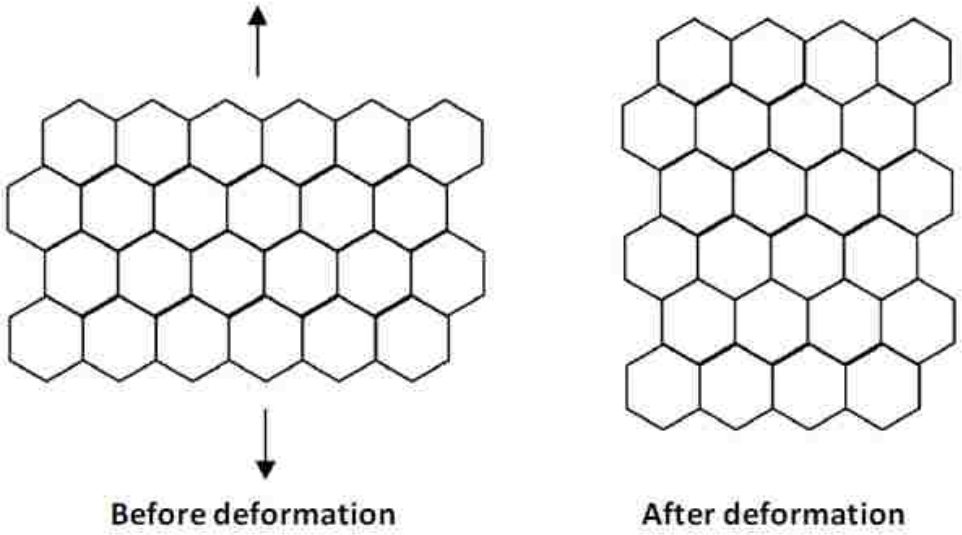

(a)

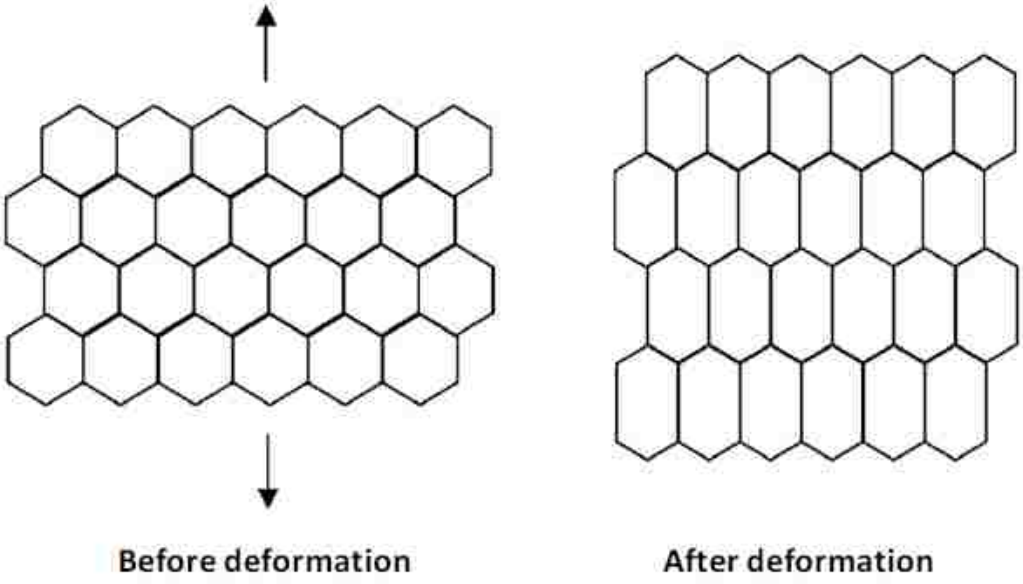

(b)

Figure 2.10 Schematic illustration of grain rearrangement during (a) Rachinger sliding [51] and (b) Lifshitz sliding [35]

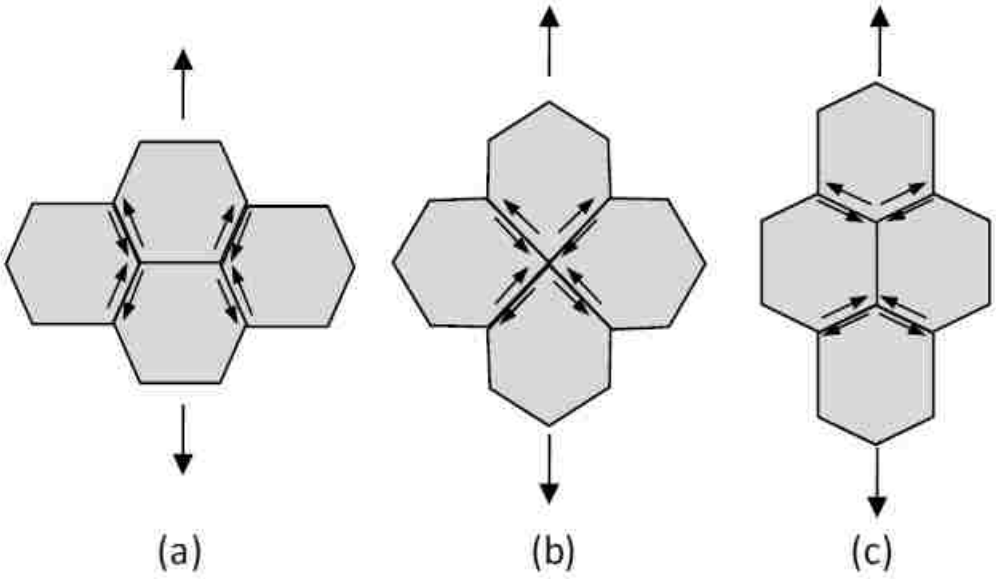

Figure 2.11 The principle of the model of Ashby and Verrall [36] for grain rearrangement by diffusion

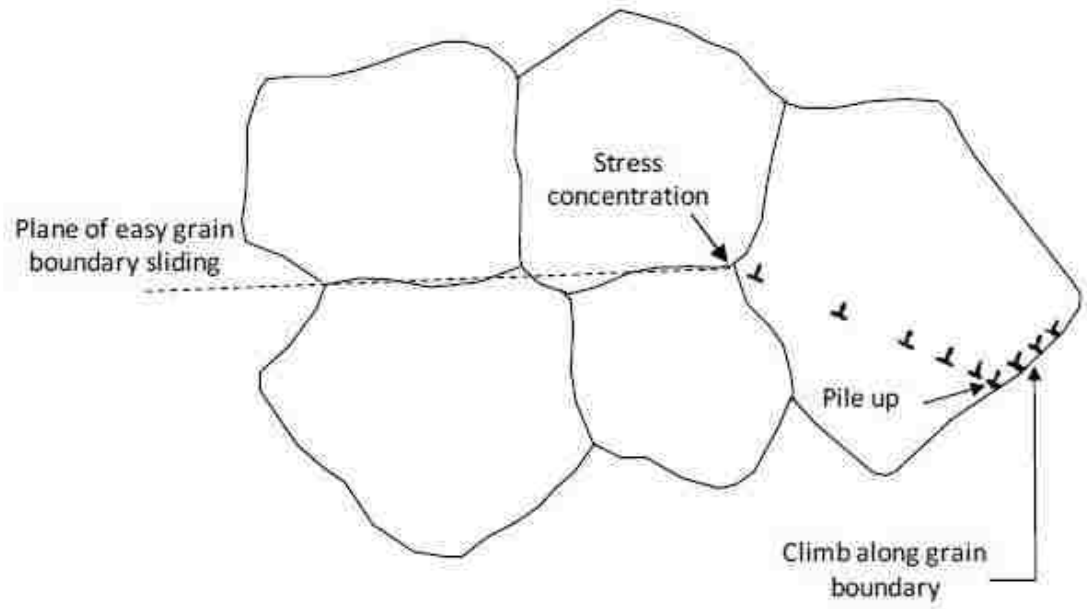

Figure 2.12 Schematic illustration of the mechanism of superplasticity developed by Ball and Hutchison [39].

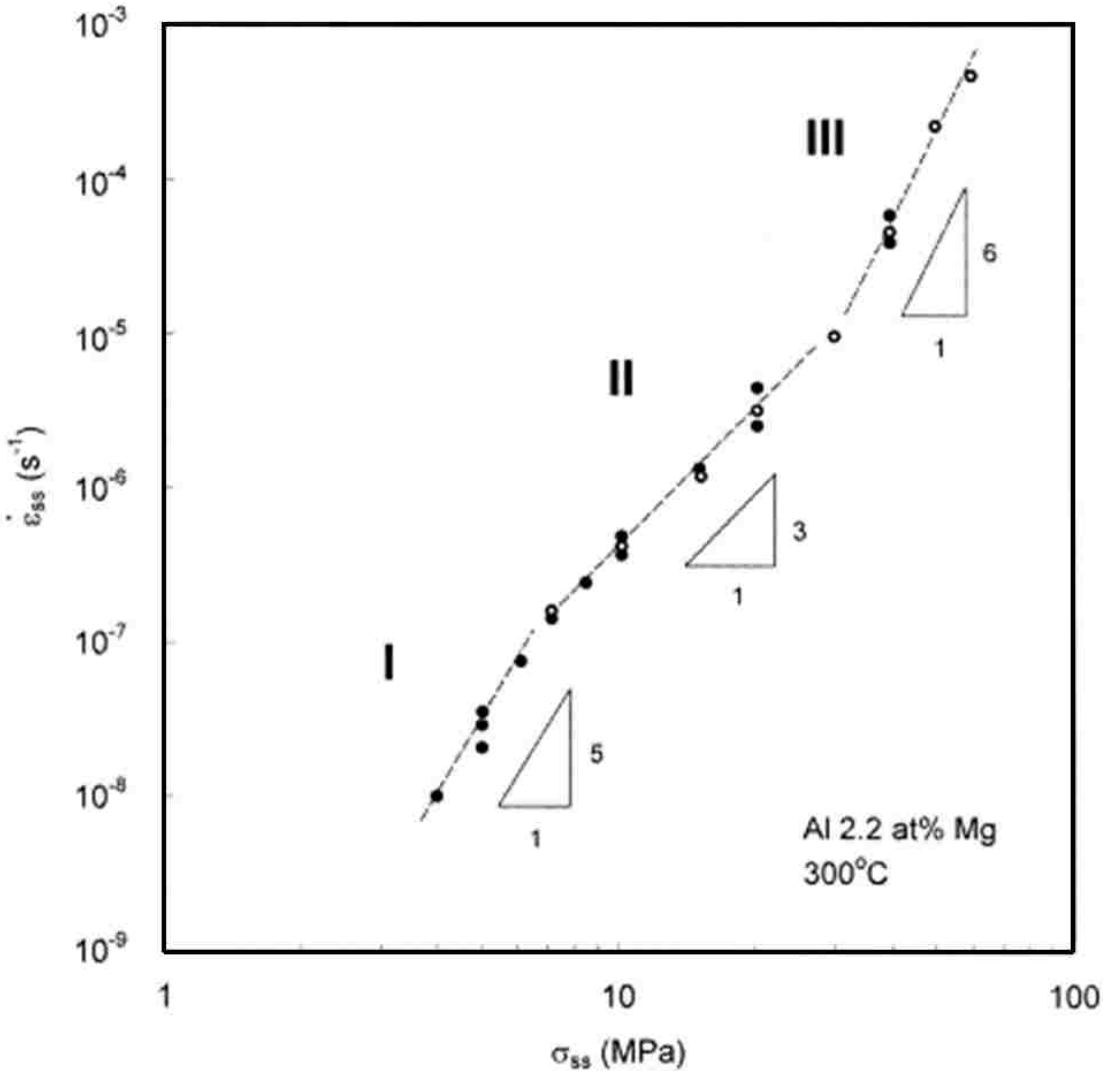

Figure 2.13 Steady-state creep rate versus applied stress for an Al-2.2at%Mg alloy at 300°C. Three different creep regimes, I, II, and III, are evident [33].

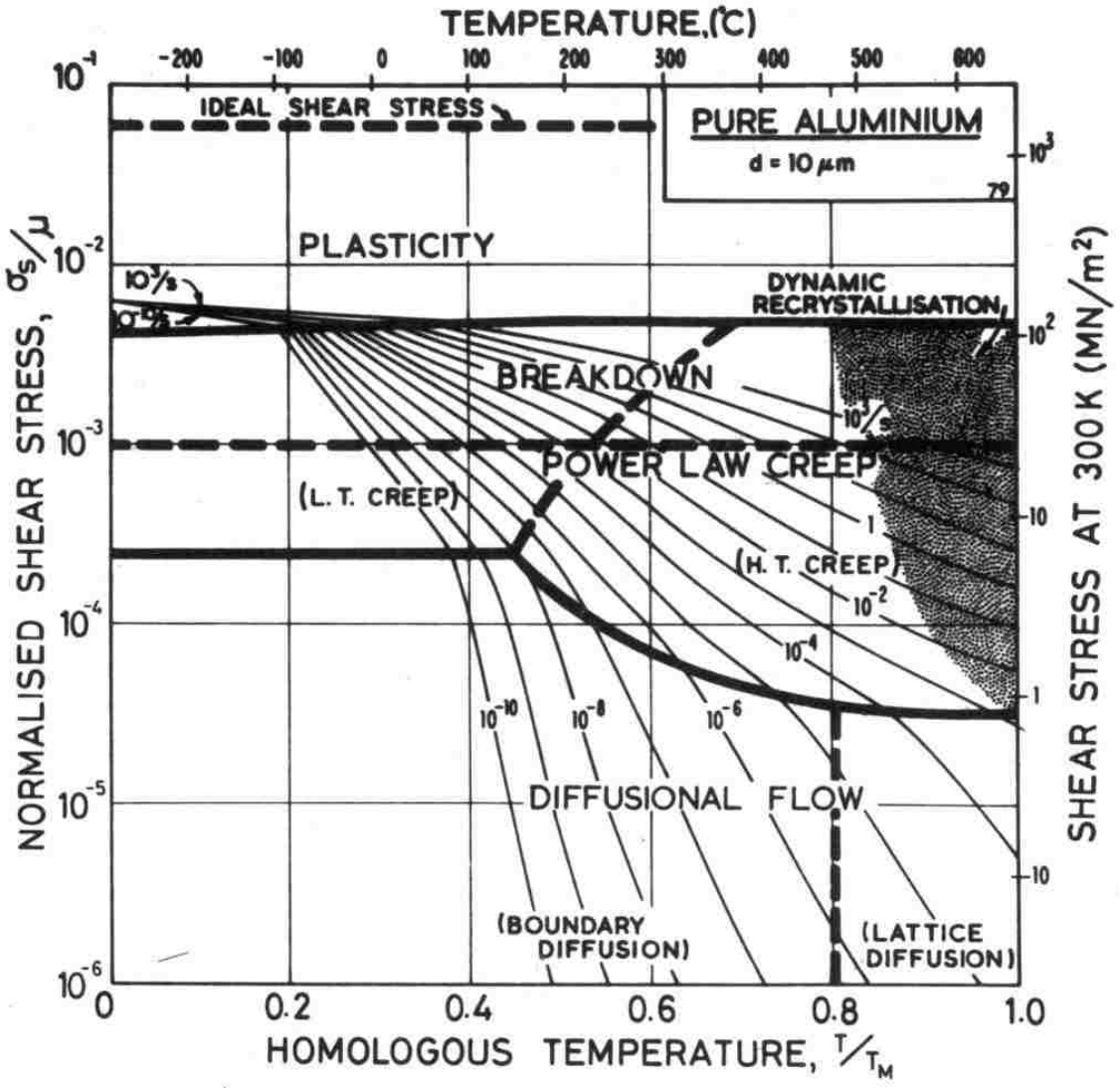

Figure 2.14 Deformation mechanism map (DMM) for pure aluminum of grain size 10 μm, showing boundary and lattice diffusion controlled diffusional flow, dynamic recrystallization and power law creep [42].

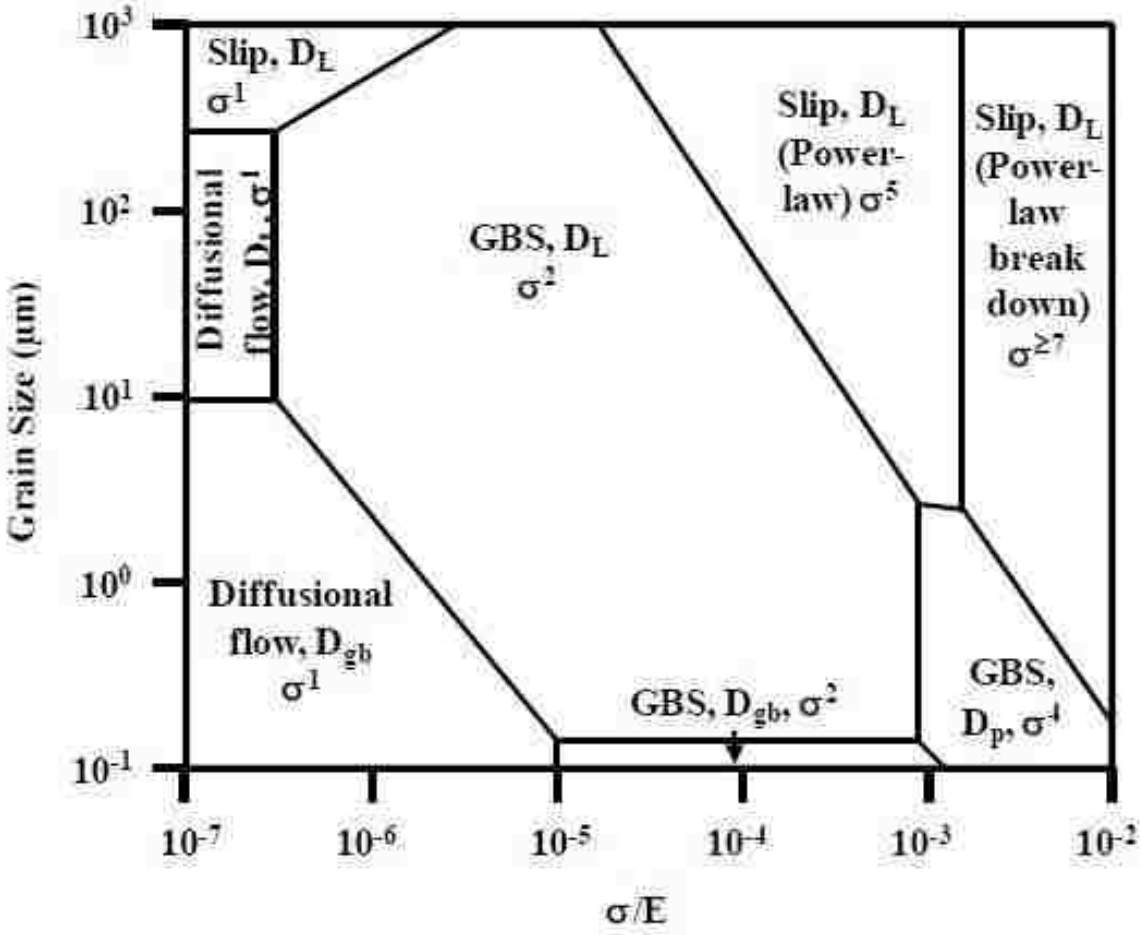

Figure 2.15 DMM for aluminum alloy at 800K [43].

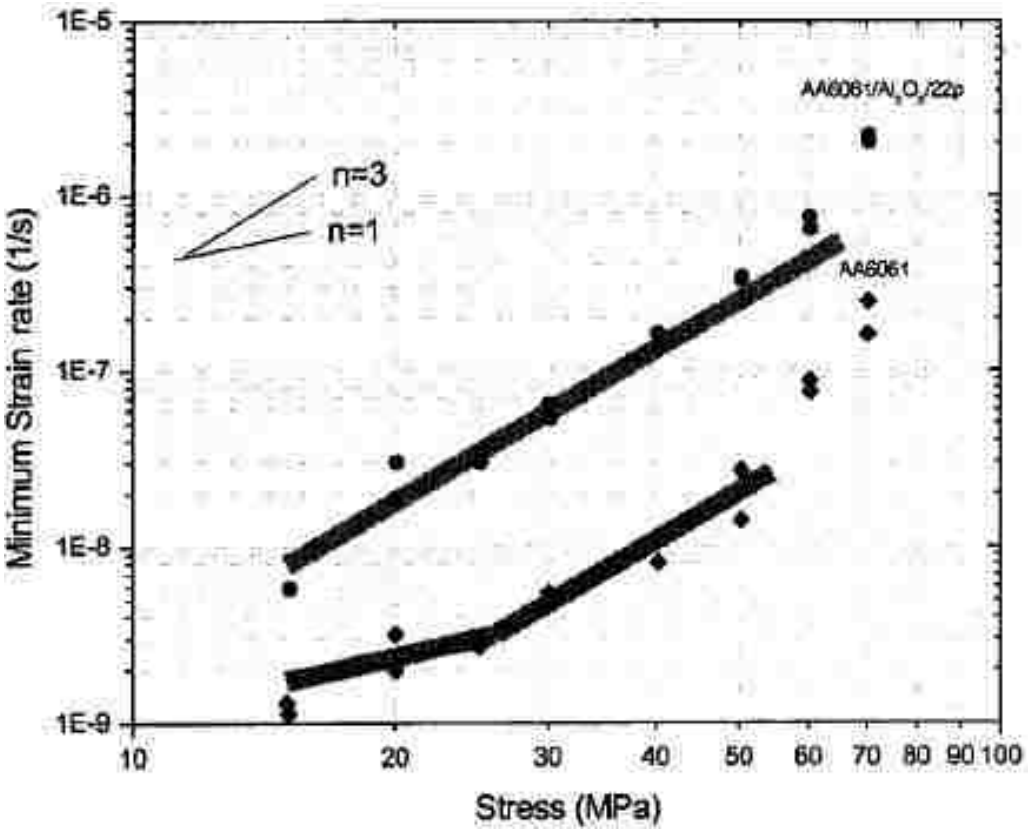

Figure 2.16 Minimum strain rate v. stress curves showing slopes for stress exponent n=1 and stress exponent n=3 [46].

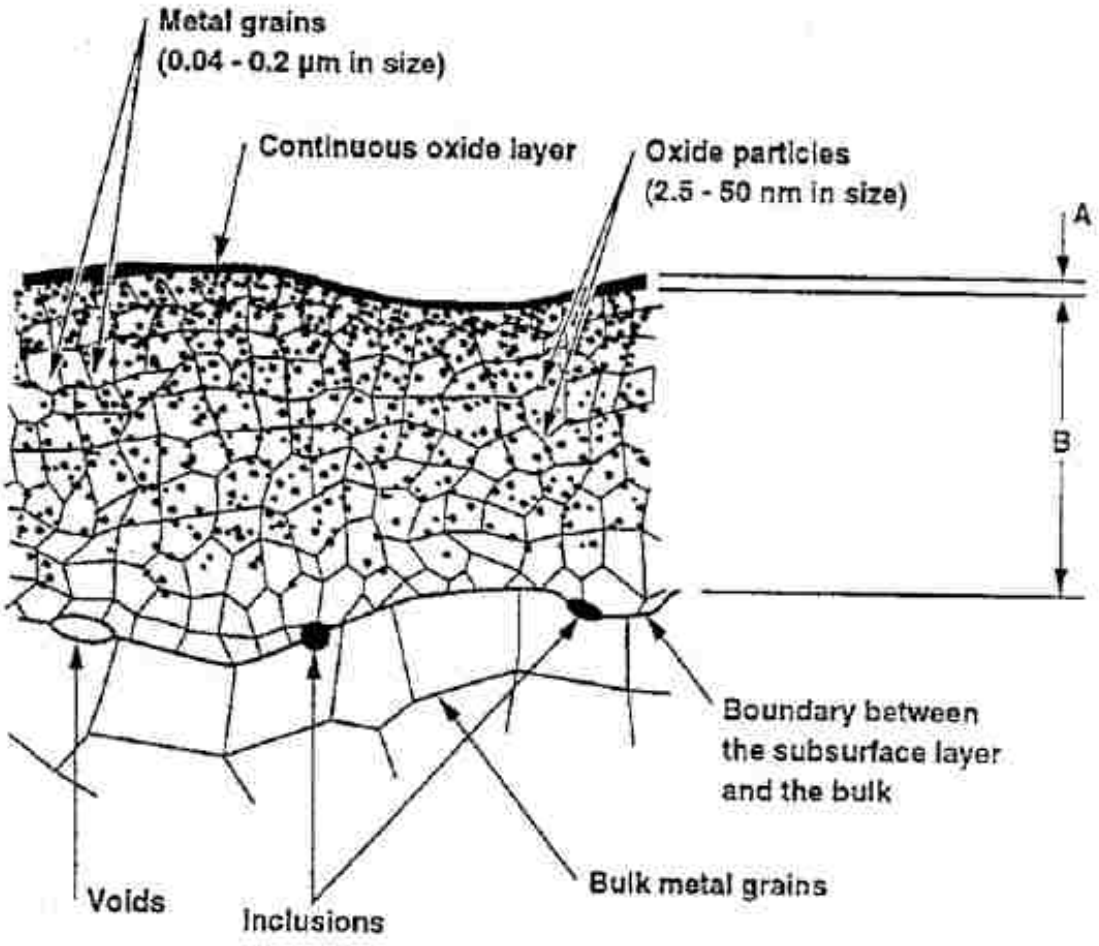

Figure 2.17 Schematic representation of the subsurface layer containing the microcrystalline oxides mixed with the small grained metal and covered with the continuous surface oxide: (A) thickness of the continuous surface oxide, 250 – 1600 Å; (B) thickness of the mixed subsurface layer, 1.5 – 8 μm [50].

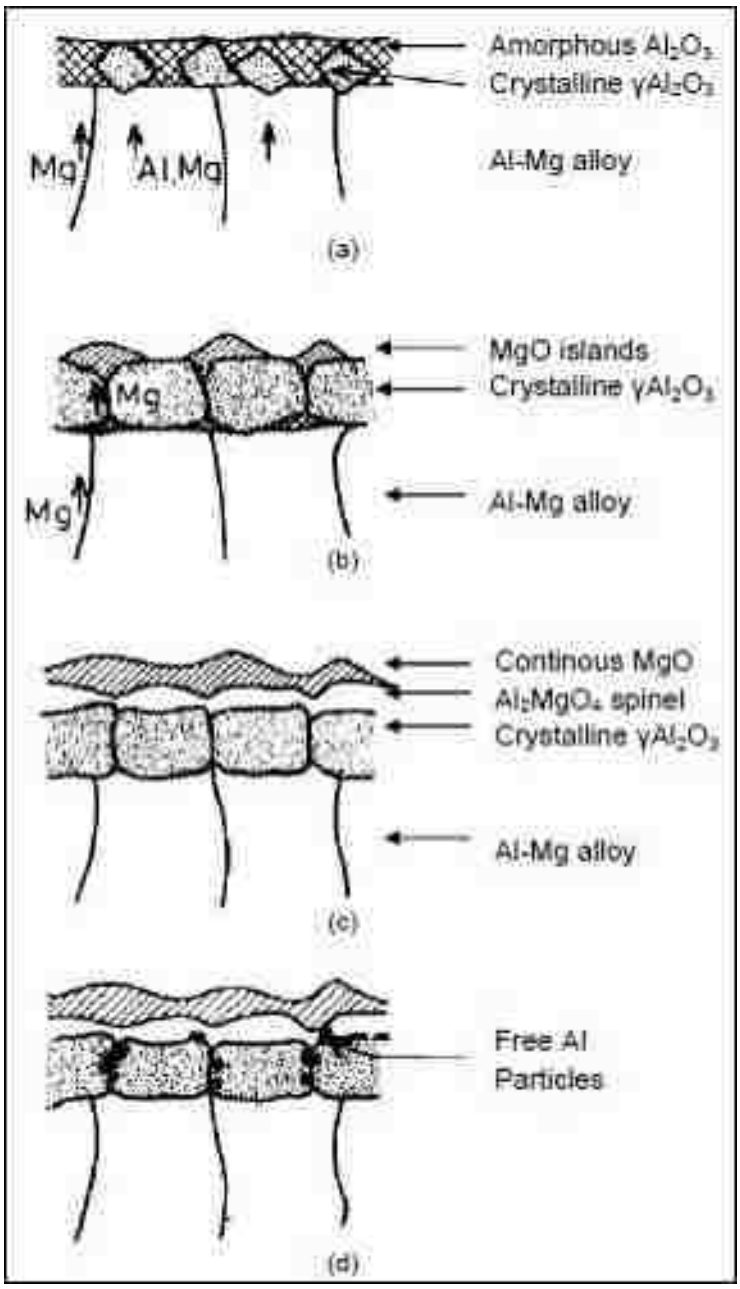

Figure 2.18 Schematic model of the growth of the oxide film on Al-Mg alloys during heat treatment [57] – (a) oxide crystallites nucleate and the thickness increases by grain boundary diffusion of aluminum and magnesium to the free surface, (b) The difference in diffusivity of the species ensures that the surface becomes magnesium-rich and MgO islands forms on the surface, (c) Al_2O_3 in the film is reduced by the outwardly diffusing magnesium to form the spinel MgAl2O4, and (d) this leaves free aluminum within the oxide and also leaves MgO islands that join to form an aluminum-free surface.

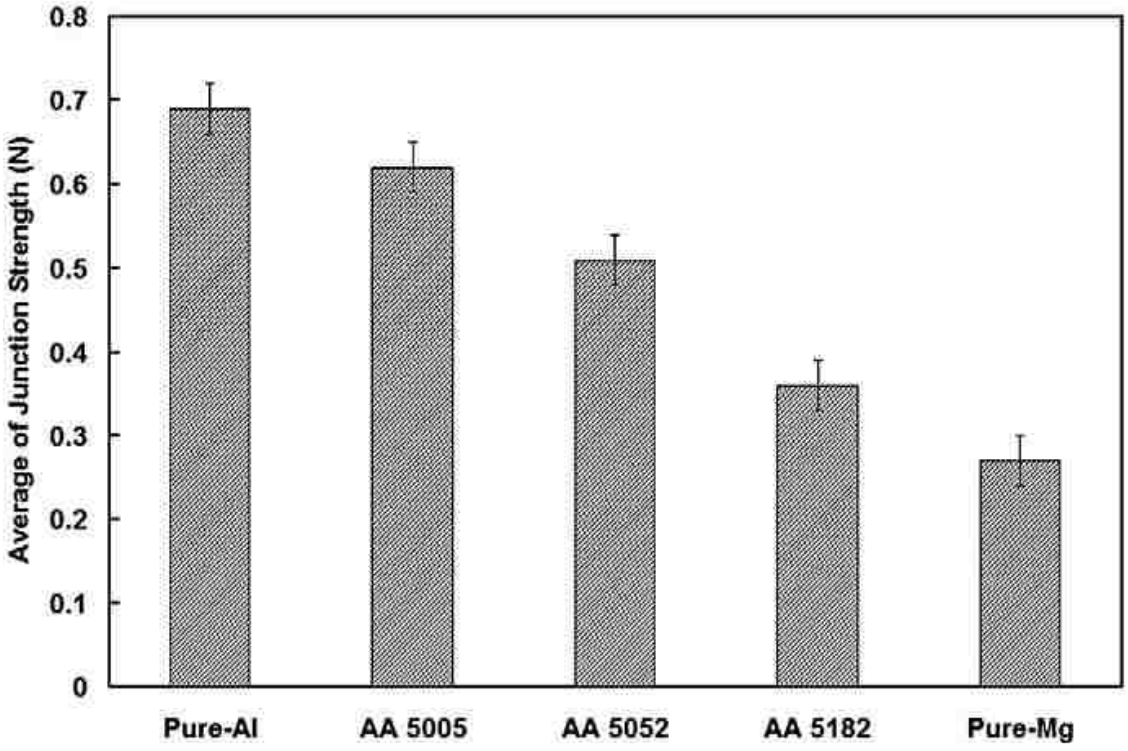

Figure 2.19 The average value of junction strength for each alloy (maximum tangential stress reached before the failure of adhesive junction) [59].

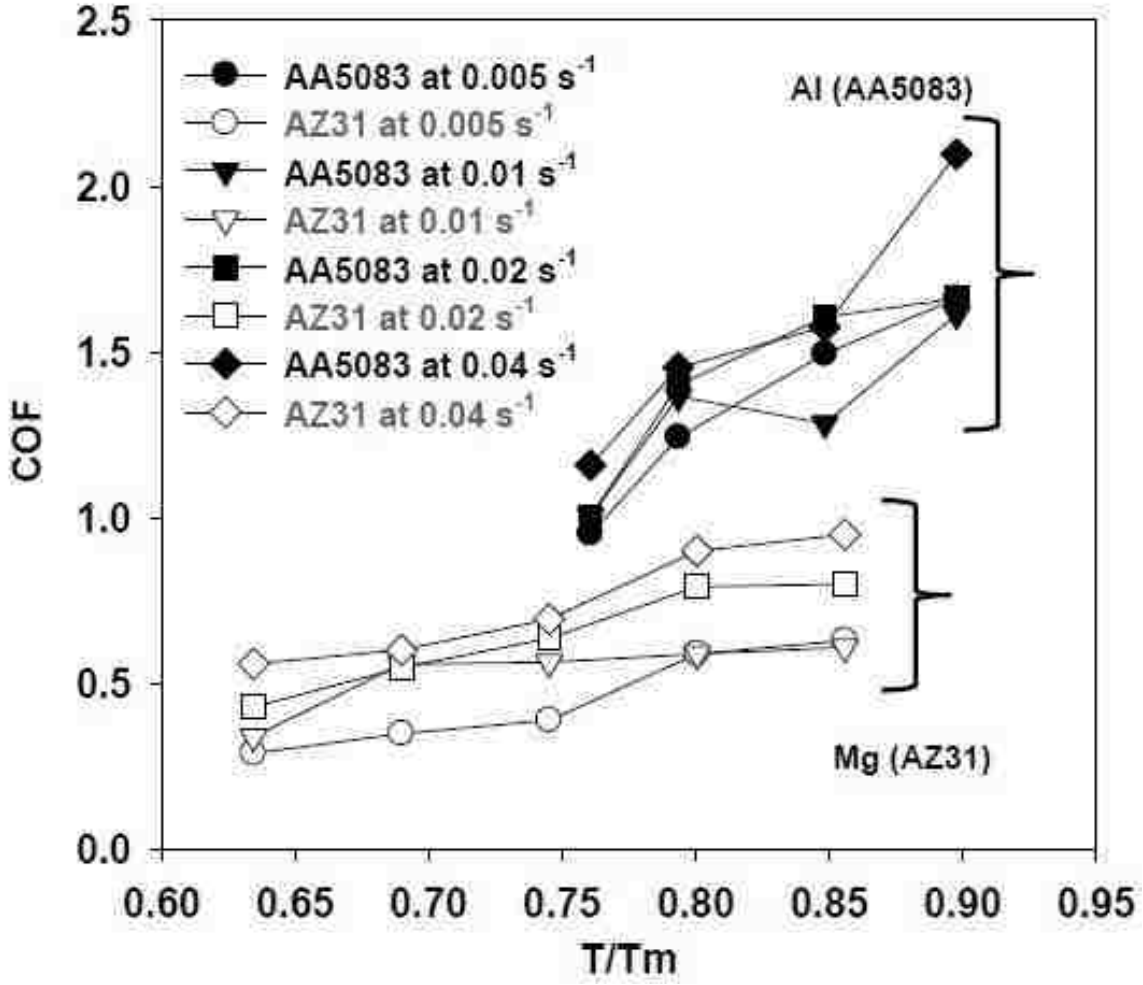

Figure 2.20 COF of AA5083 and AZ31 alloys for same homologous temperatures at different strain rates [61].

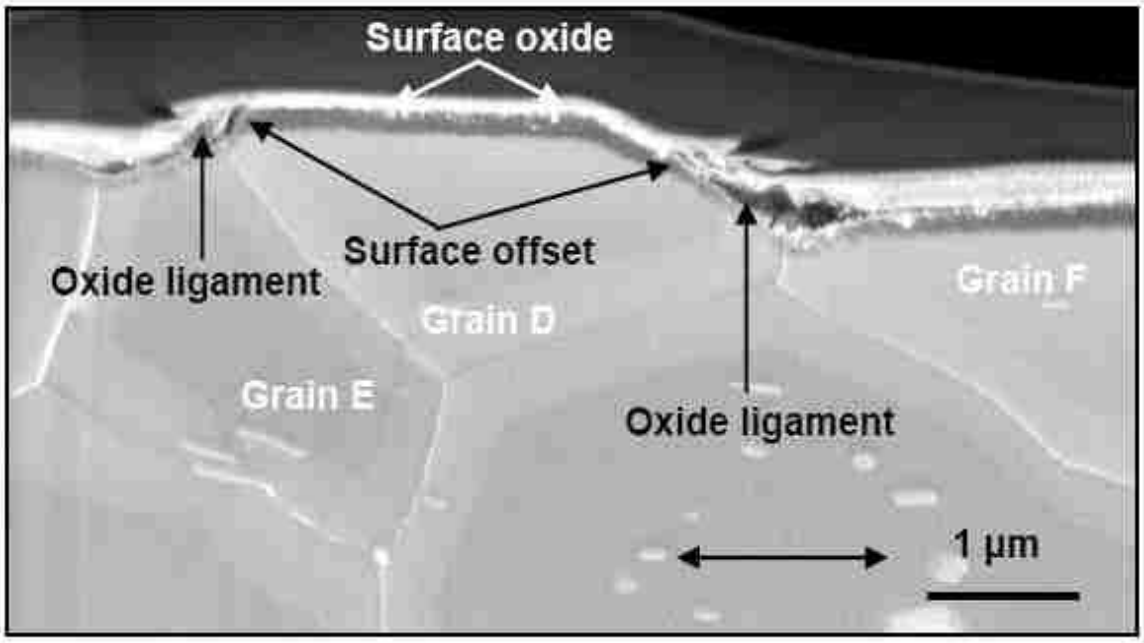

Figure 2.21 FIB cross-section of deformed surface taken along the tensile axis to illustrate the superplastic ligament formed at the surface offset that resulted from GBS [61].

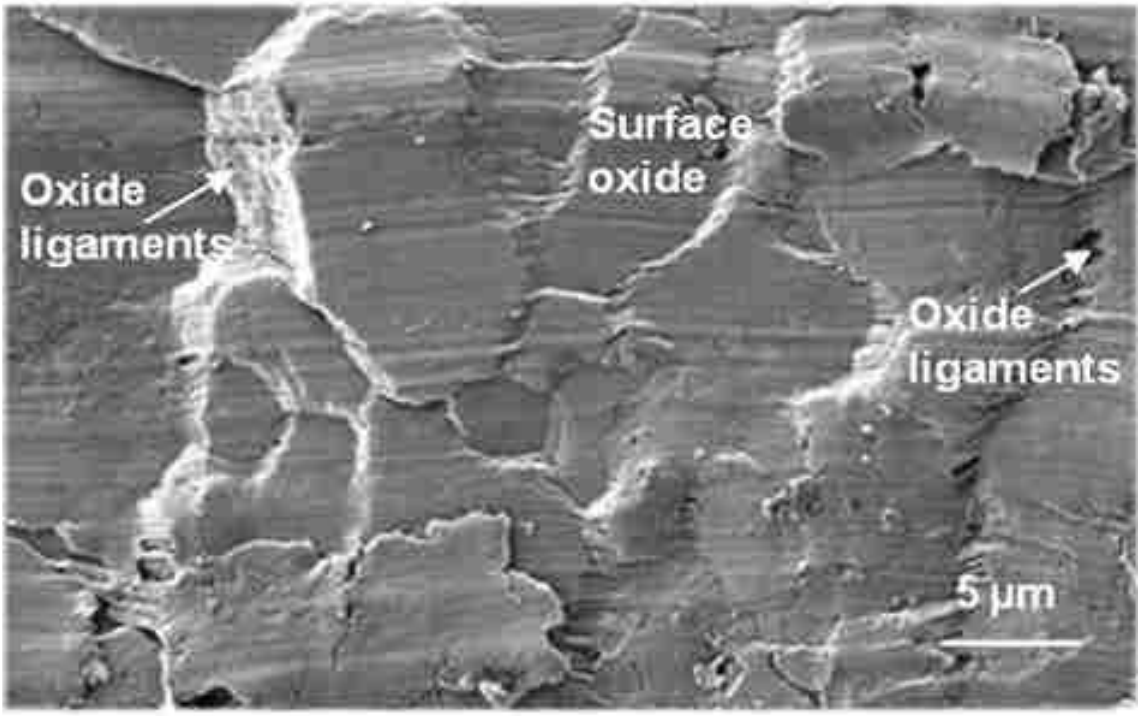

Figure 2.22 Surface morphology of the strip deformed at T = 818 K (545 ^{o}C) and dϵ/dt =4 x $10^{-2}s^{-1}$ [26].

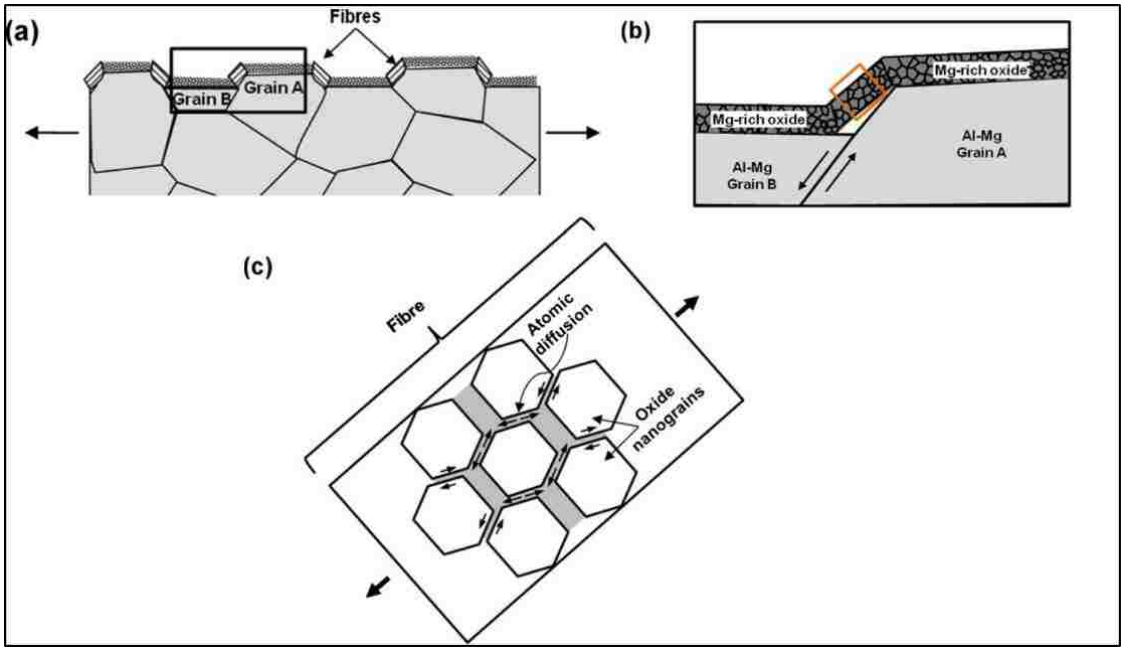

Figure 2.23 Schematics showing (a) GBS of bulk Al-Mg grains leads to the formation of steps at the surface. (b) Surface step formed at the grain boundary due to relative sliding between grain A and grain B of Al-Mg, and the tribo-layer above the grains stretched over this step generating a fibrous structure. (c) Suggested microscopic process responsible for the formation of fibres from the tribo-layer on the surface of the hot deformed AA5083 alloy (representing the magnified view of the fibres in the box shown in plate (b)) [62].

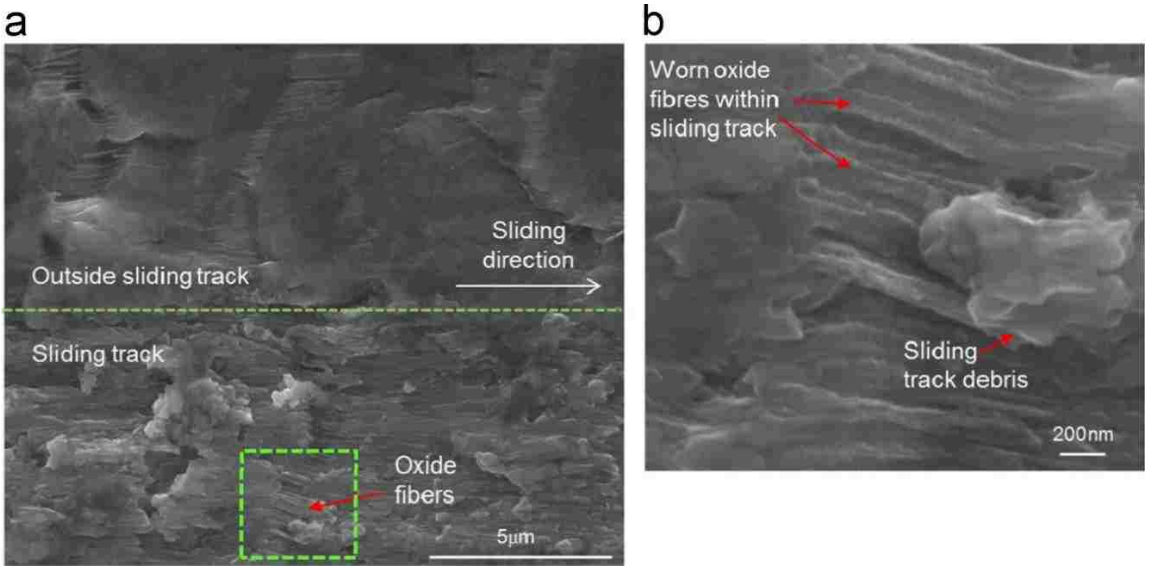

Figure 2.24 Secondary electron images of (a) oxide fibres located within the sliding track generated on the as-receivedAA5083 aluminium alloy at 545 ^{o}C and also shows the fibres formed on the tribolayer surface outside the sliding track (b) higher magnification image of boxed area in (a) which shows sliding debris lying on the oxide fibres [31].

CHAPTER 3: EXPERIMENTAL METHODOLOGY

3.1 Introduction

In this chapter, experimental details are described. These include i) heat treatment of the workpiece, ii) hot forming experiment, iii) measurement of adhesion strength using junction strength experiments, and iv) surface characterization techniques employed to investigate the deformed and worn surfaces. An outline of the experimental methods used in this work is shown in **Figure 3.1** and **Figure 3.2**

3.2 Hot forming experiments

3.2.1 Heat treatment of the workpiece

The wrought alloy was an aluminum-magnesium-silicon alloy, AA6061, with the composition given in **Table 3-1**.

Table 3-1 Composition of alloy under investigation, wt-% (AA6061)

Component	Al	Cr	Cu	Fe	Mg	Mn	Si
Wt. %	95.8-98.6	0.04-0.38	0.15-0.4	Max 0.7	0.8-1.2	Max 0.15	0.4-0.8

Samples were in the form of strips that were 5mm wide, 1mm thick and 150mm long. The strips were annealed to reach the full annealing condition, which is the softest, most ductile, and most workable condition of heat-treatable alloys. The annealing consisted of the following steps:

i. Heating of the strip to 415^{o}C for 3 hours,

ii. Furnace cooling to 260^{o}C using a cooling rate of 80^{o}C/h,

iii. Air cooling to room temperature.

The strips were tested in two conditions, one set of samples was unpolished strips with tribolayer, and the other one was polished strips in which the tribolayer was removed.

The unpolished state indicated that no work has been performed on the surface. It is expected that such strips possess a tribolayer from previous high temperature processing operation like hot rolling. This is therefore a high concentration of oxides on the surface of the strips. The cross-sectional SEM image of the AA6061 alloy is shown in **Figure 3.3**, and the average of the thickness of the tribolayer is 1.63 ± 0.26 μm. The polished state indicated that the surface was polished to a 1μm mirror surface, and all previous processing and oxides has been removed from the surface.

3.2.2 The counterface material

The counterpace was a cylindrical P20 steel pin with the dimensions 25mm length and an 11.5mm diameter see **Figure 3.4**. P20 tool steel is a typical die material used for forming of aluminum sheets. The length of the pin was divided into four sections of 5mm each with a spacing of 3 mm between sections. The pin sections were polished to 1um. The composition is given in **Table 3-2**.

Table 3-2 Composition of counterface P20 steel, wt-%

Component	C	Mn	Si	Cr	Mo	Fe
Wt. %	0.40	1.00	0.40	1.20	0.35	Bal

3.2.3 Laboratory simulation

3.2.3.1 Description of the hot forming simulator

The hot forming process was simulated with the use of a high temperature tribometer. A polycarbonate cover was constructed to enclose the setup to generate a controlled testing atmosphere. The tribometer stretched the AA6061 strips and simulated

the sliding contact between the die and the workpiece. The tribometer consisted of four assembly parts (**Figure 3.5**), which are described as follows:

1. A loading system that consists of two linear actuators, and each of them connected to one end of the strip to be tested. The actuators can apply tensile stress along the longitudinal axis of the strip at the required strain rate. The tensile load in each test was measured using a load cell (Omega LCMCD-100) with a sensitivity of ± 0.1N attached on the strip holder.

2. COF measurement assembly (**Figure 3.6**) made up of force measurement system which consisted of another load cell with a sensitivity of ± 0.5N, and heating system. The strip was heated while passing through the stainless steel roller heated using a 500W cartridge heater inserted inside the roller. Three thermocouples were inserted in the holes inside the roller. The strip temperature during experiments was determined from the average reading obtained from these three thermocouples. The hot roller was installed in a bearing system which allowed to rotate freely, and a boron nitride lubricant was applied to its surface to reduce the friction.

3. A camera system that records the in-situ deformation of the grids inscribed on the sample surface.

4. Polycarbonate cover was installed to enclose the tribometer to generate controlled atmosphere (**Figure 3.7**). Argon gas was injected in the chamber, and the relative humidity inside was monitored by a humidity sensor.

3.2.3.2 COF measurements (Air and Argon)

Friction tests were performed in air and an argon atmosphere to determine the effect of atmosphere on friction at elevated temperatures. The experimental conditions is given in **Table 3-3**

Table 3-3 Experimental conditions

Temperature (℃)	Strain rate (s^{-1})	Sample (annealed AA6061)	Pin (polished)	Normal load	Atmosphere
350-545	0.01-0.04	Unpolished Polished	P20 steel	22g	Air Argon

By using the experimental setup described above, the COF was obtained during the sliding contact motion. The strip was cleaned with acetone prior to each test. Then the strip`s ends were connected to each of the two actuators (a slave and a master), passing it over the stainless steel roller which rotates freely. The strip was then heated to 350^{o}C, 400^{o}C, 450^{o}C, 545^{o}C with the contact of the bottom face with the hot roller, it was allowed to slide and stretch by the actuators. The pin, which was connected to a load cell, was then brought down into contact with the top face of the strip. The load cell collects data and transmits data to the data acquisition system (InstruNet), with the use of calibration equation, COF graphs can be plotted.

For tests in an argon atmosphere, the argon gas was injected inside the chamber and the atmosphere inside the chamber was monitored by a humidity sensor. Friction tests were initiated when the required temperature was attained and the reading of the humidity sensor decreased to zero.

3.2.3.3 Stretching tests

A series of 'non-contact' tests were performed by using the same high temperature simulator to measure the flow stress of the strip at elevated temperatures at the strain rates used in the friction test to determine the stress exponent. The deformation mechanisms of the annealed AA6061 at elevated temperatures and different strain rates ($1x10^{-2}$ s^{-1}, $2x10^{-2}$ s^{-1}, $3x10^{-2}$ s^{-1}, $4x10^{-2}$ s^{-1}) were determined by analysing the creep data and the micrographs.

The major and minor strains in the hot zone were measured from the changes in initial diameter (2.5mm) of circular grids inscribed on the top surface (**Figure 3.8**). The calculated major and minor strain from two consecutive grids at the hot zone are shown in **Figure 3.8**. The instantaneous (true) strain rate for the strip at 545 °C for the test shows in **Figure 3.9** was $d\varepsilon/dt = (\varepsilon_1 - \varepsilon_2)/\Delta t = 4.05 \times 10^{-2}$ s^{-1} (where Δt = 2s).

3.3 Adhesion force measurement by junction strength experiments

In order to understand the localized junction formation due to material adhesion and transfer during the sliding experiments, junction strength tests of AA6061 were performed in air and argon atmospheres to study the effect of atmosphere on junction strength. In addition to AA6061, the adhesion behaviour of oxides formed by using alloys with increasing Mg content were also investigated.

The experimental setup used for the adhesion tests in this work is a pin-on-disc tribometer (**Figure 3.10**), and the junction strength tests were performed using cylindrical pins that were 14 mm long and having a diameter of 4.5 mm. One end of each sample was machined to a hemispherical shape with a 2.1 mm radius, then polished to a surface roughness of 0.15um. The tip radius of the pins was 50 ± 3 um. The pins were fabricated

from the following alloys: AA1100, AA6061, AA5083, and AZ91. The composition of each alloy is listed in **Table 3.4**.

Table 3-4 Composition of the Al-Mg alloys

Alloy	Mg wt.%	Al wt.%	Zn wt.%	Mn wt.%	Fe wt.%	Cu wt.%
AA1100	0.00	>99	<0.10	<0.05	<0.95	0.05-0.20
AA6061	0.80	95.8	<0.25	<0.15	<0.70	0.15-0.40
AA5083	4.80	92.4-95.6	<0.25	0.40-1	<0.40	<0.10
AZ91	90.2	8.9	0.91	0.20	0.0025	<0.0007

An M2 steel disc with a 25 mm diameter was used as the counterface. The surface roughness of the steel disc after polishing was 0.07μm. Prior to adhesion tests, the samples were ultrasonically cleaned in acetone for 15 min. Junction strength tests were operated at a typical hot forming temperature which is 420^{o}C. Each sample was heated by a cartridge heater (Omega css-01235/120V 35W) embedded inside the sample holder, while a 0.5mm diameter thermocouple was inserted into the side face of the sample holder to measure the temperature of the alloy. The sample was heated to 450^{o}C, the counterface M2 steel was not heated. The samples were held at the test temperature for 600s. Then their tip was pressed against the steel surface under a normal load of 0.5N. After a short, initial static contact period of 10s, the steel counterface rotated at a very slow velocity (8.75 μm/s). The tangential force required to initiate the sliding of the steel counterface was recorded using a load cell with a sensitivity of ± 0.01N. The maximum value of force represents the force required to break the asperity junction formed at the first contact and hence termed as 'junction strength' [14, 27]. The change in the tangential force, Ft, was measured

throughout the experiment. The deformed pin tip and steel counterface were analysed by using optical microscope, SEM, and EDS methods.

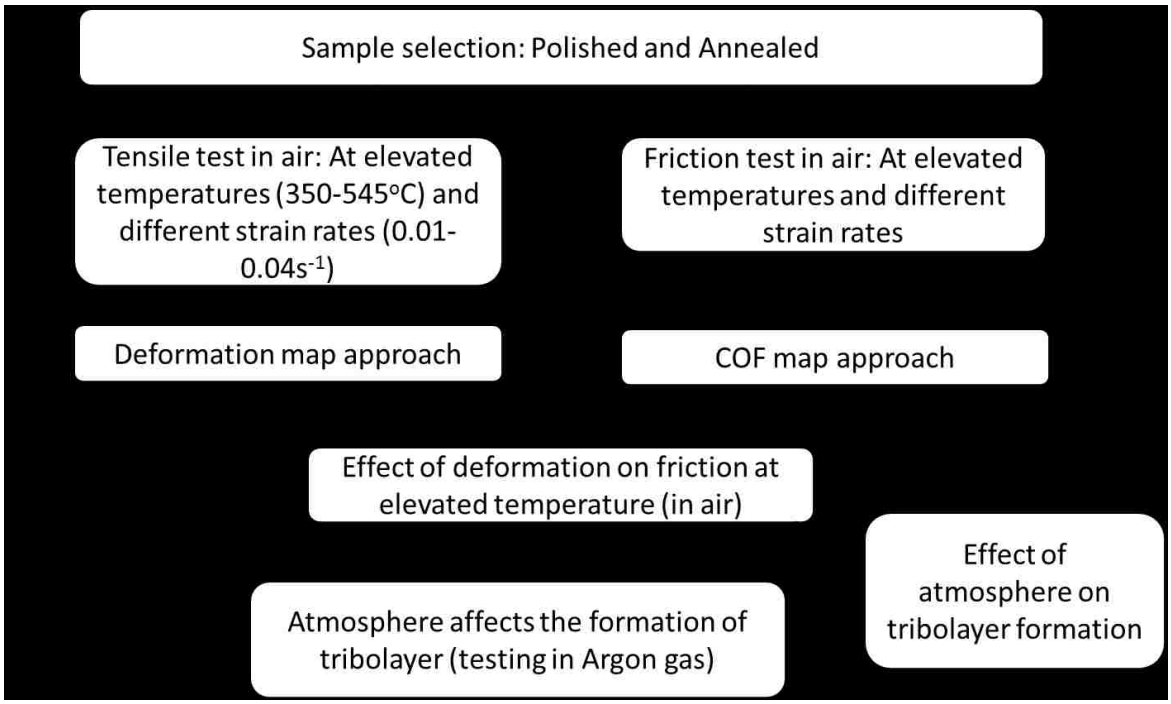

Figure 3.1Experimental methodology of the hot forming test.

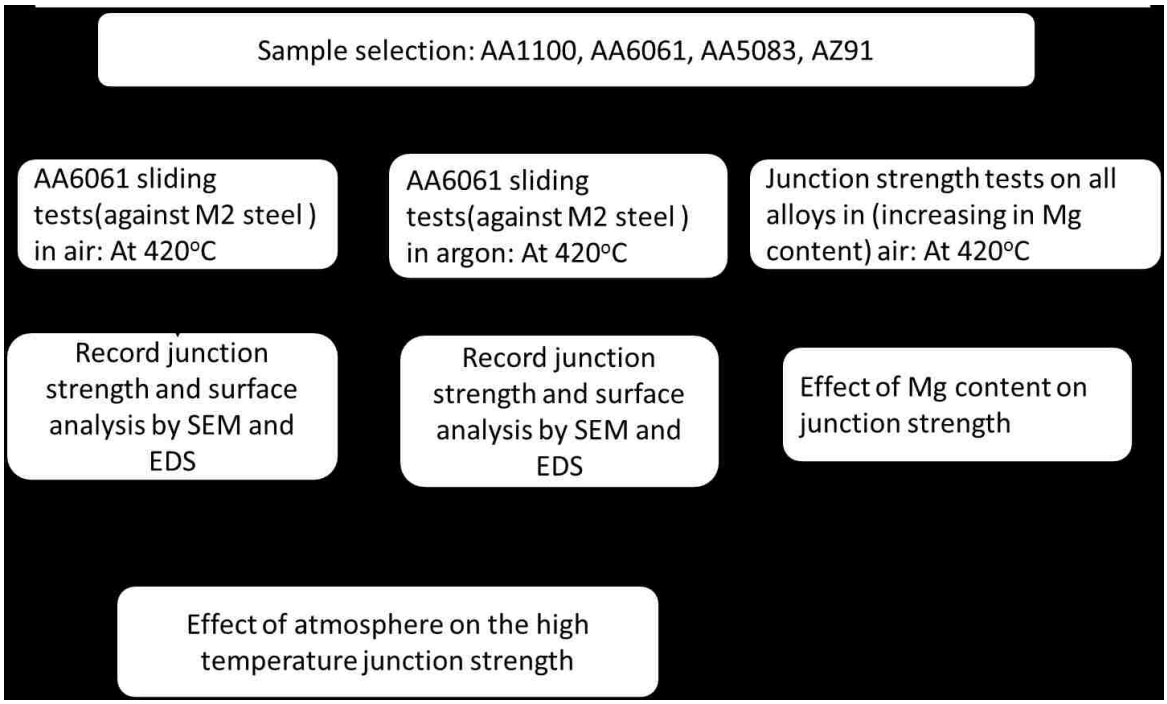

Figure 3.2 Experimental methodology of the junction strength test.

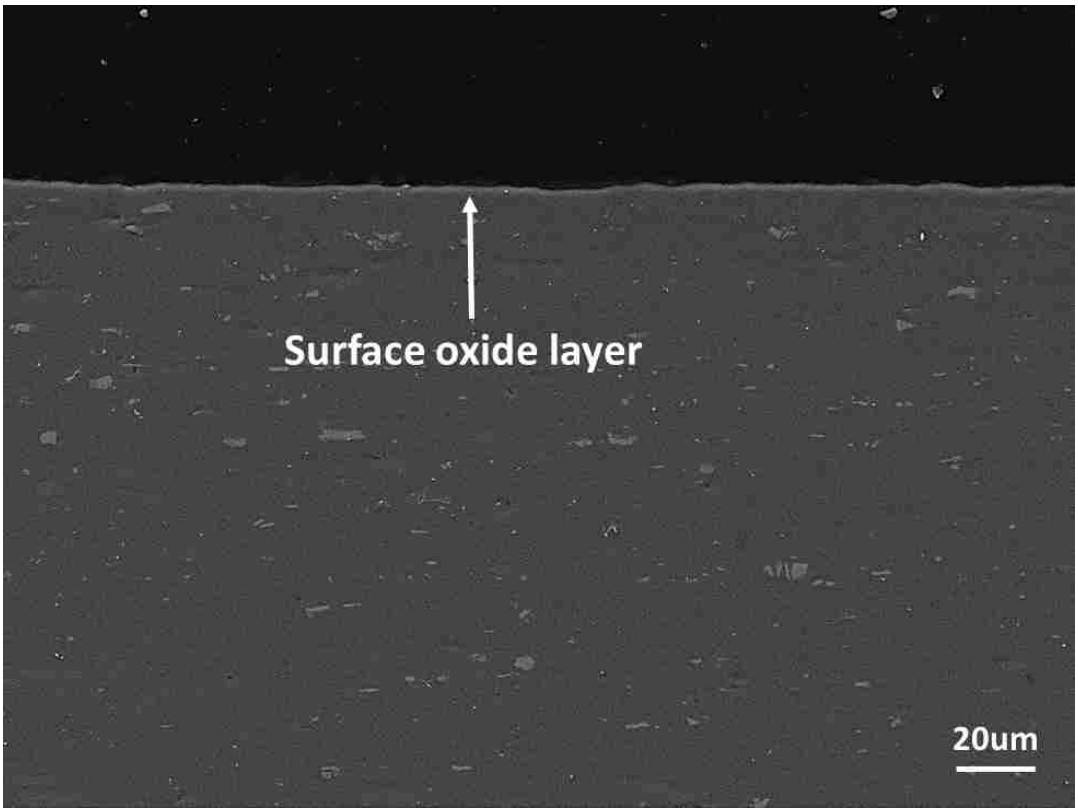

Figure 3.3 Cross-sectional SEM image of AA6061 alloy showing the tribolayer covered on the surface.

Figure 3.4 Image showing the polished pin used in the friction tests

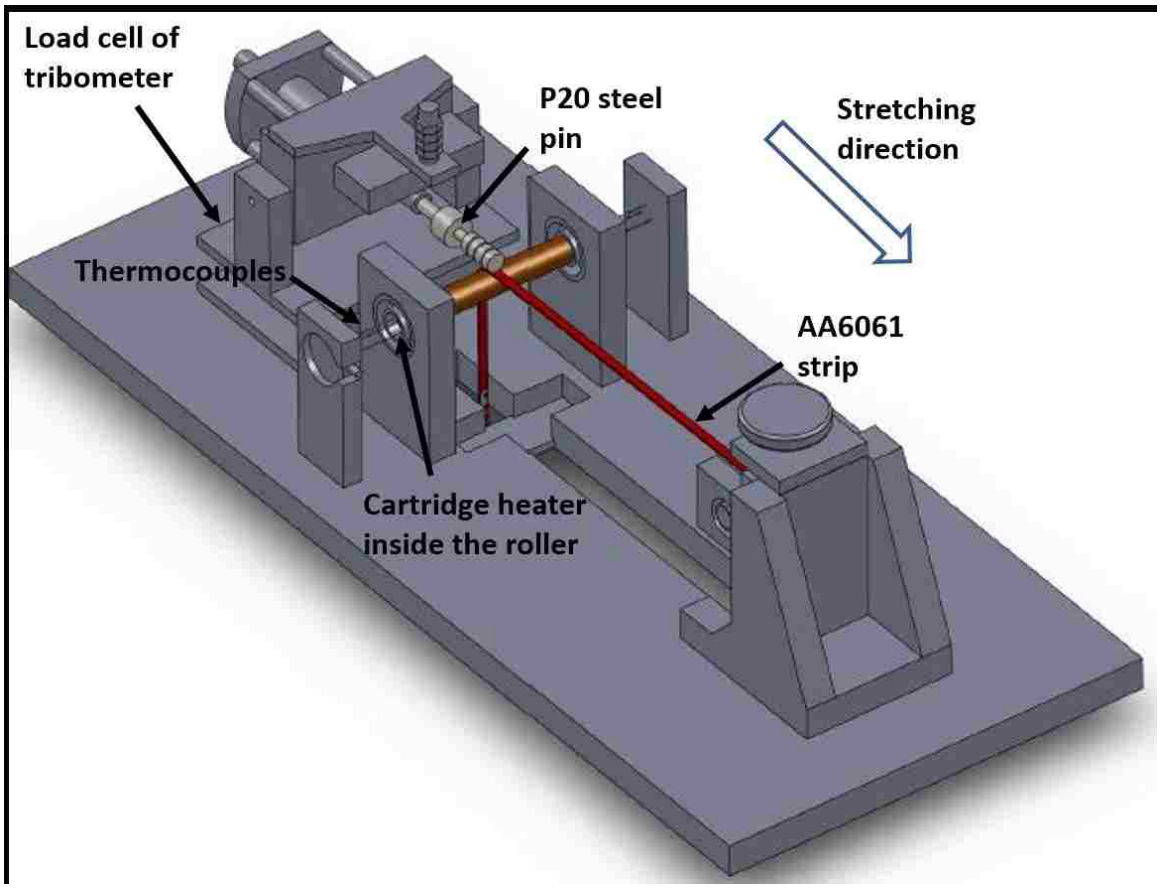

Figure 3.5 Schematic of the experimental setup that shows the AA5083 strip under sliding contact against the P20 steel pin being stretched by the linear actuators.

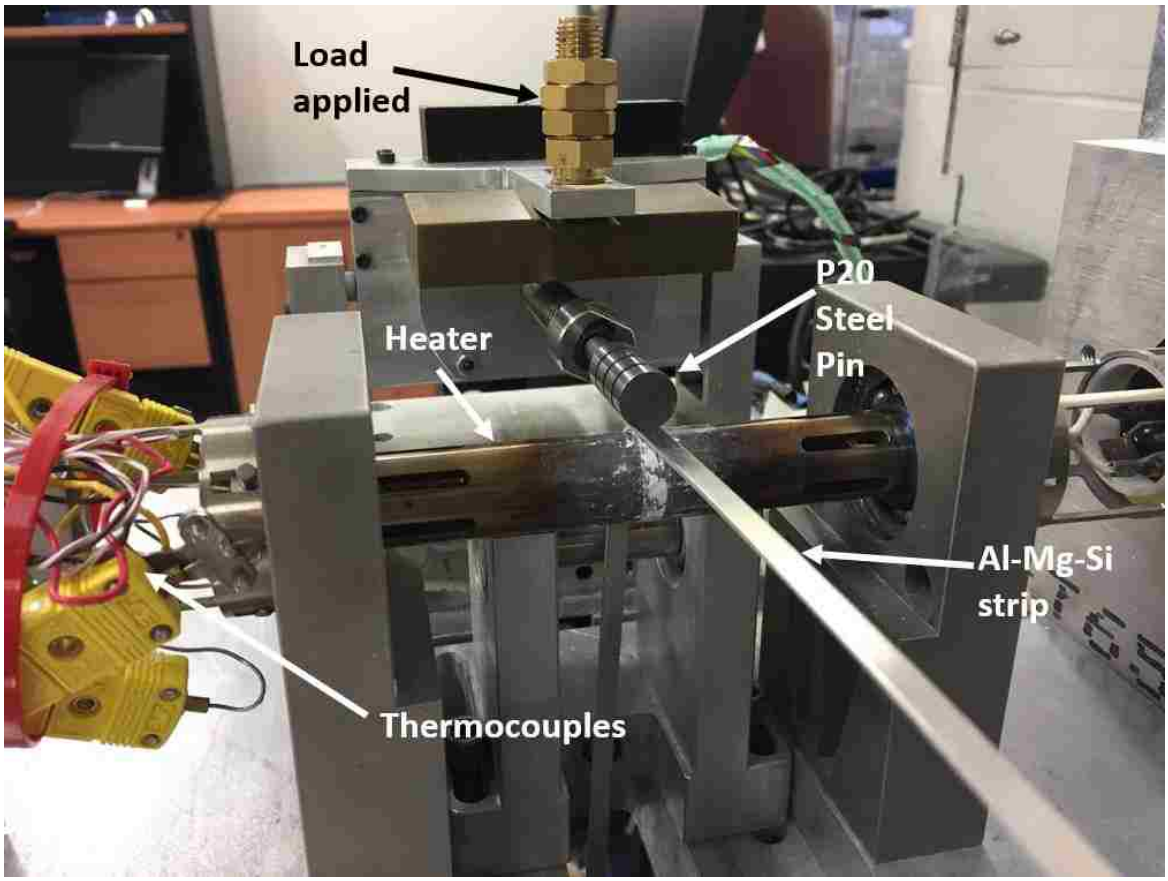

Figure 3.6 Photograph of the tribometer and heater assembly.

Figure 3.7 Photograph of the installation of the chamber on the tribometer.

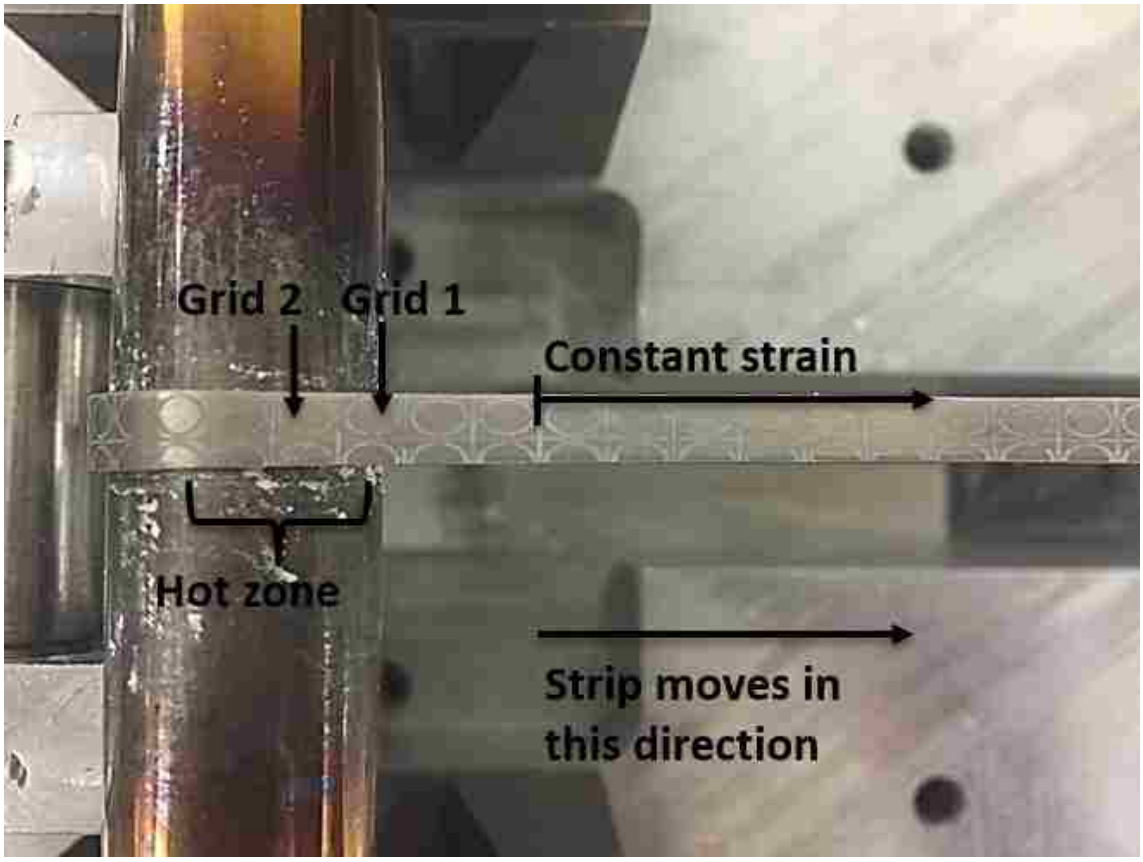

Figure 3.8 AA6061 strip inscribed with grids that shows elongation along the direction of the applied strain while being pulled.

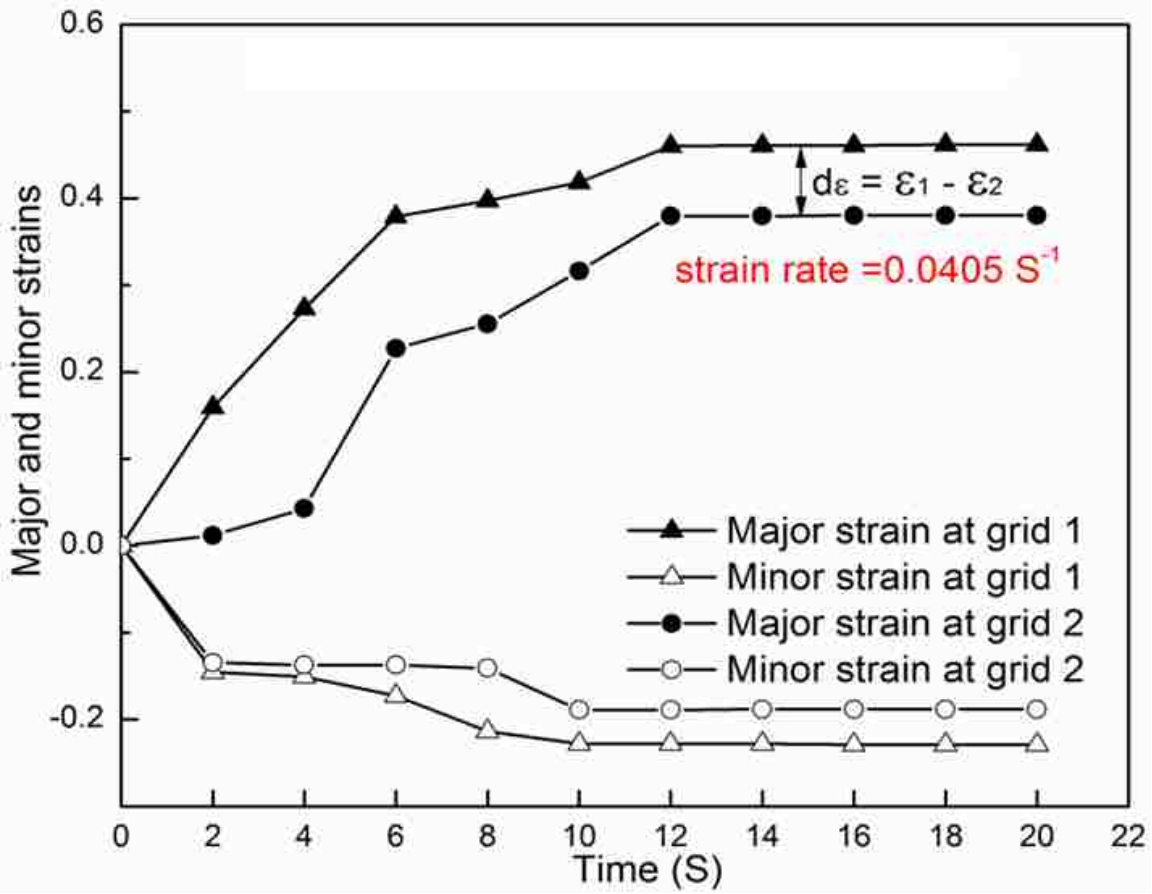

Figure 3.9 Major and minor strain of the AA6061 strip, measured from two consecutive grids (shown in Figure 3.6) within the hot zone (constant high temperature zone).

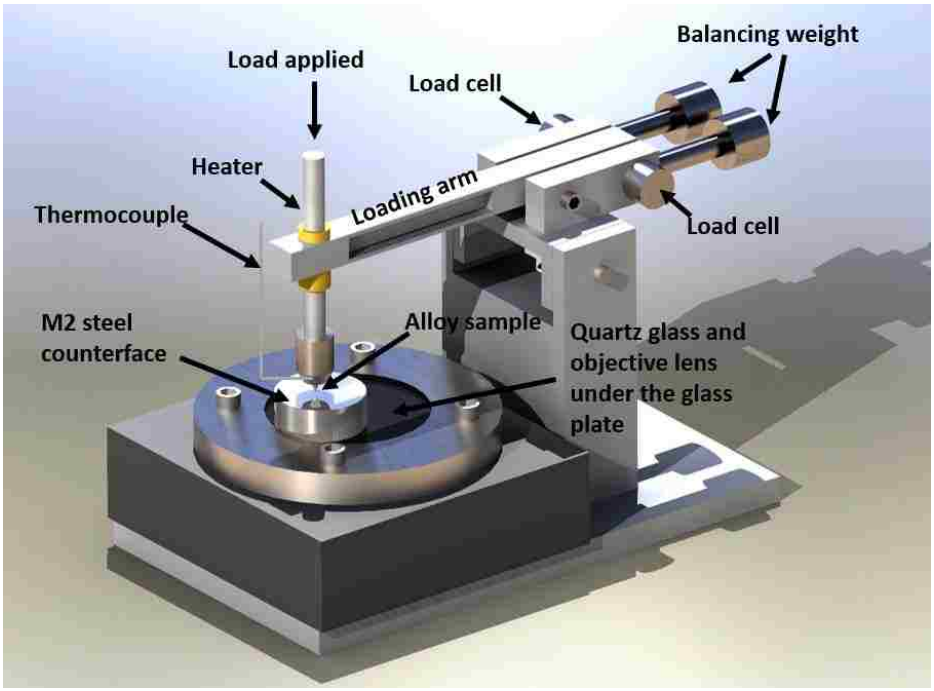

(a)

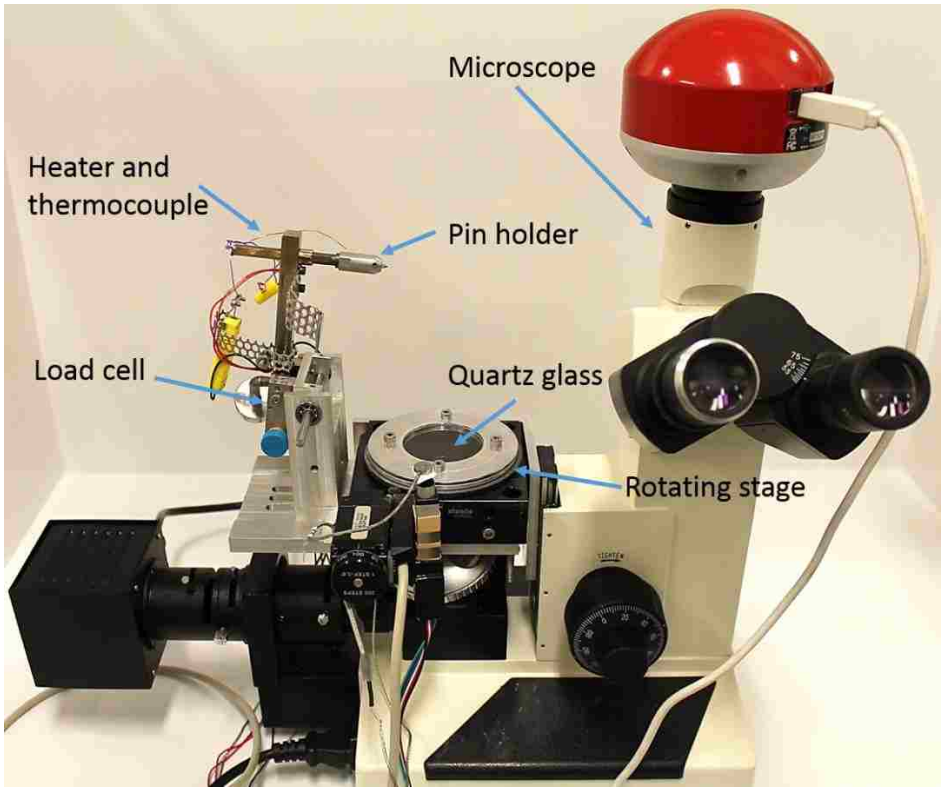

(b)

Figure 3.10 (a) Schematic view of setup and (b) Experimental setup for junction strength experiment.

CHAPTER 4: RESULTS

4.1 Introduction

This chapter presents the results of experiments performed in order to study: (1) the properties of interface generated between the AA6061 alloy and the P20 steel counterface under a dynamic loading conditions generated under high temperatures and different strain rates (2) the effect of the atmosphere on junction strength and adhesion (3) and the effect of Mg content on junction strength and adhesion.

The high temperature tribological experiments were performed at temperatures between 350 °C and 545 °C, and strain rate ranges between $1x10^{-2}$ s^{-1} and $4x10^{-2}$ s^{-1}. The purpose of these experiments was to simulate conditions close to those in hot-forming operations, where the workpiece was subjected to tensile forces while undergoing sliding contact.

The friction experiments were also performed in argon at temperatures between 350 °C and 545 °C and at strain rate of $4x10^{-2}$ s^{-1}. The purpose of these experiments was to study the effect of atmosphere on the friction in comparison with the tests under the ambient conditions.

In order to understand the localized junction formation due to material adhesion and transfer during the sliding experiments at different atmospheres, the adhesive force measurements tests were performed at 420ºC in air and argon to study the role of the atmosphere on the formation of surface oxides that control the friction and material transfer occurring during initial sliding contact between samples and counterface. In addition to

AA6061, the adhesion behaviour of oxides formed by using alloys with increasing Mg content were also investigated to study the effect of the Mg content on junction strength.

4.2 Variation of COF with temperature and applied strain rate in air

The typical COF vs. time curves at different strain rates and temperatures were plotted in **Figure 4.1a and 4.1b**. **Figure 4.2a** shows COF variations with strain rate at four different temperatures characteristic of the hot-forming process (350 °C, 400 °C, 450 °C and 545 °C). The average COF values are plotted against the instantaneous strain rate measured in the part of the strip inside the hot zone. The reported values are averages of three tests at each temperature and strain rate. The COF values increased with strain rate at each of the four temperatures.

The increase was the highest at 545 °C ranged from 1.94 at $1x10^{-2}s^{-1}$to 2.26 at $4x10^{-2}s^{-1}$. The mean value of COF was 1.73 at T = 350 °C and $d\varepsilon/dt = 1\times 10^{-2}$ s^{-1}. The COF increased to 1.90 at a higher strain rate of 4×10^{-2} s^{-1}. Temperature had a significant effect on COF; increasing the temperature from 350 °C to 545 °C at a strain rate of 4×10^{-2} s^{-1}, the COF value increased by 20 % to 2.26.

In **Figure 4.2b**, the friction data is represented by plotting the average COF values as a function of the test temperature, at four different constant strain rates of 1×10^{-2} s^{-1} 2×10^{-2} s^{-1} 3×10^{-2} s^{-1} and 4×10^{-2} s^{-1}. **Figure 4.2b** indicates that the COF values were higher when the strips were subjected to higher strain rates. At $1x10^{-2}s^{-1}$ the mean value of COF ranged from 1.73 at 350^{o}C to 1.90 at 545^{o}C, at $4x10^{-2}s^{-1}$ the mean value of COF ranged from 1.94 at 350^{o}C to 2.26 at 545^{o}C.

The effects of the strain rate and temperature on COF are shown in the form of a map on temperature vs. strain rate axes, **Figure 4.3**. This map visualizes the combined effect of temperature and strain rate on the COF of AA6061 alloy. From this map, under a certain temperature the mean value of the COF increased with increasing strain rate from 1×10^{-2} s^{-1} to 4×10^{-2} s^{-1}, in addition, at a certain stain rate, the mean value of the COF increased with increasing temperature from 350^{o}C to 545^{o}C.

4.3 Surface deformation and damage at high temperature in air

4.3.1 Pre-existing surface oxide

The surface morphology of AA6061 in the unpolished and undeformed condition is shown in **Figure 4.4**. A compacted oxide layer covered the surface with a morphology typical of rolled aluminum surfaces. The surface damage is due to the cold rolling process and the continuous lines extending parallel to the rolling direction and the formation of surface cracks normal to the rolling direction can be observed. The surfaces were also investigated using white light non-contact optical surface profilometer. **Figure 4.5** shows the 3-D profile of the unpolished and undeformed strip. During the friction tests the P20 pin came in contact with a surface which has undergone simultaneous tensile deformation. Surface morphologies of strips deformed at 545^{o}C and 350^{o}C that have not yet contacted the P20 pin are discussed in **Sections 4.3.2 and 4.3.3**.

4.3.2. Surface morphology after deformation at 545 °C

The typical surface morphology of an AA6061 alloy strip deformed at 545^{o}C and 0.04 s^{-1} is shown in **Figure 4.6**. Due to the sliding of the grains relative to each other, steps formed at the grain boundaries. The tribolayer that covered the top surface of grain

boundaries experienced damage with cracks forming at certain locations. At the same time, formation of thin and fibrous structures was visible at locations just above the top surface of the grain boundaries. The location of the oxide fibres coincided with the grain boundaries of the bulk alloy that exhibited sliding. This phenomenon is akin to microfibers, which were observed on the fracture surface of aluminum [70, 71], proposing local superplasticity in the oxide layer. This kind of phenomenon was also observed by Das [26, 62] and Gali et al.[31] in Al-Mg (AA5083) alloy. The surfaces were also investigated using WYKO NT1100 optical surface profilometer and **Figure 4.7** shows the 3-D profile of the unpolished strip deformed at 545ºC and 0.04 s^{-1}. The surface became rougher and the rolling lines became discontinuous by the sliding motion occurred between the grains when compared with the as-received condition shown in **Figure 4.5.**

Figure 4.8 is a higher magnification view of the deformed surface, and obviously shows how GBS between grain A and B (as labelled in **Figure 4.8**) led to the formation of a prominent grain step. 2.8 ± 0.39 μm long and with a diameter of 146 ± 28nm fibres formed from the oxide is shown in **Figure 4.8** to coincide with sections of oxide lying at the boundary where steps were formed by GBS. Gali et al.[31] reported the oxide ligaments formed on AA5083 alloy at 545ºC and 0.04s^{-1} have a length of 3.04 ± 0.59 μm and with a diameter of 85 ± 39nm. Very few fibres fractured, however a majority of the fibres underwent large amounts of deformation without exhibiting fracture due to the mechanism of micro-superplastic behaviour [70, 72, 73].

4.3.3. Effect of strain rate on surface oxide

When tests were performed at low strain rates at T = 545ºC, the oxide layer remained ductile, with few cracks, as shown in **Figure 4.9.** Very few fibres were also

formed. The length of these fibres was very short and no stretched oxide fibres can be observed when it was compared with the test carried out at higher strain rate shown in **Figure 4.8.** The number of the oxide fibres and their length were a function of the temperature and strain rate and will be indicated in detail in **Section 4.3.5.**

4.3.4. Surface morphology after deformation at 350 °C

A less faceted appearance was observed on the surface that was covered with a pre-existing oxide layer after deformation at 350^{o}C and 0.04 s^{-1}. The extent of the out-of-plane displacement of the near surface grains, seen underneath the oxide layer, was also smaller (**Figure 4.10**) when compared with strips deformed at higher temperatures (**Figure 4.8**). **Figure 4.10** shows that at 350^{o}C the oxide layer fractured more frequently. The resulting cracks were formed normal to the direction of the applied strain, were longer and wider. The oxide fibres did not totally disappear, but were fewer in number.

In summary, clear differences were observed between the surface morphology of strips deformed at 350^{o}C and 545^{o}C. The surface oxide deformed at 350^{o}C exhibited less ductility, with damage proceeding mainly as a result of crack formation, while the oxide exhibited high plasticity and local oxide superplasticity was obvious in the form of fibre formation when the strips were deformed at 545^{o}C. In fact the high length-to-diameter ratios (19 for AA6061) of fibres indicated that superplastic deformation occurred during the formation of these fibres.

4.3.5 Quantification of oxide cracks and oxide ligaments

Statistical analyses were performed to quantify the average length of the fibres as well as the average width of the cracks that appeared on stretched oxide surfaces. The area fraction of oxide surface covered by fibres at 545^{o}C and 0.04 s^{-1} was determined, which

was 17%. An increase in temperature at high strain rate promoted the formation of the oxide fibres and simultaneously hindered the formation of cracks on the surface. The average oxide fibre length and surface crack width are plotted against the test temperature in **Figure 4.11** at a constant strain rate of 4×10^{-2} s^{-1}. The length of the oxide ligaments increased from 0.7 ± 0.05 μm at 350 °C to 2.8 ± 0.39 μm at 545 °C. The average width of the brittle oxide cracks decreased from 3.2 ± 0.21 μm at 350 °C to 1.0 ± 0.37 μm at 545 °C.

4.4 Wear track observation on the strips deformed in air

Surface damage to the AA6061 alloy induced by sliding contact of the steel pin was estimated from measurements of the sliding track width on the tribolayer covered samples for each test run at temperatures 350 °C, 450 °C and 545 °C. **Figure 4.12** and **4.13** display the microstructure of the wear tracks on unpolished AA6061strips obtained in air, **Figure 4.14** shows the variation of sliding track width with temperature. Sliding track width was observed to increase with temperature for as-received surface conditions. The widest sliding track occurred at 545 °C and the narrowest at 350 °C. Sliding track damage appeared to correlate with the temperature increase as AA6061 displayed increasing damage in the form of overlaps, grooves and compacted oxide debris due to plastic deformation.

4.5 Adhesion and material transfer to P20 steel in air

The material was transferred to P20 steel surface (counterface) when slid against AA6061 alloy surface. The typical transferred material generated under the experimental condition of $\dot{\varepsilon} = 4 \times 10^{-2}$ s^{-1} and T = 350 °C, 450 °C, 545 °C were shown in **Figure 4.15**. Material transfer was not uniformly distributed with build-up observed at the sides of the

sliding track and minute quantities of material transfer spread across wide areas of the pin surface. Also, the area of the transferred material to counterface was plotted in **Figure 4.16**. The area of material transferred to the counterface increased with increasing temperature.

4.6. Deformation mechanisms of the material at high temperatures

4.6.1. Mechanisms identified based on stress-strain rate data

The change in tensile load applied to the AA6061 strip with time was determined for different strain rates at a given temperature. Typical data is given in **Figures 4.17 a, b and c** for tests conducted at 350ºC, 450 °C and 545 °C, respectively. The flow stress of the AA6061 was calculated using the cross-sectional area of the sample when it passed through the hot zone (shown in **Figure 3.8**) within a time interval, *dt* =10s (from 70s to 80s). Ture strain rate was determined from the strain differences within a time interval of *dt* = 2s. The flow stress values are plotted in temperature and strain rate space in **Figure 4.17 d**. The relationship between the strain rate and applied modulus-compensated flow stress of AA6061 was determined using the general creep equation (**Equation 4.1**) from the data plotted in **Figure 4.18**.

$$\dot{\varepsilon} = A\left(\frac{\sigma}{E}\right)^{n} \exp\left(-\frac{Q}{RT}\right) \quad (4.1)$$

$$\ln \dot{\varepsilon} = \ln A + n \ln\left(\frac{\sigma}{E}\right) - \frac{Q}{RT} \quad (4.2)$$

Where *A* is a material constant, σ is the flow stress (the instantaneous value of stress required to continue plastically deforming the material), *n* is the stress exponent, *E* is the temperature compensated Young's modulus ($E = E_{RT}\,[1-5.3\times10^{-4}(T-300)]$), *Q* is the

activation energy for deformation, and *R* is the universal gas constant. The stress exponent, *n*, was obtained from the slope of a log $\dot{\varepsilon}$ vs. logσ (**Equation 4.2**) plot in **Figure 4.18**. The values of n, thus calculated are found to be in range of 1 to 3. As described earlier, a stress exponent of $n = 2$ is indicative of creep by grain boundary sliding (GBS) [37]. The value of n =2 was calculated for the temperature range between 440 ^{o}C to 545^{o}C and strain rate range of 2×10^{-2} s^{-1} to 4×10^{-2} s^{-1}. Thus, GBS was the operative mechanism in this temperature and strain range.

An effective way of illustrating the creep mechanisms for AA6061 was obtained by plotting a stress exponent contour map in temperature vs. strain rate space (**Figure 4.19**). At low temperature (< 440 °C) and high strain rate (4×10^{-2} s^{-1}), dislocation creep regime was determined based on the stress exponent value n = 3, and the flow stress reported by Requena, et al. [45, 46]. They reported that a stress exponent of $n \approx 3$ is found from 25 to 50 MPa concluding dominating dislocation creep. The flow stress calculated from experimental data (see **Figure 4.17**) gave a flow stress range from 30 to 60MPa in the n=3 regime which shown in **Figure 4.19.**

At low strain rate ($\leq 1.5 \times 10^{-2}$ s^{-1}) for all temperatures a stress exponent value of n = 1 was found and indicated that the diffusional flow was the dominant creep mechanism for these considerations [45]. A stress exponent of $n = 2$ was calculated for the temperature range of 440 °C – 545 °C and strain rate range of 2×10^{-2} s^{-1} – 4×10^{-2} s^{-1} . This was identified as GBS regime.

In **Section 4.2**, COF was observed to change with temperature and strain rate, actually, surface roughness or surface oxide damage mechanism may result in the variation of the COF. In this section, different deformation mechanisms were observed in different

temperature and strain rate regimes. It is necessary to build a relation between the deformation mechanisms and the surface characteristics.

4.6.2 Variation of the surface roughness

This section presents results of the measurement of surface roughness changes caused by the alloy's bulk deformation at elevated temperatures. The surface morphology of the as-received samples and the samples tested at high temperatures were studied with a white light interferometer. Four different locations on two sets of samples were considered for measuring *Ra*, for each location five measurements were performed, and the resulting values are given in **Table 4.1.** The lowest *Ra* of 0.61 μm was found for deformation at 350 °C and a strain rate of 1×10^{-3} s^{-1}. The R_a increased to 1.28 μm at a higher temperature of 545 °C and a strain rate of 4×10^{-2} s^{-1}. The variations of surface roughness with strain rate at four temperatures are plotted in **Figure 4.20** (a-d).Accordingly, it becomes clear that the temperature and strain rate conditions resulting in high *Ra* values also contributed to high COF values.

Table 4-1 Surface roughness at different temperatures and strain rates.

Strain rate, s^{-1}	Roughness, μm			
	350 °C	400 °C	450 °C	545 °C
1×10^{-2} s^{-1}	0.61 ± 0.12	0.63 ± 0.1	0.64 ± 0.09	0.74 ± 0.08
2×10^{-2} s^{-1}	0.72 ± 0.09	0.74 ± 0.13	0.74 ± 0.14	0.73 ± 0.1
3×10^{-2} s^{-1}	0.85 ± 0.11	0.85 ± 0.12	0.85 ± 0.09	0.91 ± 0.11
4×10^{-2} s^{-1}	0.96 ± 0.09	0.9 ± 0.08	0.97 ± 0.1	1.28 ± 0.15

An effective way of combining the observed creep mechanisms for AA6061 with the variation of surface roughness was to construct a surface roughness map in temperature

and strain rate axes (**Figure 4.21**). This constant Ra contour map illustrated how the operating plastic deformation mechanisms would affect the surface roughness. Higher surface roughness occurred on the GBS regime at the temperature range of 440 °C – 545 °C and strain rate range of 2×10^{-2} s^{-1} – 4×10^{-2} s^{-1}. When the alloy's creep deformation mechanism was dislocation creep, the surface roughness was exhibited relatively smooth.

A considerable increase in roughness was observed with the increase in temperature and strain rate. The variation in roughness was affected by the evolution of the surface characteristics, which depended on the alloy's deformation behaviour.

4.7 Variation of coefficient of friction (COF) with temperature and applied strain rate in argon.

The friction experiments were performed in argon for polished and unpolished strips at temperatures between 350 °C and 545 °C at a strain rate of $4x10^{-2}$ s^{-1}. The purpose of these experiments was to study the effect of atmosphere on the friction behaviour.

Typical COF vs. sliding time plots in argon for unpolished strips (with existing tribolayers), obtained at three different temperatures (350 °C, 450 °C and 545 °C) and at constant strain rate of 4×10^{-2} s^{-1}, are shown in **Figure 4.22a.** In order to make a comparison, the typical COF vs. sliding time plots in air that were obtained under the same loading conditions, see **Figure 4.22b.** COF measured in argon at a strain rate of 4×10^{-2} s^{-1} and temperature of 545 °C resulted in an average COF of 2.35 ± 0.06, which was the highest COF value measured under present experimental conditions. The average COF values in air and argon are plotted against different temperatures in **Figure 4.23**. The reported values are the averages of three tests at each temperature and strain rate. The COF value increased with temperature at the constant strain rate of 4×10^{-2} s^{-1} in air and argon. Under the

experimental conditions shown in **Figure 4.23**, the mean COF value measured in an argon environment at each temperature was higher than that in air.

In order to study the effect of the tribolayer and the atmosphere on the friction behaviour, the surface of the strips were mechanically polished to a 1 μm diamond finish to remove the tribolayer. Typical COF vs. sliding time plots of samples without tribolayer tested at three different temperatures (350 °C, 450 °C and 545 °C) and at constant strain rate of 4×10^{-2} s^{-1}, are shown in **Figure 4.24a.** For a comparison, the typical COF vs. sliding time plots in air were obtained under the same loading conditions see **Figure 4.24b.** In an argon atmosphere and a strain rate of 4×10^{-2} s^{-1} and temperature of 545 °C the highest average COF of 2.67 ± 0.01 was measured. The average COF values in air and argon are plotted against temperature in **Figure 4.25**. The reported values are the averages of three tests at each temperature and strain rate. The COF value increased with temperature at the constant strain rate of 4×10^{-2} s^{-1} in air and argon. The mean COF value measured in argon environment at each temperature was higher than that in air. The interpretation of higher COF values obtained in argon in comparison to those obtain in air will be discussed in **Section 5.4.**

4.8 Surface deformation and damage of polished strips at high temperature in an argon atmosphere

4.8.1. Surface morphology after deformation at 545 °C in an argon atmosphere

The typical surface morphology of an AA6061 alloy strip deformed in an argon atmosphere at 545^{o}C and 0.04 s^{-1} is shown in **Figure 4.26**. Due to the sliding of the grains relative to each other the steps were formed at the grain boundaries. Unlike the test performed in air, formation of the fibrous structures cannot be observed at the grain

boundaries subjected to sliding. **Figure 4.27** is a higher magnification view of the deformed surface, and obviously shows how GBS between grain A and C (as labelled in **Figure 4.27**) led to a formation of a prominent grain boundary step.

4.8.2. Surface morphology after deformation at 350 °C in argon

A less faceted appearance of the surface was observed after deformation at 350^{o}C and 0.04 s^{-1} (**Figure 4.28**) when compared to strips deformed at 545^{o}C (**Figure 4.26**). **Figure 4.29** shows that at 350^{o}C the tribolayer fractured and the resulting cracks, forming normal to the direction of the applied strain, and there was no evidence for the oxide fibres.

In summary, differences were observed between the surface morphology deformed in argon at 350^{o}C and 545^{o}C.The surface oxide deformed in argon at 350^{o}C exhibited less ductility, with damage proceeding mainly as the result of crack formation compared to the surface oxide deformed at 545^{o}C. The surface microstructure and morphology of the deformed work piece in air and argon will be compared in **Section 5.3**.

4.9 Wear track and adhesion comparison in argon and air.

Surface damage to the AA6061 alloy induced on contact with the steel pin in argon environment was estimated from measurements of the sliding track width on the samples covered with tribolayers for each test run at temperatures 350 °C, 450 °C and 545 °C. **Figure 4.30** displays the optical microstructures of the wear tracks formed on unpolished AA6061strips obtained in argon, and **Figure 4.31** shows the variation of sliding track width in argon and air. Sliding track width was observed to increase with temperature. The widest sliding track was formed at 545 °C in air and the narrowest at 350 °C also in air. The wear track width also increases in argon atmosphere with temperature. However, at 450^{o}C and 545^{o}C the wear track width is smaller than that in air.

The material was transferred to P20 steel surface (counterface) when slid against AA6061 alloy surface in both air and argon. The typical transferred material generated under the experimental condition of $\dot{\varepsilon} = 4\times 10^{-2}\ s^{-1}$ and T = 350 °C, 450 °C, 545 °C are shown in **Figure 4.32**. The morphology of the material transferred to the P20 pin from the strips tested in air was discontinuously distributed over a wide area. The amount of material transfer in argon is more than that in air. The maximum height and the area of the transferred material to the counterface were plotted in **Figure 4.33a** and **4.33b**. In general, the maximum height decreased at 545^{o}C in both air and argon. However, the maximum height of material transferred to the counterface in argon is higher than that in air, and the area of the transferred material to the counterface in argon atmosphere is larger than that in air.

4.10 Junction strength tests

4.10.1 Measurement of junction strength of AA6061 alloys in comparison with others against steel in Air.

The typical trends of the tangential forces as a function of sliding time are shown for each alloy in **Fig.4.34 (a)**, where the maximum tangential force corresponds to the force required to break adhesive junctions (i.e. the junction strength). For AA1100, the time required to break the junction was larger, while the maximum junction strength of AZ91 was reached within a shorter time. After reaching the highest tangential strength, sliding was continued and all samples showed variable fluctuations in the tangential force possibly due to formation of new junctions. The tangential force required to break the new junctions was less compared to that required to break the first junction. For AZ91, the force curve showed less fluctuations. It is possible that the surface magnesium oxide formation on AZ91 played a role in decreasing the force required to break the junctions from the steel

counterface. While the curve for AA6061 showed more fluctuations possibly due to less oxide formation (due to less Mg content than AZ91 alloy) during the sliding. The change in the junction strength for each alloy is summarized in **Fig.4.34 (b)**. It was observed that the junction strength decreased with the increase in Mg content in the Al-Mg alloys against steel counterface when tested in air.

4.10.2 Analyses of the material transfer to steel from different alloys in air.

Figure.4.35 shows the optical microstructures of the contact surfaces of M2 steel discs used as counterfaces while sliding against AA1100 [Fig.4.35 (a)], AA6061 [Fig.4.35 (b)], AA5083 [Fig.4.35 (c)] and AZ91 [Fig.4.35 (d)]. The contact surface after sliding against AA1100 [Fig.4.35 (a)] exhibited a region of initial contact and a region representing junction growth [74] when the tangential force was applied. The area of the material transferred to the counterface, in general, decreased with the increase in Mg content. **Figure.4.36** shows that the height of the material transferred to the counterface disk increased with decreasing Mg content. The maximum height of the material transferred to the counterface and the area of the transferred material to counterface are summarized in **Figure.4.37a and 4.37b**. SEM images and EDS elemental maps taken from the contact surfaces of the steel discs after each test are shown in **Figure.4.38.** It was observed that the contact areas for alloys containing lower amount of Mg contained less oxygen. Therefore oxide formation was not observed for these alloys. Considering the Mg and O-maps of AA5083 and AZ91, it was suggested that a large quantity of oxides rich in Mg were formed for these alloys.

4.10.3 Microstructure of Al-Mg pins after sliding tests against steel in air.

2-dimensional surface profile measurements, presented in **Figure.4.39**, showed that the height of the pin-tip decreased with decrease in Mg content in the alloys. The oxide enriched layer formed in Mg rich alloys reduced adhesive material transfer. A reasonable evidence can be revealed from the SEM images and EDS elemental maps taken from the contact surfaces of the alloy after each test are shown in **Figure.4.40.** Oxygen is detected on all alloys' surface. For AZ91, the main oxide covering on the deformed surface is MgO, for AA1100, the oxides occur in a form of Al_xO_y instead of MgO. For AA5083 and AA6061 alloys, the occurrence of MgO and Al_xO_y can be evidenced from the Mg, Al, and O map shown in **Figure.4.40**. In general, when the junction strength tests were performed in air, oxides were formed at the deformed pin surfaces of all alloys.

4.10.4 Comparison of junction strength of AA6061 in Air and Argon

In order to understand the localized junction formation due to material adhesion and transfer during the sliding experiments at different atmospheres, the adhesive force measurements tests were performed at 420^{o}C in air and argon to study the role of the atmosphere on the formation of surface oxides that control the friction and material transfer occurring during initial sliding contact between the samples and the counterface. The typical trends of the tangential forces as a function of sliding time are shown for each alloy in **Fig.4.41 (a)**, where the maximum tangential force corresponds to the force required to break adhesive junctions (i.e. the junction strength). In argon, the time required to break the junction (38s) was more than that in air (34s).

After overcoming the first junction, sliding was continued and samples in both atmospheres showed fluctuations in the tangential force possibly due to the formation of

new junctions. In argon, after overcoming the first junction the curve dropped to a relatively lower position and showed a relatively flat trend. A similar trend was also observed in air. However, the tangential force generated after the first junction broke in argon (average 1.2N) was higher than that in air (average 0.8N). It is possible that the surface oxide formation on AA6061 in air played a role in decreasing the force required to break the junctions from the steel counterface, in addition, in the absence of the surface oxide formation in argon, the tangential (friction) force showed a higher mean value than that in air. The change in the junction strength for different atmospheres is summarized in **Fig.4.41 (b)**.

4.10.5 Comparison of material transfer and surface analyses of AA6061 in Air and Argon.

Figure.4.42 shows the 3-D profilometry images of the adhered material on the steel counterface surfaces tested against AA6061 alloys in (a) air, and (b) argon. The area covered with the transferred material in argon is obviously larger than that in air, and the height of the material transferred to the counterface after sliding tests with AA6061 in air (10.8um), in general, is less than that formed in argon atmosphere (19um). It is possible that the oxide enriched layer formed in air reduced adhesive material transfer.

SEM images of the deformed AA6061 pin in air and argon, presented in **Figure.4.43.** The contact areas after the sliding in air and argon were almost the same, however, in air, a dark layer was observed on the deformed area as labelled in **Figure 4.43**. In argon, no dark layer was observed on the deformed surface and grooves formed along the sliding direction resulting in a rougher surface. The differences appeared on the surface indicated that the atmosphere played a role in this tribological system. It is possible that in the absence of oxygen, no oxide layer formed and resulting in more metal to metal contact

between the alloy and the steel counterface, consequently, induced higher junction strength. While, in air, due to the dark layer formation, resulting in less intimate contact between the alloy and the steel counterface.

A reasonable evidence can be revealed from the EDS elemental maps taken from the contact surfaces of the alloy after each test are shown in **Figure.4.44.** It was observed that the contact areas for alloys deformed in argon contained less (negligible) oxygen than that in air. Therefore oxide formation was not observed for AA6061 in argon atmosphere, and it is consistent with the conjecture stated above.

4.11 Summary of the results

The role of temperature and strain rate on friction behaviour of AA6061 alloy was studied by performing the friction test using hot-forming simulator. An increase in the COF with an increase in the temperature and strain rate was observed in air. Different surface characteristics were observed for the plastically deformed material under different conditions of temperature and strain rates. The surface roughness of the sample increased with the increase in temperature and strain rate. The surface roughness increase in the sample deformed at 545^{o}C and 4×10^{-2} s^{-1} due to the presence of grain boundary steps was confirmed through the metallographic examination on the deformed surface. The COF measured in argon at 4×10^{-2} s^{-1} at each temperature was higher than that measured in air. In summary this chapter shows the relationship between the plastic deformation and surface damage mechanisms, and their relation with the tribological behaviour of AA6061 alloy. Additionally, the localized junction formation behaviour due to material adhesion and transfer during the sliding experiments was investigated in various atmospheres. The junction strength of AA6061 in argon is higher than that measured in air due to the absence

of an Mg oxide layer on the surface of the alloy. This was consistent with the higher COF values obtained in argon.

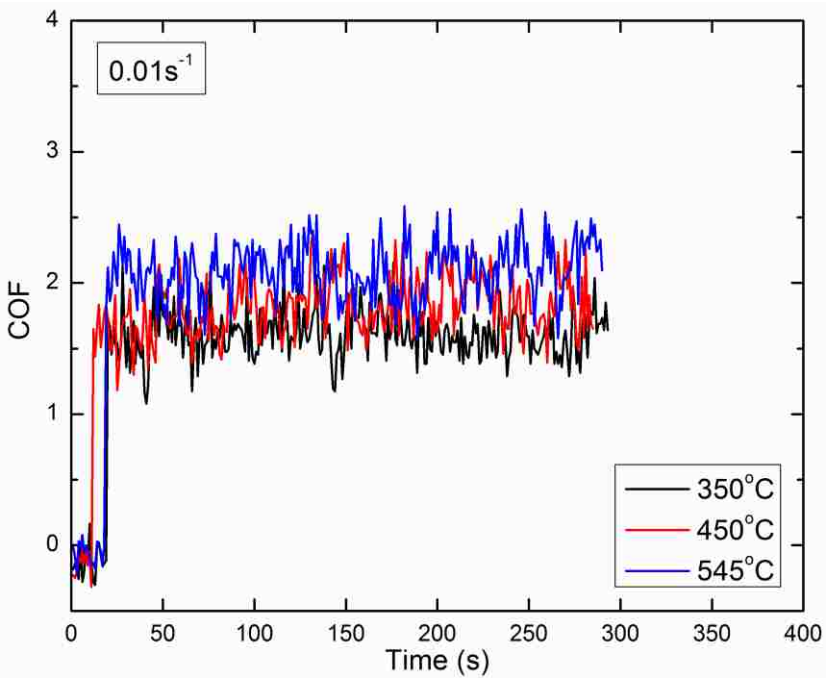

(a)

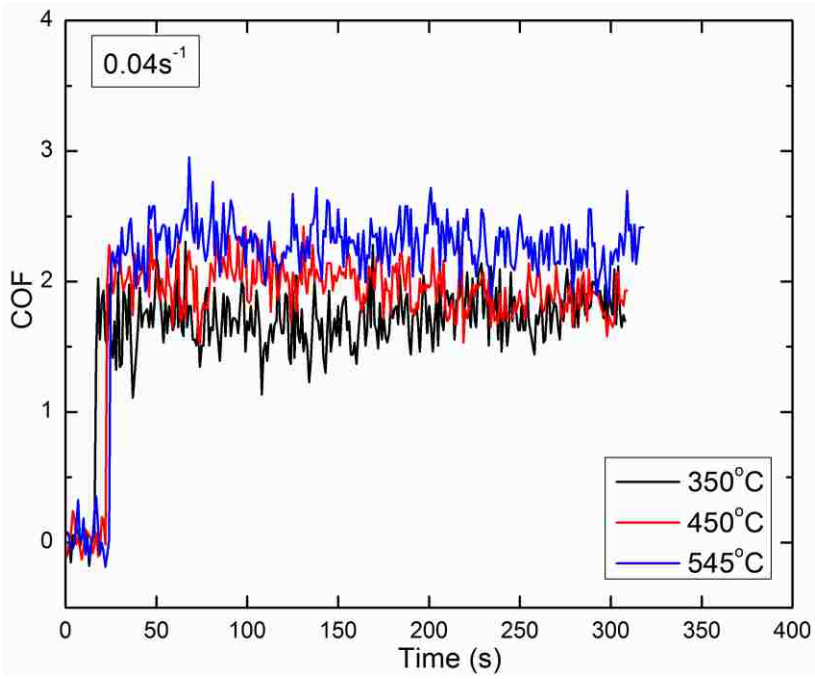

(b)

Figure 4.1 Typical COF vs. time curves at different strain rates: (a) at $0.01s^{-1}$ (b) at $0.04s^{-1}$

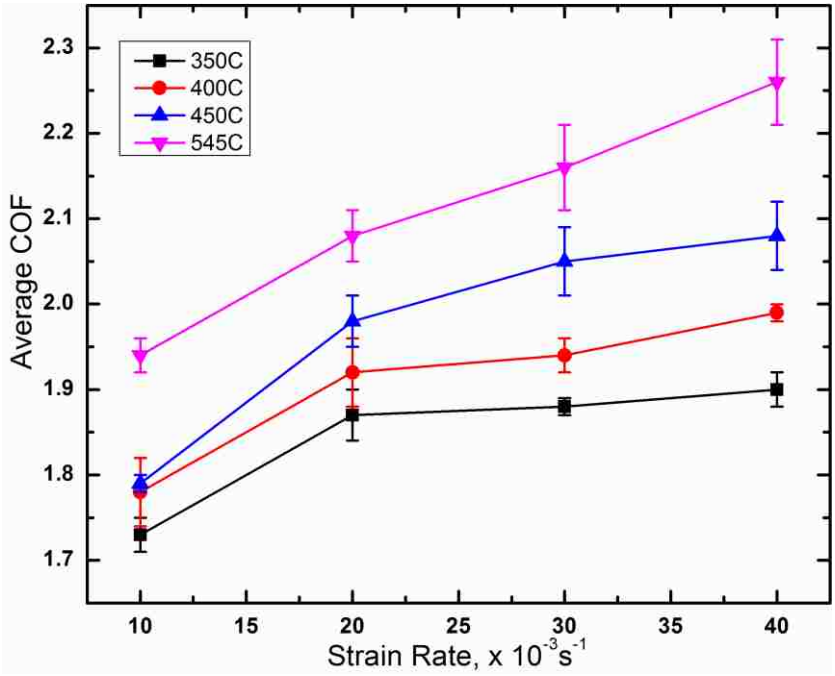

(a)

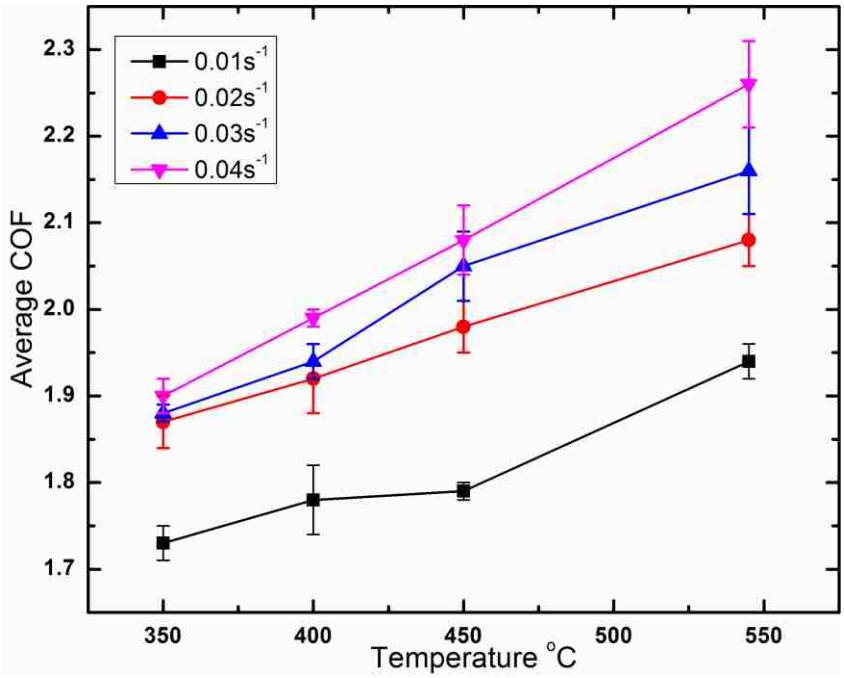

(b)

Figure 4.2 Average COF vs. time plot: (a) at different temperatures (b) at different strain rates. Error bars indicate range of fluctuations in mean COF values measured over 100 s time test period on each strip (following the initial 20 s heating period) at a constant temperature and strain rate.

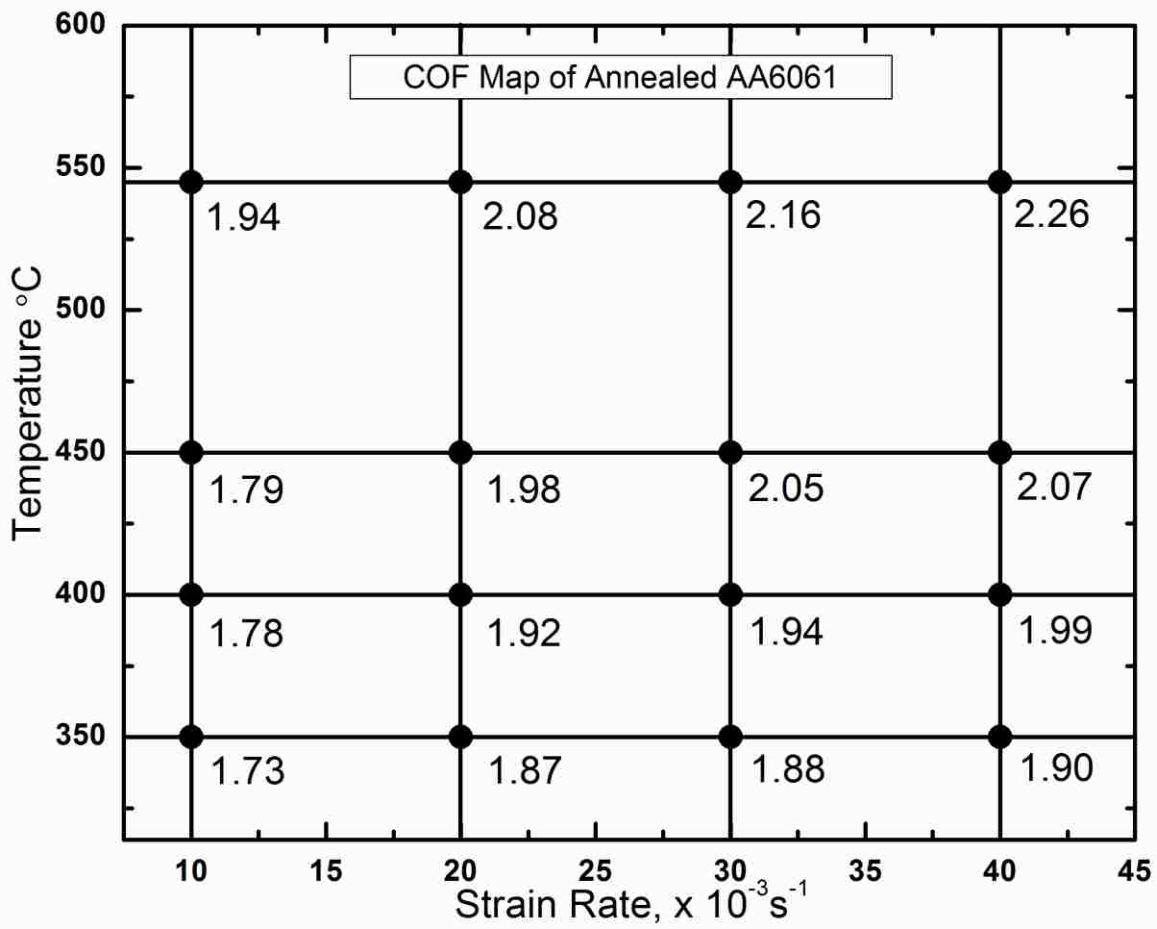

Figure 4.3 Average COF values plotted on temperature vs. strain rate axes in air.

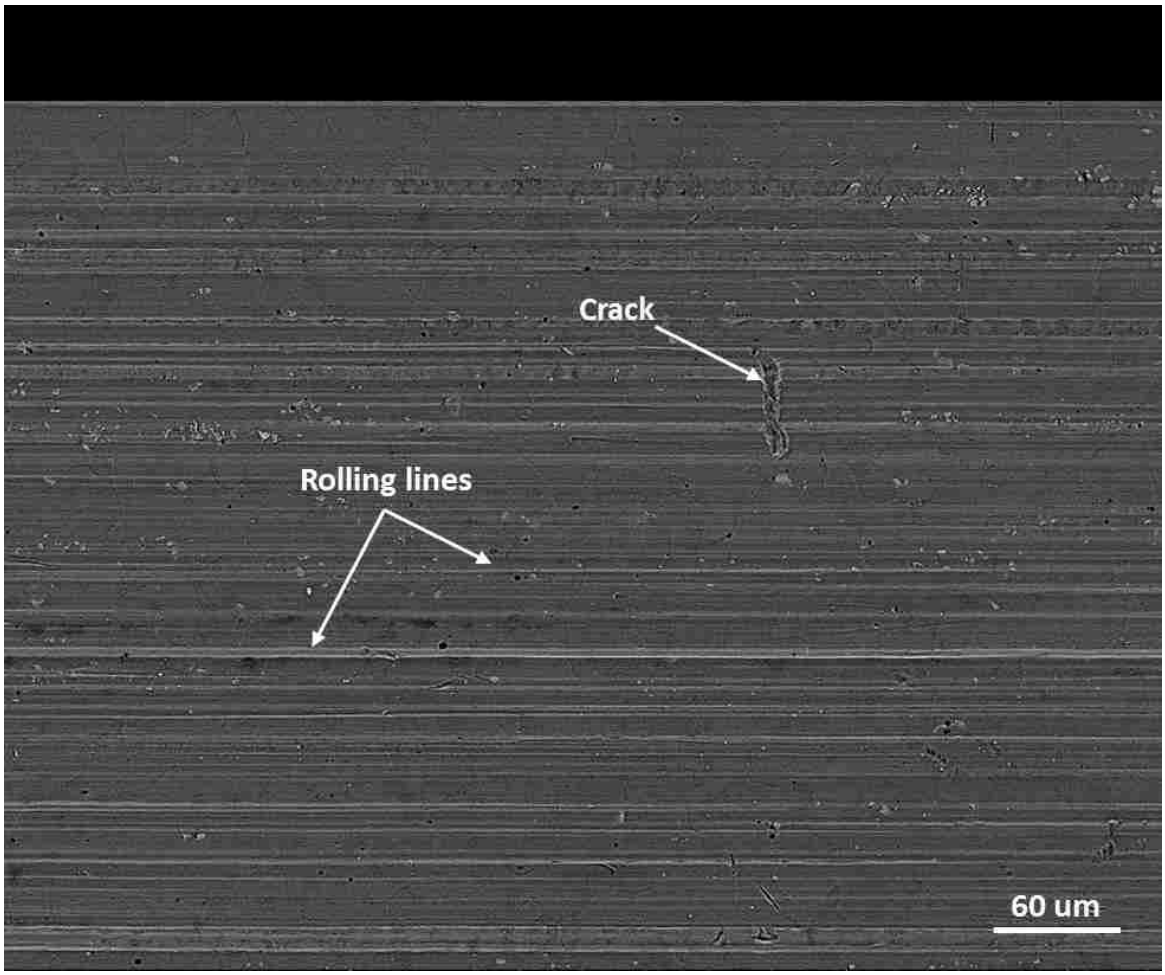

Figure 4.4 Secondary electron image showing the surface morphology of as-received AA6061 strip surface.

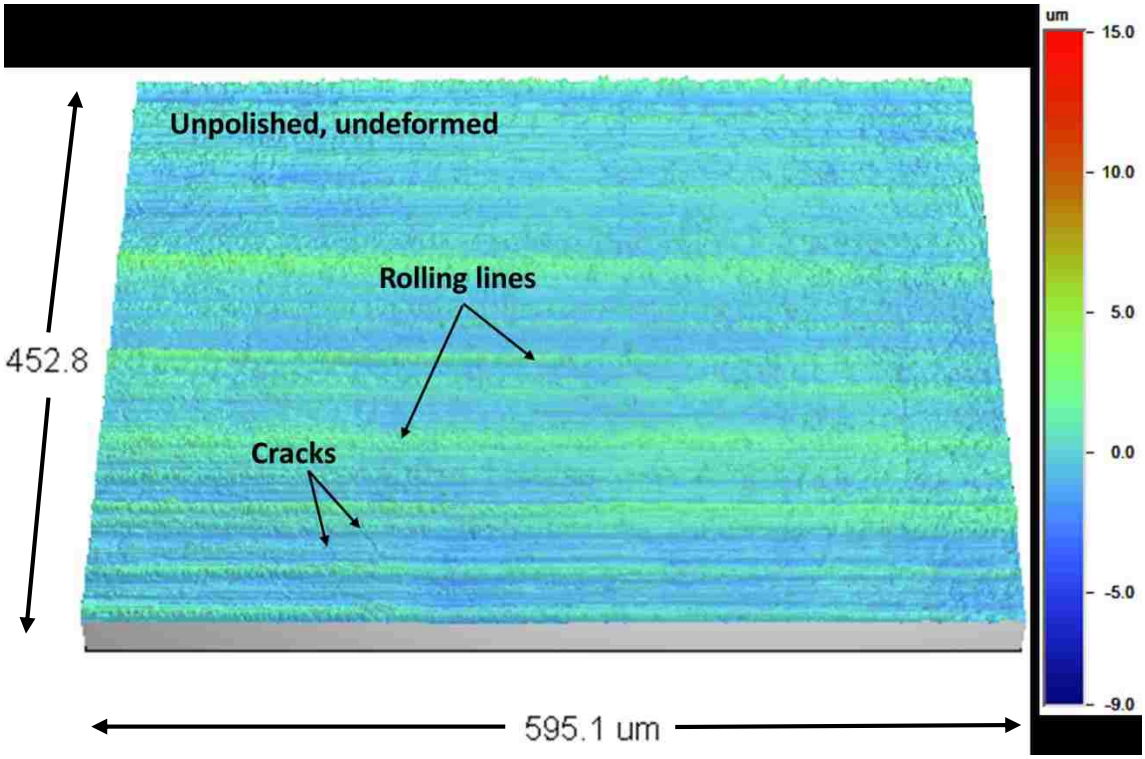

Figure 4.5 Three-dimensional surface profile showing the surface morphology of as-received AA6061 strip surface.

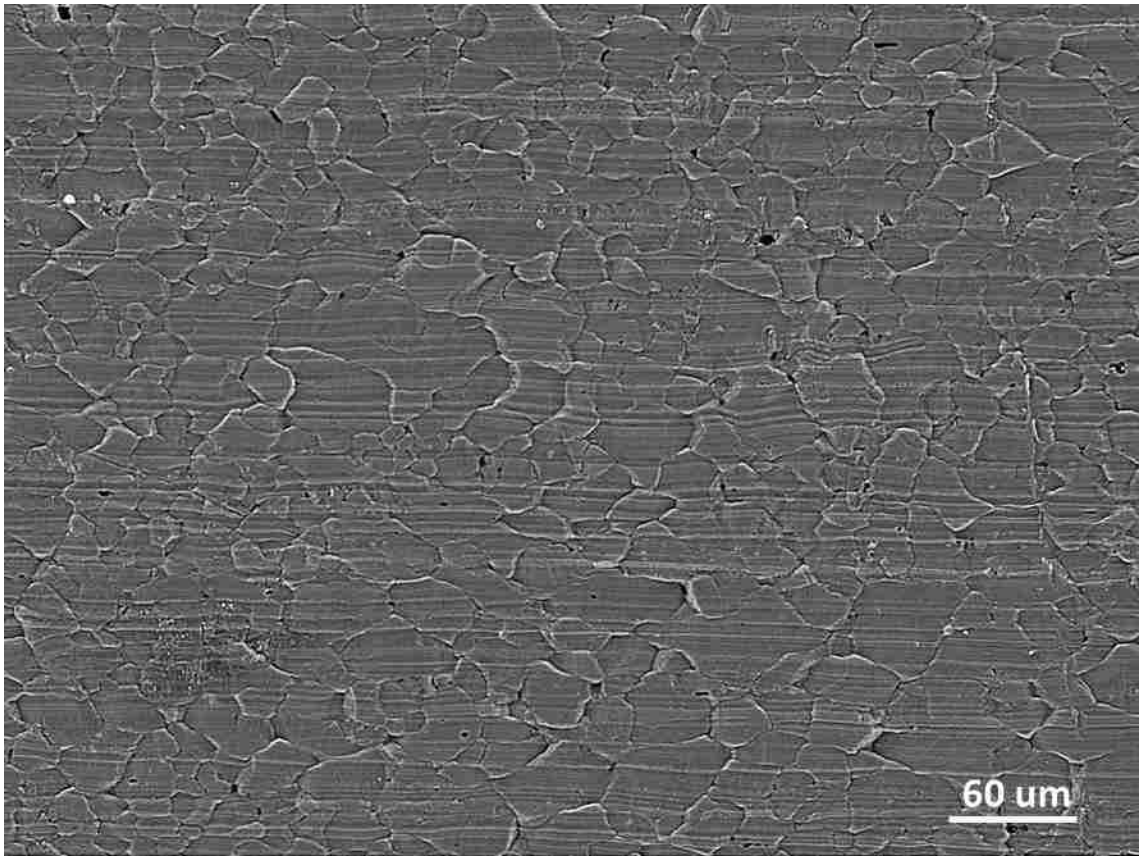

Figure 4.6 Secondary electron image showing the surface morphology of as-received AA6061 strip deformed at elevated temperatures (545 °C and 4×10^{-2} s^{-1}).

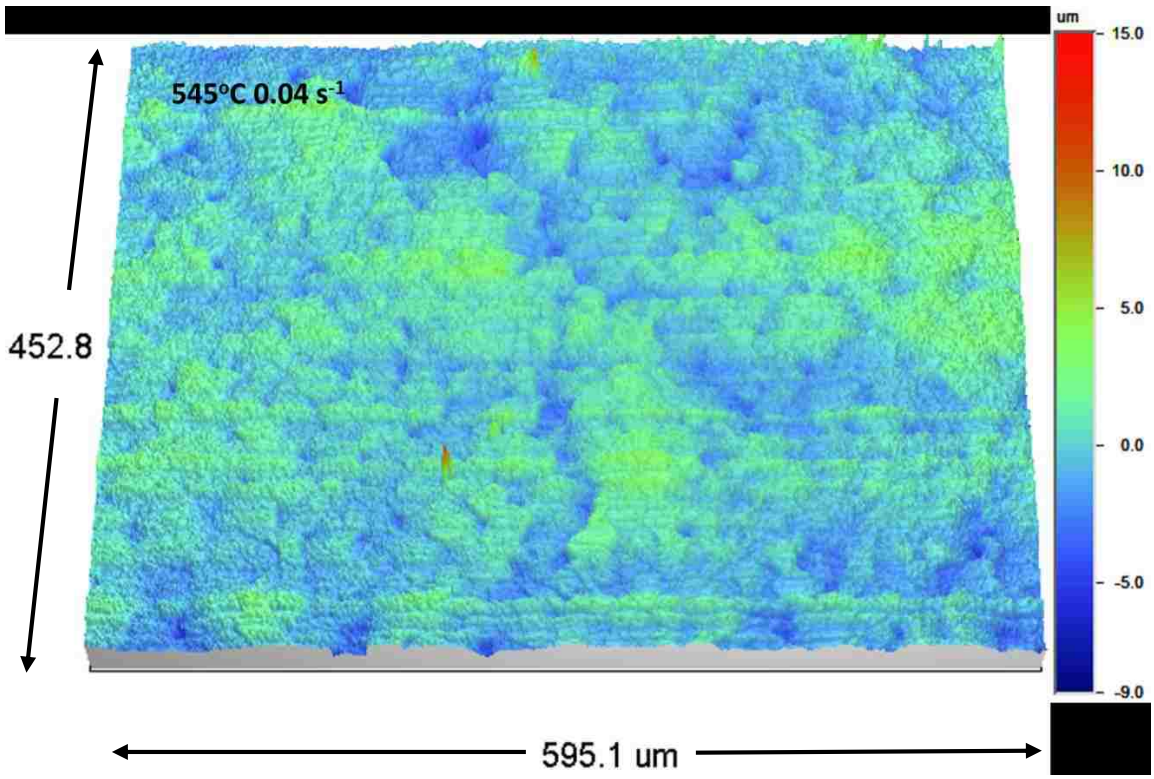

Figure 4.7 Three-dimensional surface profile showing the surface morphology of as-received AA6061 strip deformed at elevated temperatures (545 °C and 4×10^{-2} s^{-1}).

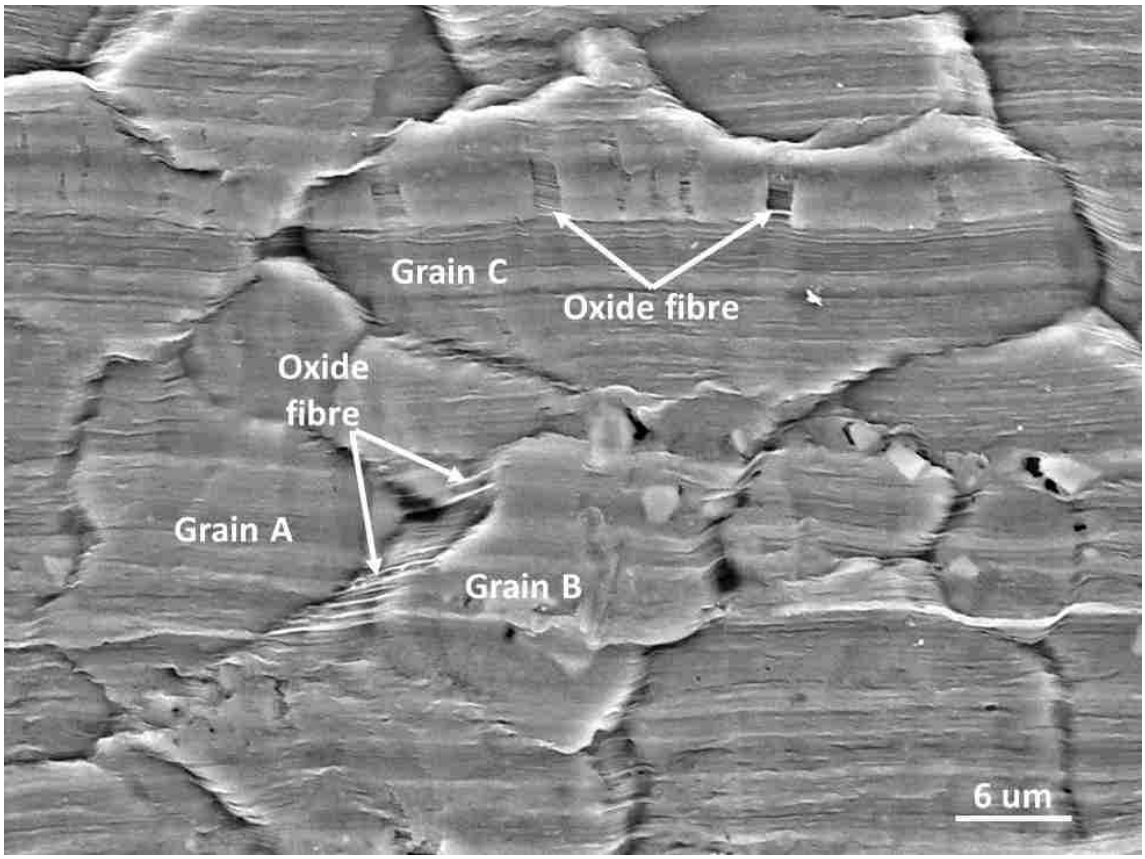

Figure 4.8 A higher magnification view of the sample surface deformed at 545 °C and 4 × 10^{-2} s^{-1}. Surfaces are covered by oxide layers, and GBS beneath oxide layers is evident.

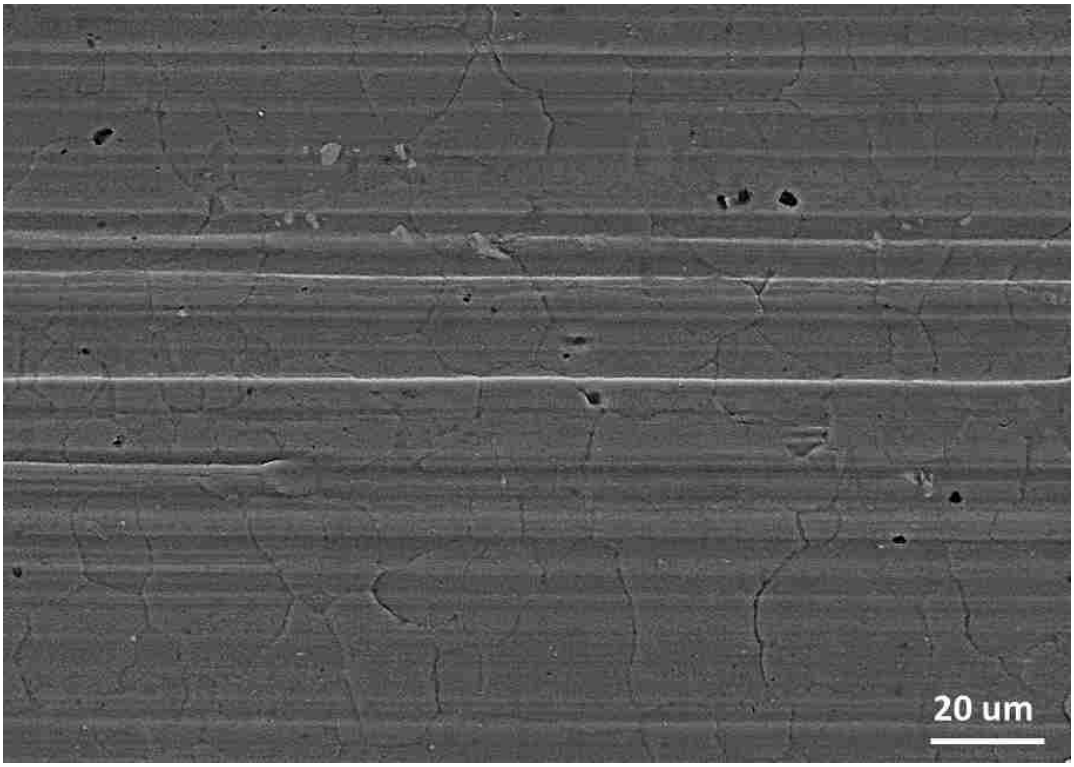

Figure 4.9 SEM micrograph of the deformed surface corresponding to the condition (545 °C and 1×10^{-2} s^{-1}) where a few oxide ligaments were observed at the grain boundaries.

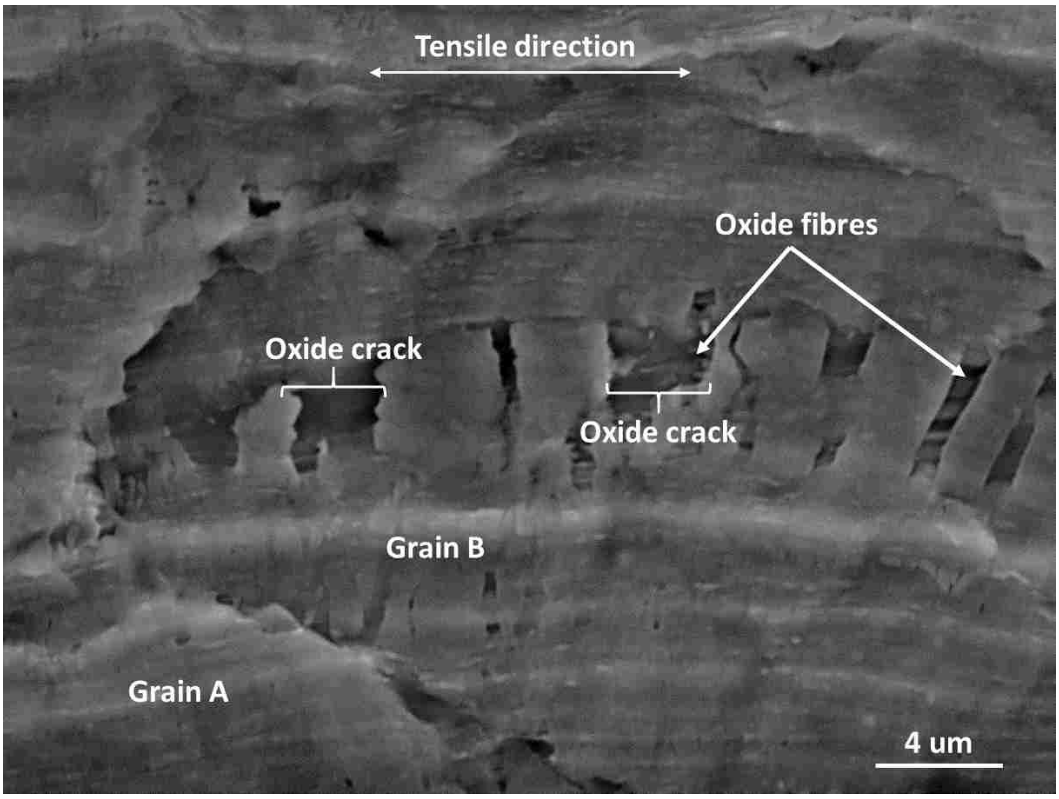

Figure 4.10 SEM micrographs of the sample deformed at 350 °C and 4×10^{-2} s^{-1}. Cracks in surface oxide indicate the brittle nature of the oxide at low temperatures.

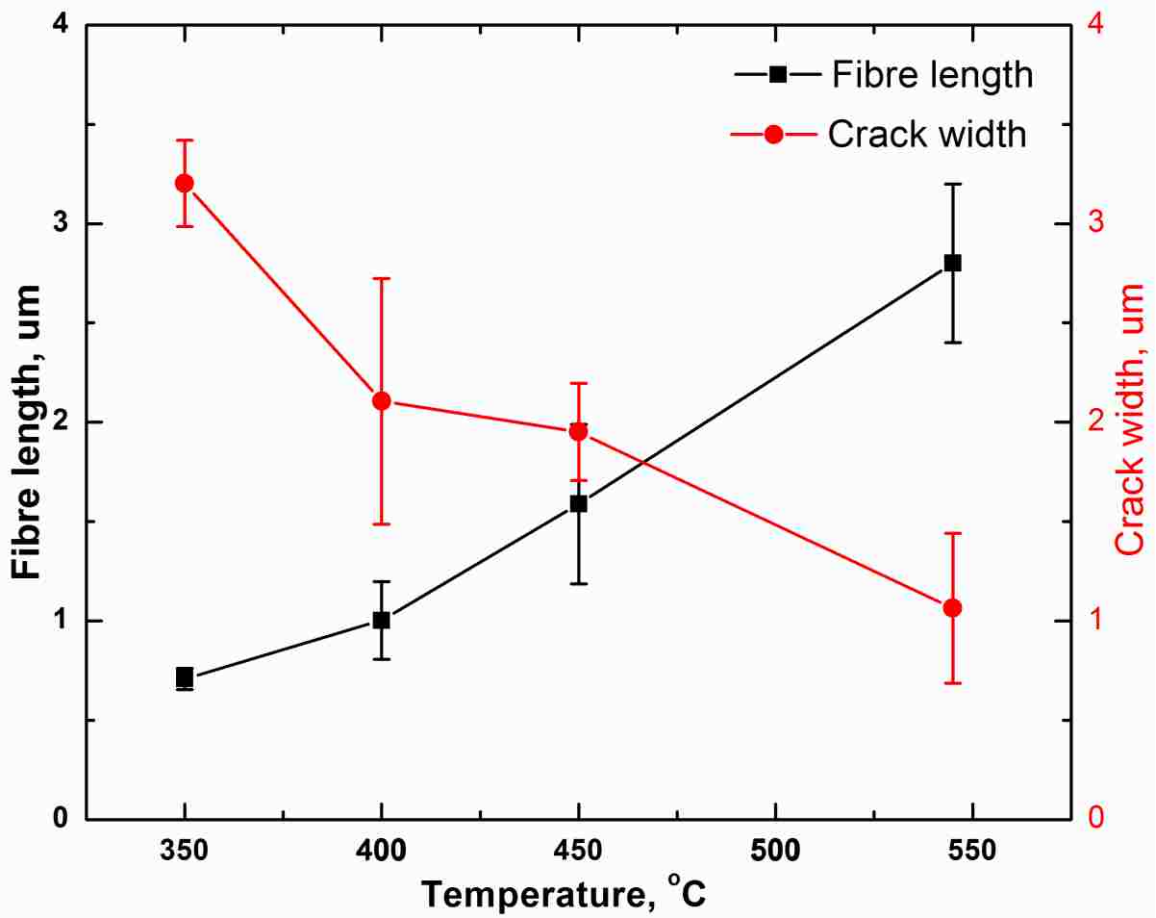

Figure 4.11 Crack width and fibre length vs. temperature plot at $0.04s^{-1}$ shows the length of superplastic fibres increases with temperature. Crack width indicates the width of the brittle cracks that occurred on the grains.

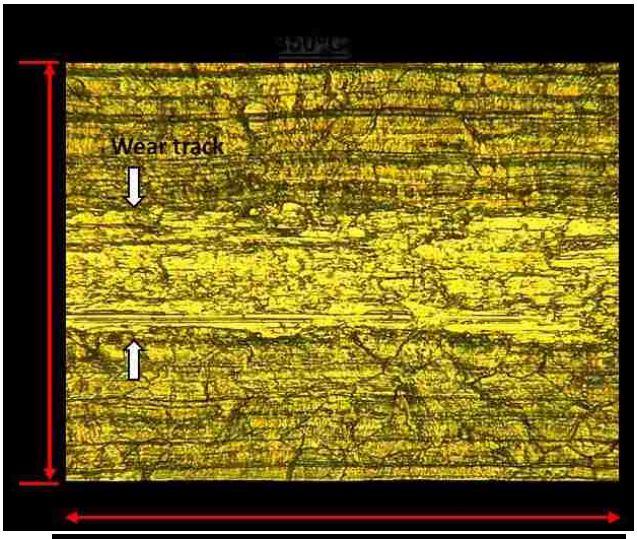

(a)

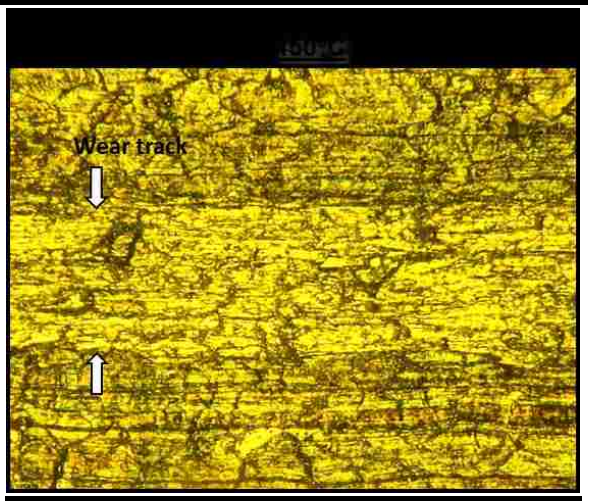

(b)

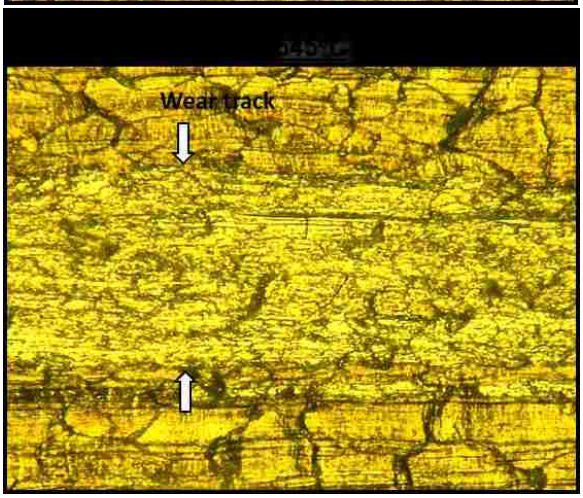

(c)

Figure 4.12 Optical microstructure of the wear tracks on unpolished AA6061strips obtained in air at $0.04s^{-1}$: (a) at 350°C, (b) at 450°C, (c) at 545°C.

(a)

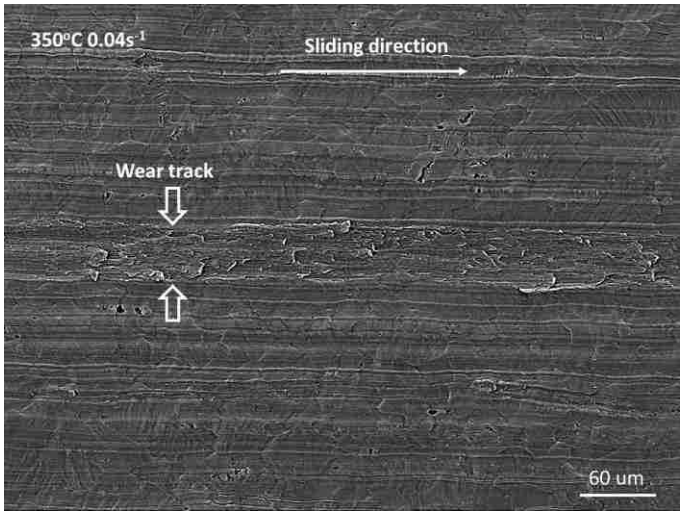

(b)

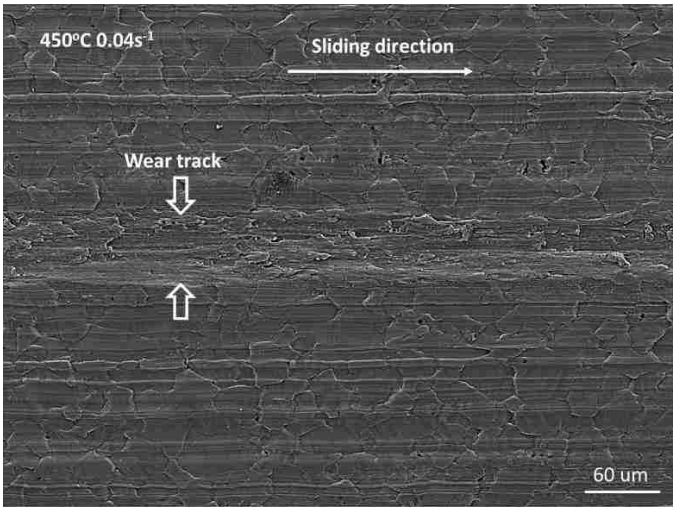

(c)

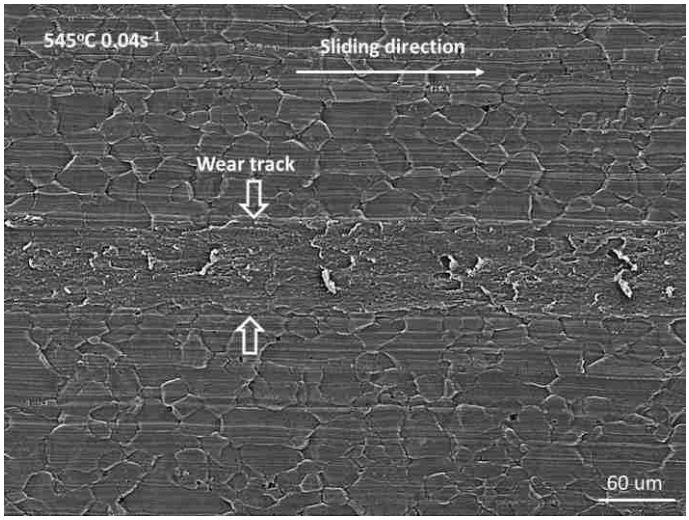

Figure 4.13 SEM images of the wear tracks on unpolished AA6061strips obtained in air at 0.04 s^{-1}: (a) at 350°C, (b) at 450°C, (c) at 545°C

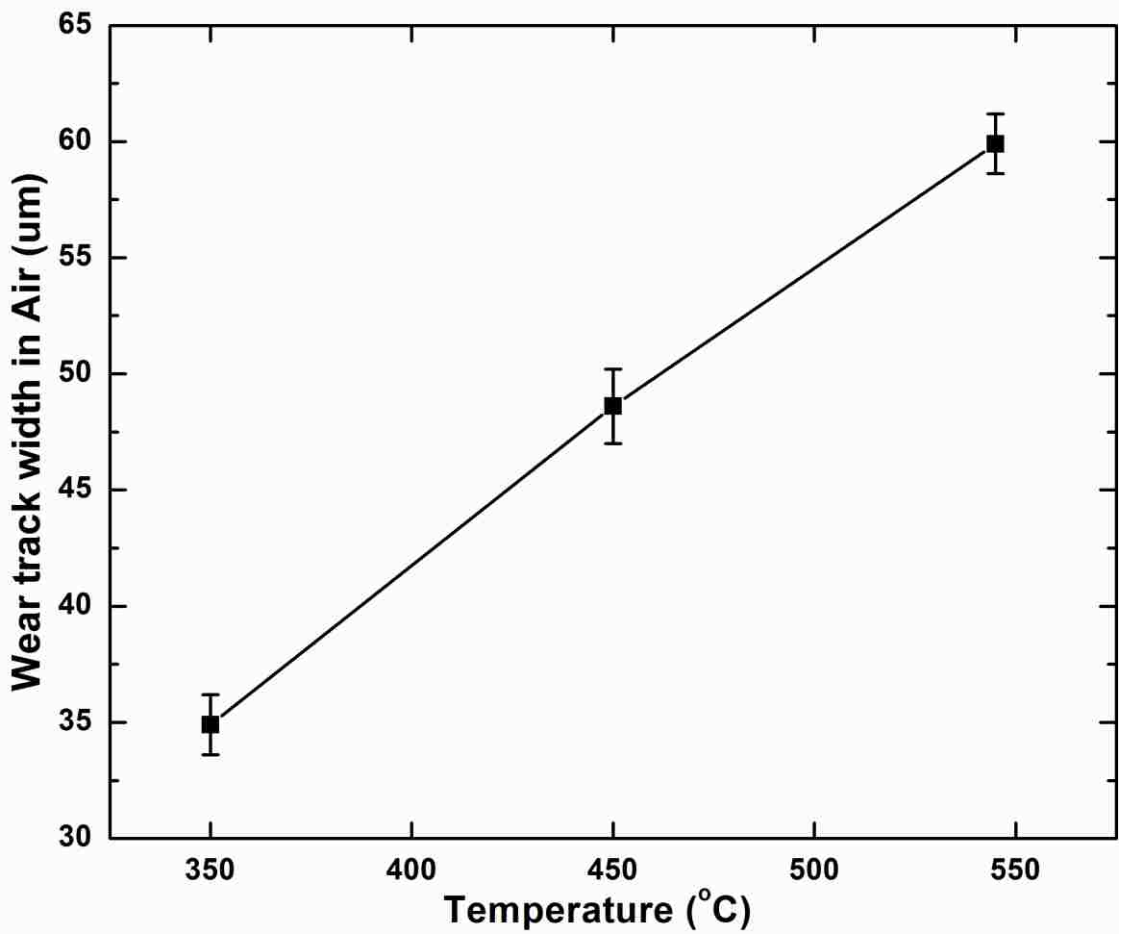

Figure 4.14 Changes in the width of the sliding induced wear track on the AA6061 strip unpolished condition in contact with the P20 steel pin at various temperatures and $0.04s^{-1}$.

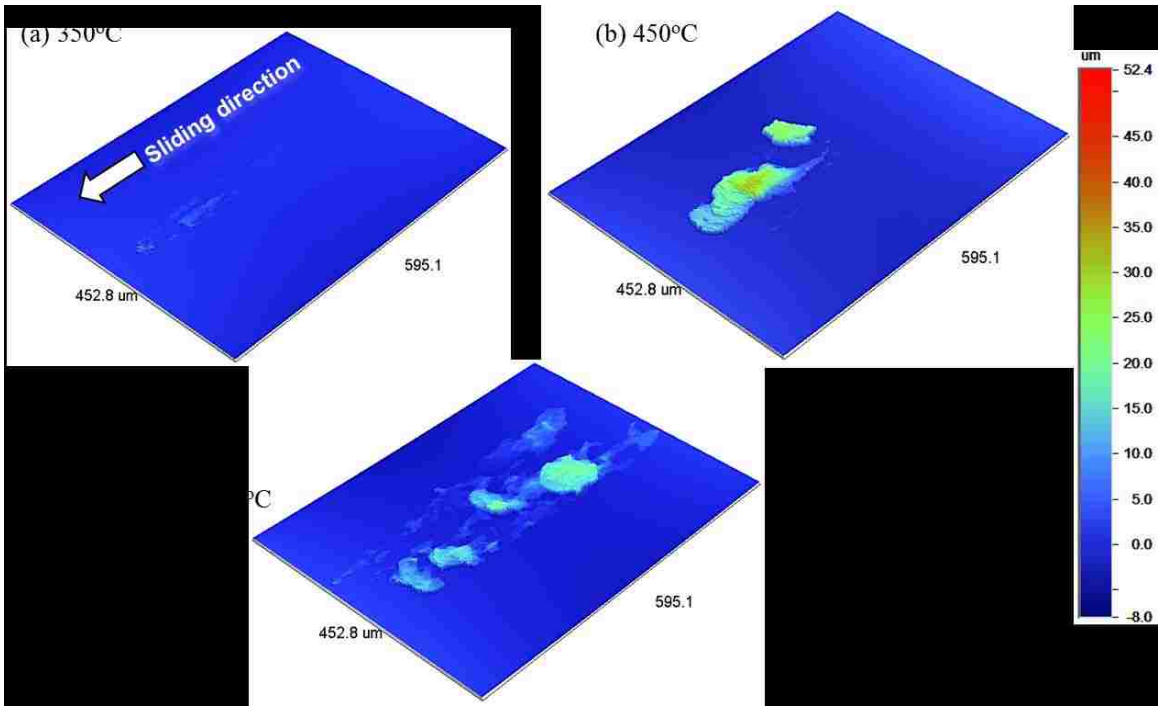

Figure 4.15 3-D profilometery images of material adhered to counterface, P20 pin while sliding against AA6061 strips at $\dot{\varepsilon} = 4\times 10^{-2}\ s^{-1}$: (a) T = 350°C, (b) T = 450°C, (d) T = 545°C

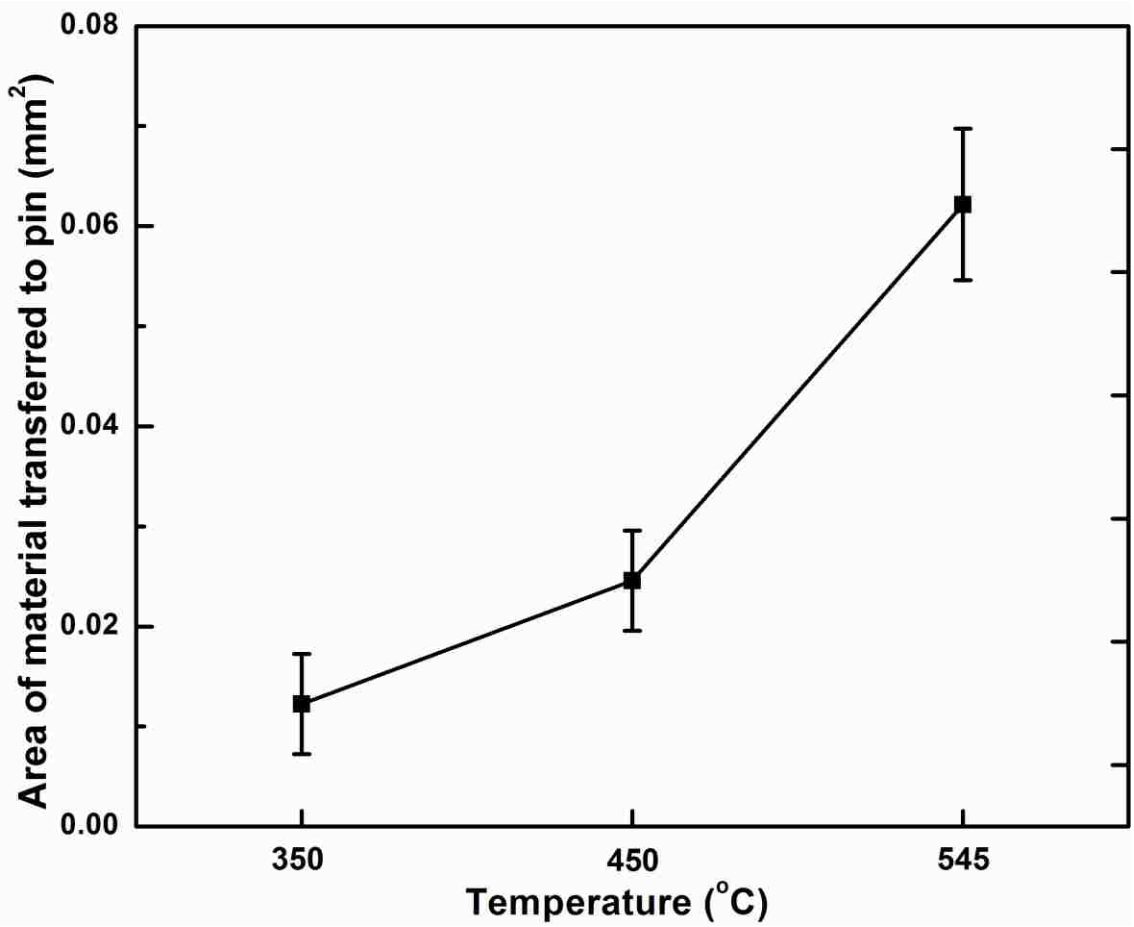

Figure 4.16 Variation of material transferred to counterface P20 Pin while sliding against AA6061 strips at $\dot{\varepsilon} = 4\times 10^{-2}\ s^{-1}$

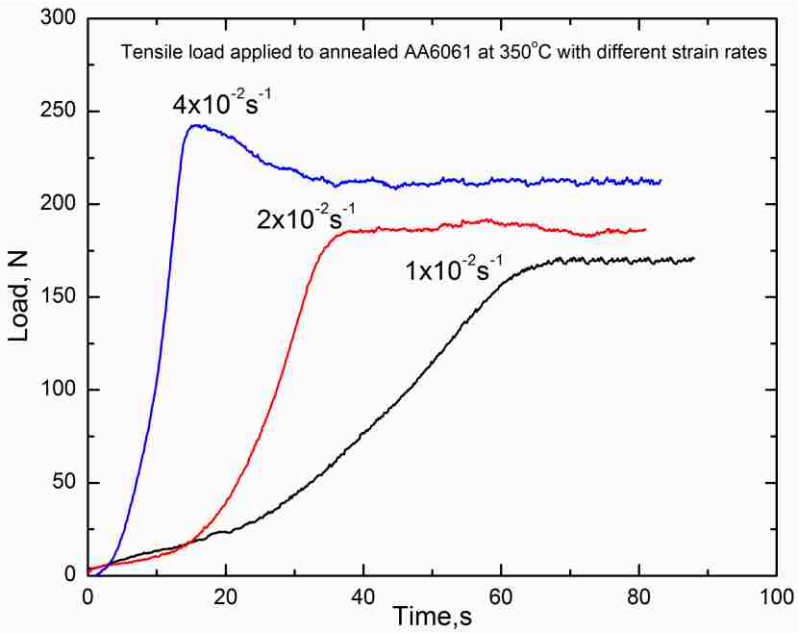
Tensile load applied to annealed AA6061 at 350°C with different strain rates
4x10-2s-1
2x10-2s-1
1x10-2s-1
Load, N
Time,s
0
50
100
150
200
250
300
0
20
40
60
80
100

(a)

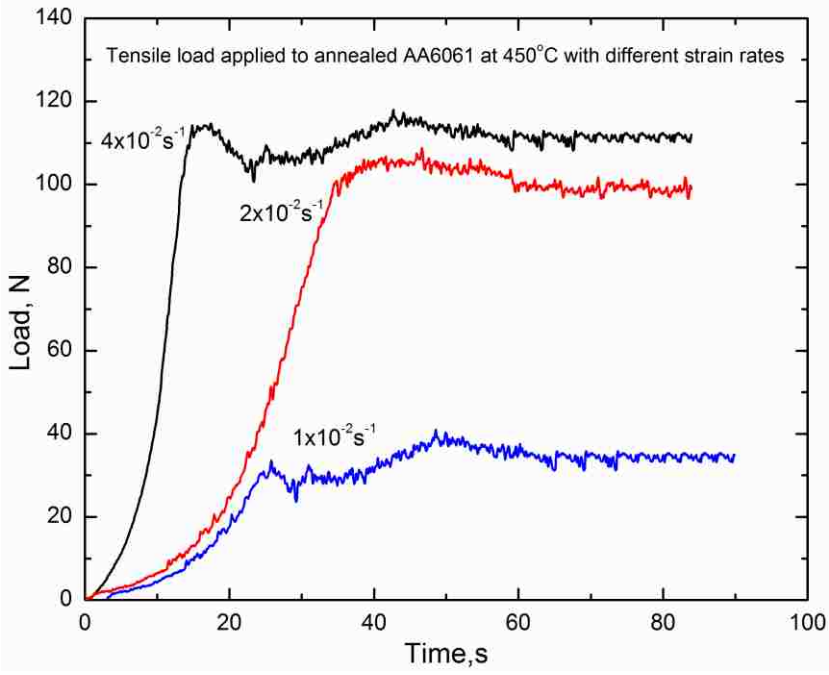
Tensile load applied to annealed AA6061 at 450°C with different strain rates
4x10-2s-1
2x10-2s-1
1x10-2s-1
Load, N
Time,s
0
20
40
60
80
100
120
140
0
20
40
60
80
100

(b)

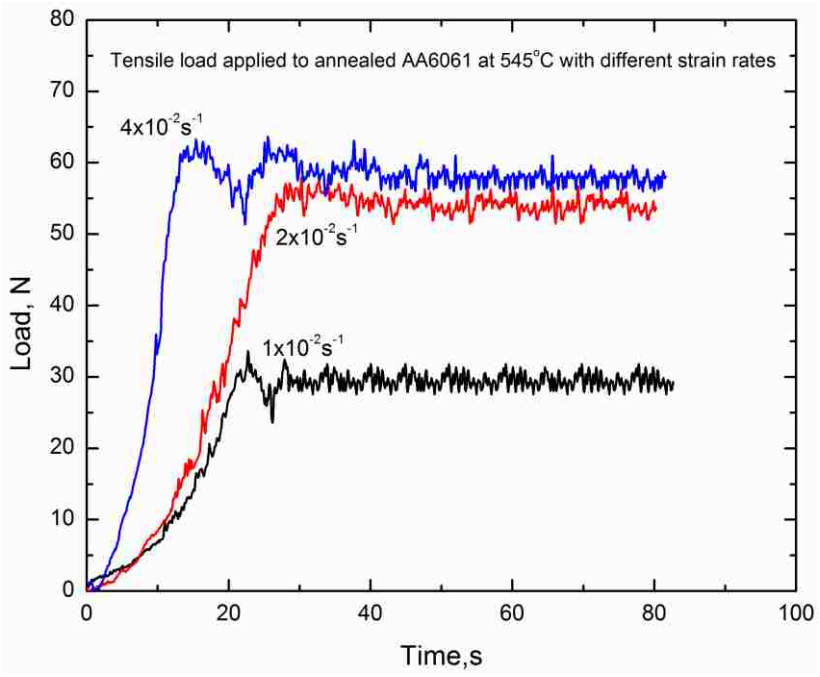

(c)

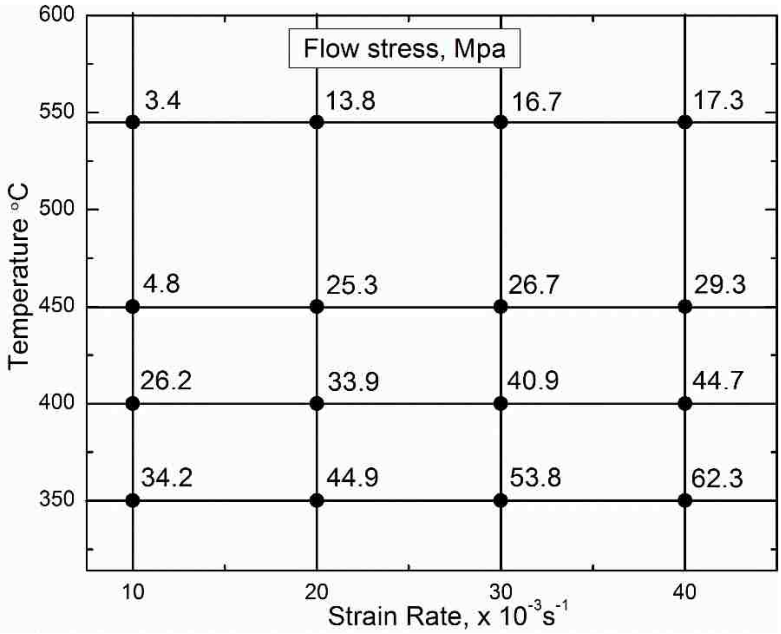

(d)

Figure 4.17 Tensile loads applied to AA6061 strips at different strain rates at (a) 350 °C; (b) 450°C and (c) 545 °C. (The time axis indicates the duration of the test, during which a different section of the forward moving strip – 170 mm in length – passes through the hot zone. The flow stress of the strip was calculated at the section that enters the hot zone within a time interval, from 70s to 80s). (d) Flow stress calculated from experimental data in (a) to (c) and plotted on temperature vs. strain rate axes.

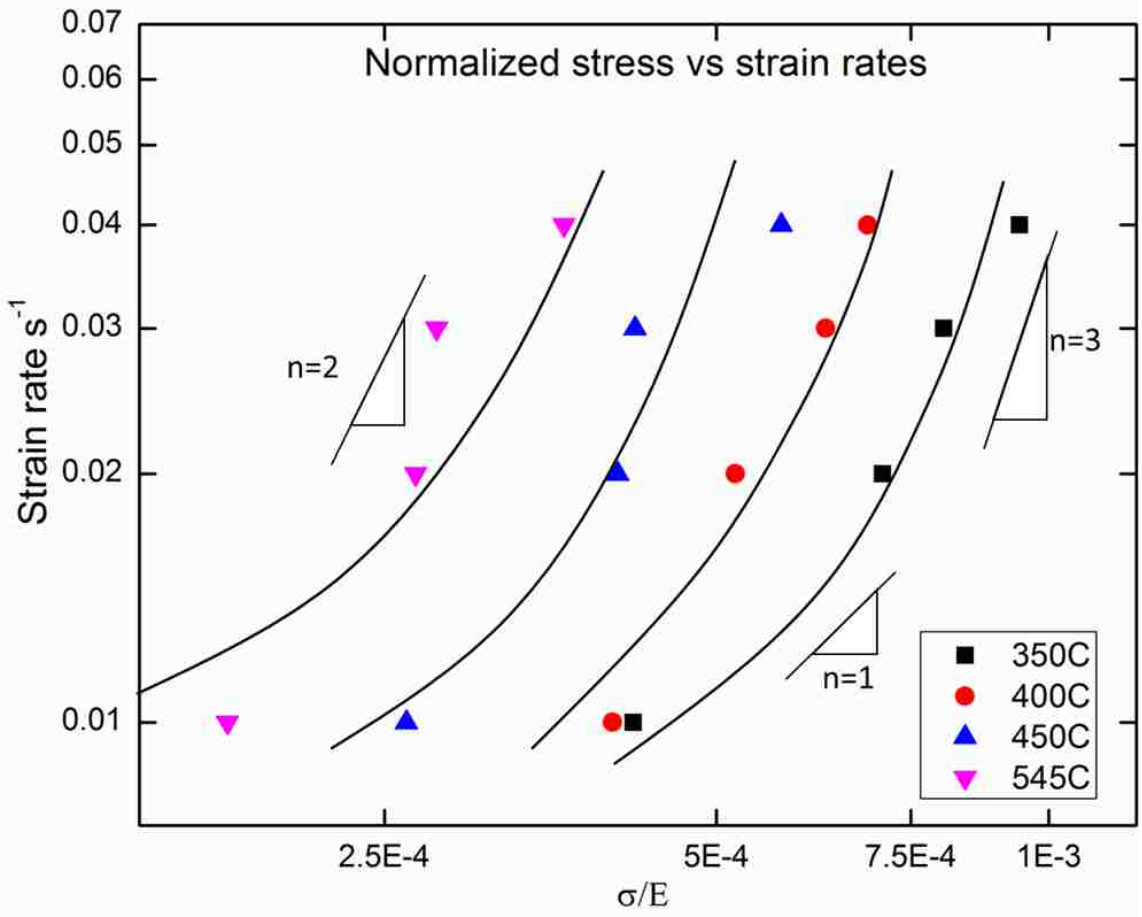

Figure 4.18 Strain rate vs. modulus compensated flow stress plots following the general creep equation where '*n*' is the stress exponent.

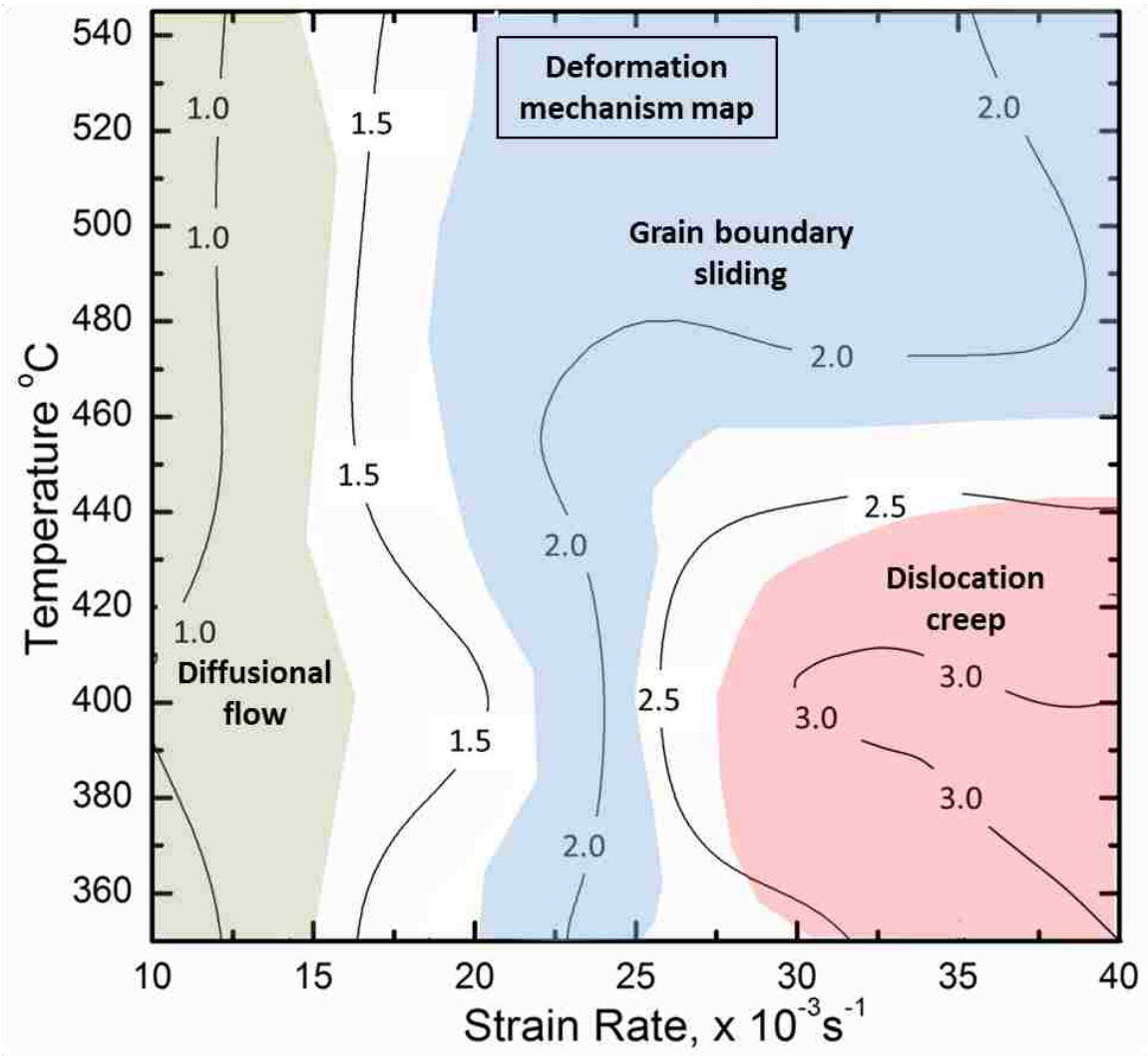

Figure 4.19 Deformation mechanism map (DMM) for AA6061plotted on temperature vs. strain rate axes, where the regions of dominance for each mechanism are identified based on the stress exponent value, *n*. The contours are for constant stress exponent values.

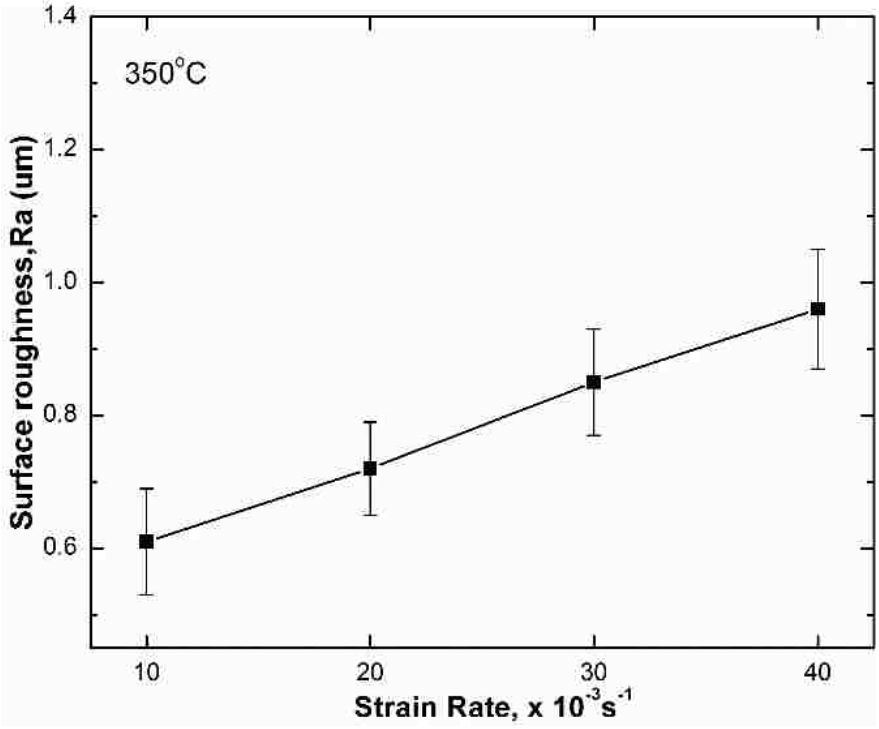
350°C
Surface roughness,Ra (um)
1.4
1.2
1.0
0.8
0.6
10
20
30
40
Strain Rate, x 10-3s-1

(a)

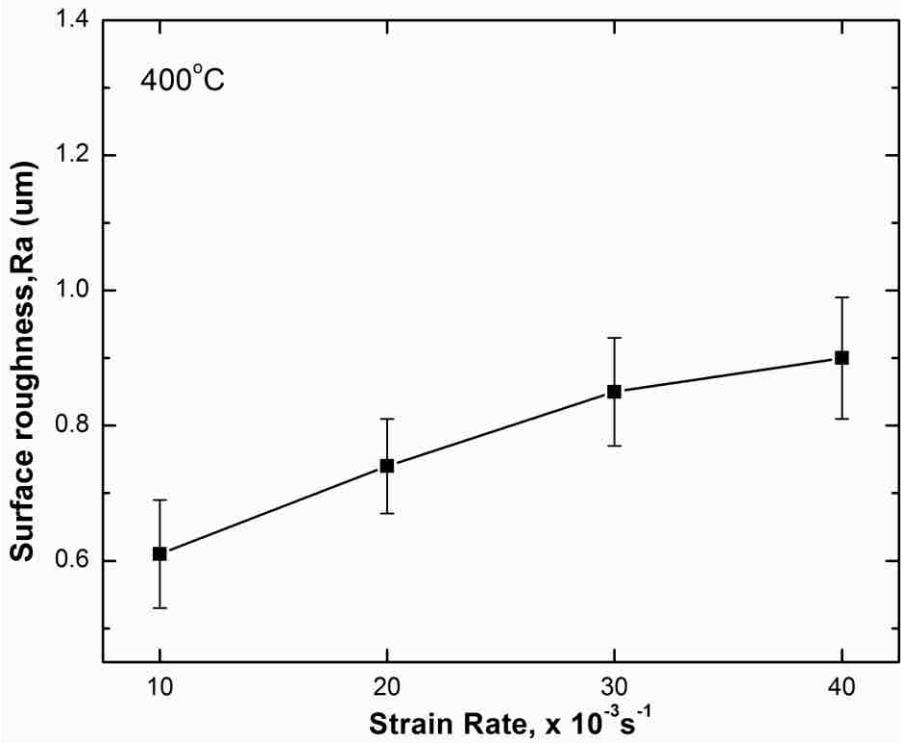
400°C
Surface roughness,Ra (um)
1.4
1.2
1.0
0.8
0.6
10
20
30
40
Strain Rate, x 10-3s-1

(b)

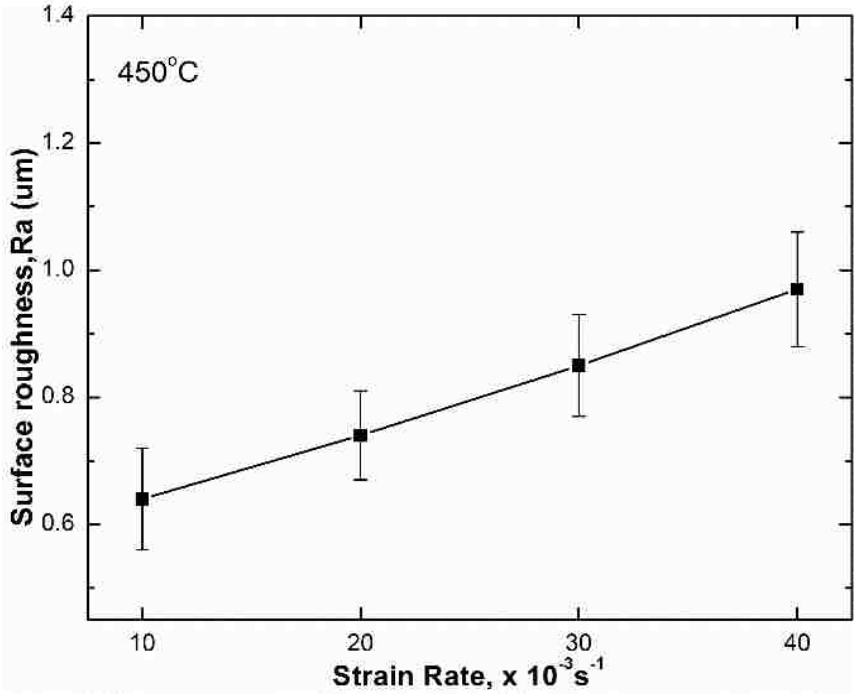

(c)

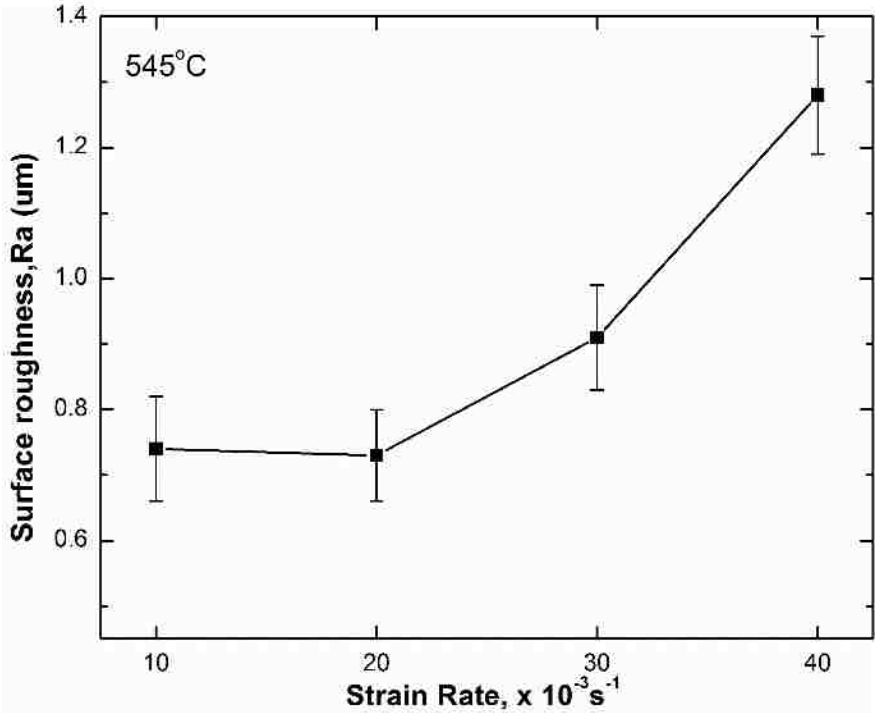

(d)

Figure 4.20 Surface roughness measurement for surface deformed at four temperatures (a) T = 350°C, (b) T = 400°C, (c) T = 450°C, (d) T = 545°C.

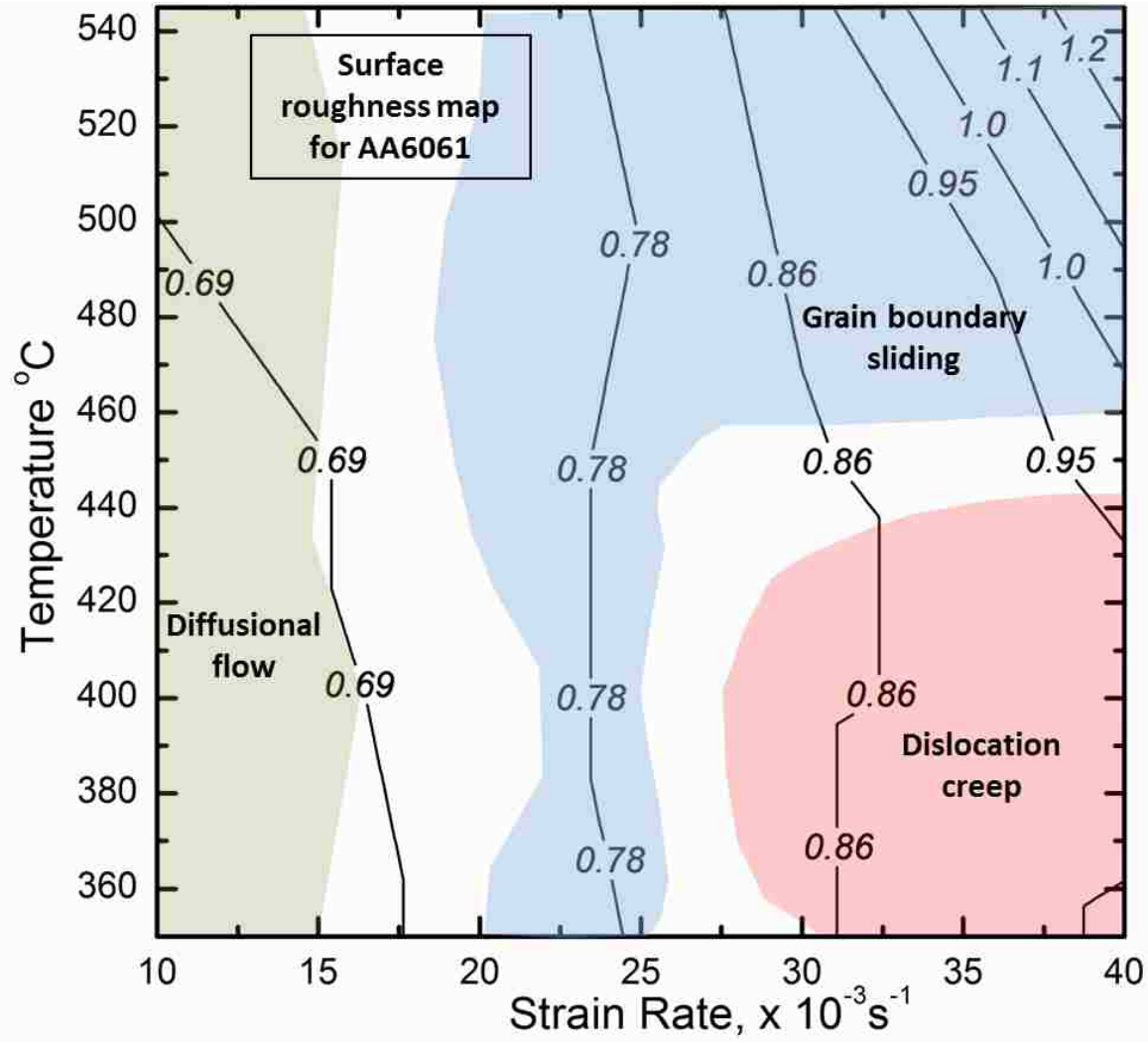

Figure 4.21 Surface roughness map for AA6061 plotted on temperature vs. strain rate axes, where the regions of dominance for each mechanism are identified based on the stress exponent value, *n*. The contours are for constant surface roughness Ra.

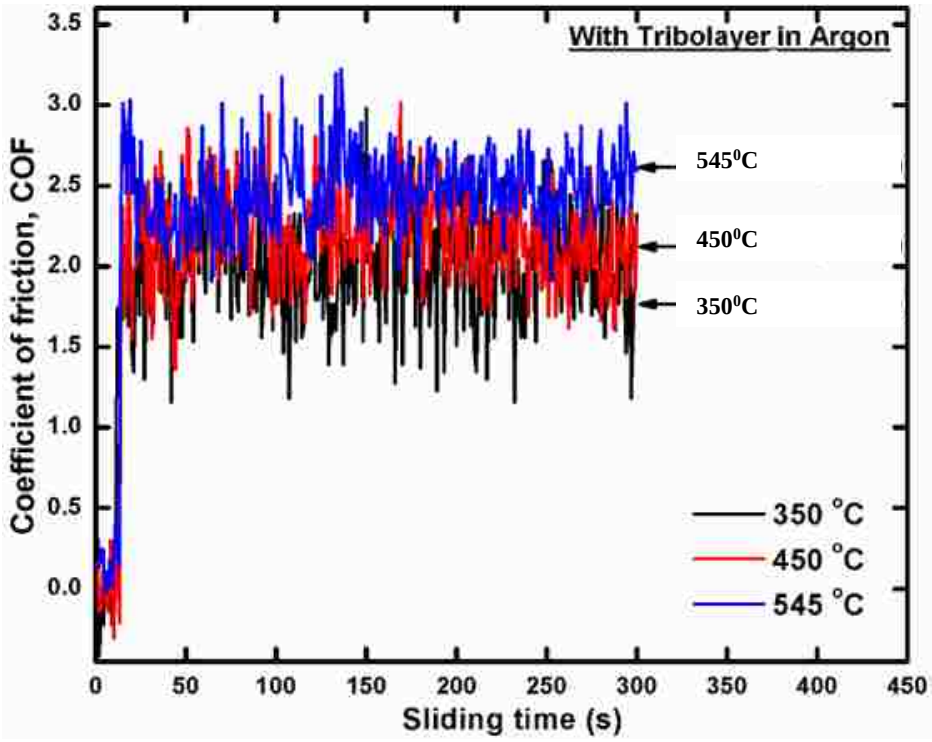

(a)

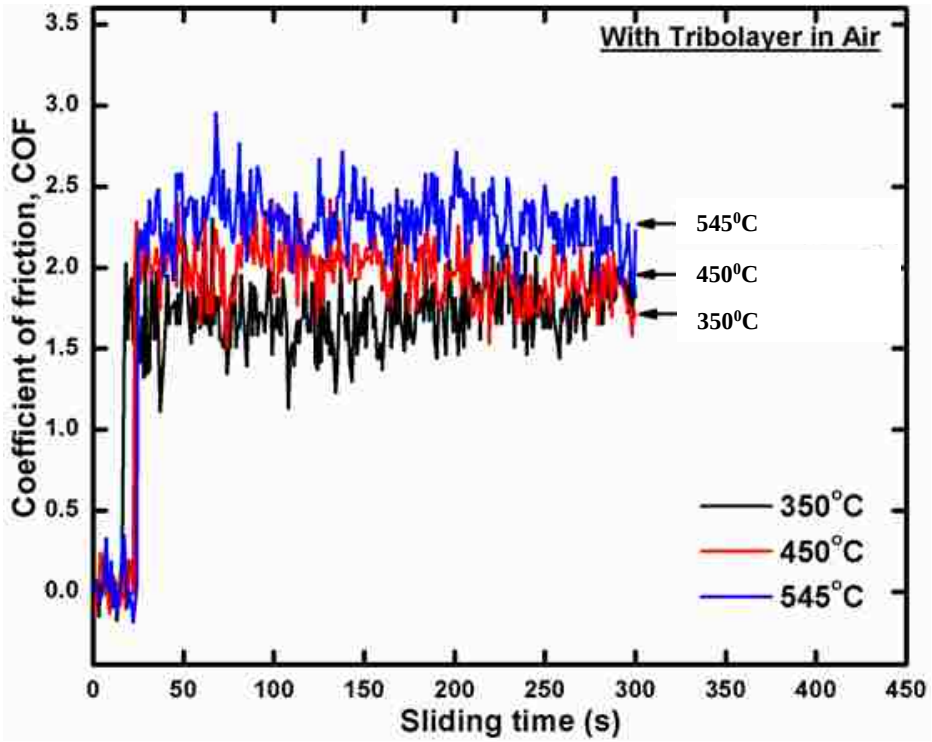

(b)

Figure 4.22 COF vs. sliding time plot for unpolished strips at three temperatures and strain rates of 4×10^{-2} s^{-1} in (a) argon and (b) in air.

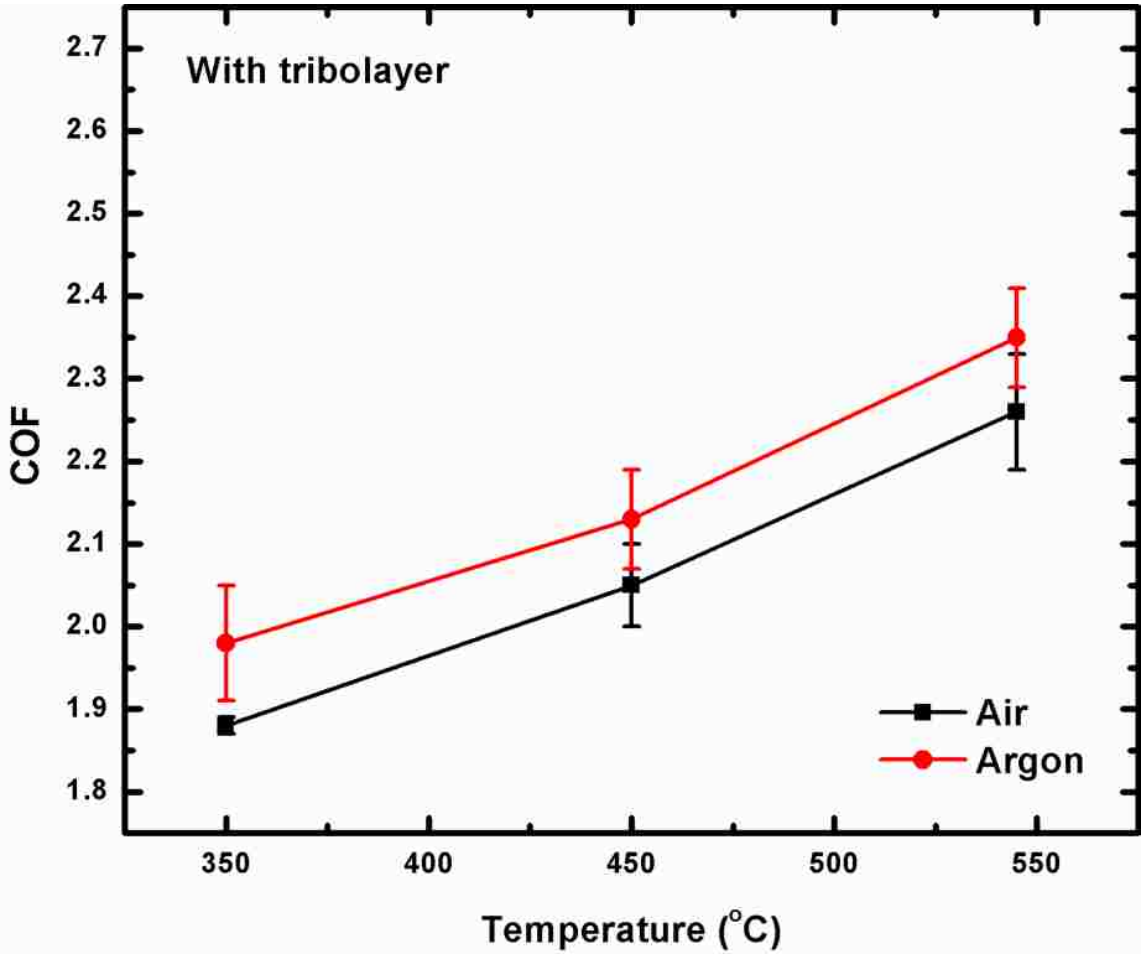

Figure 4.23 Average COF vs. temperature plot for unpolished strips at three temperatures and strain rates of 4×10^{-2} s^{-1} in argon and air, where error bars indicate range of fluctuations in mean COF values.

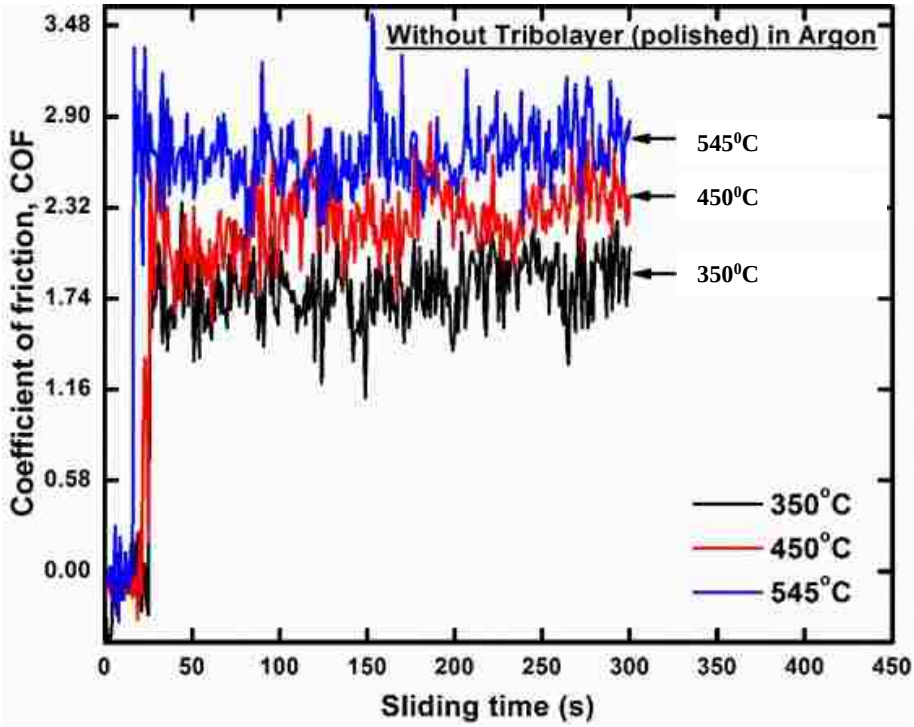

(a)

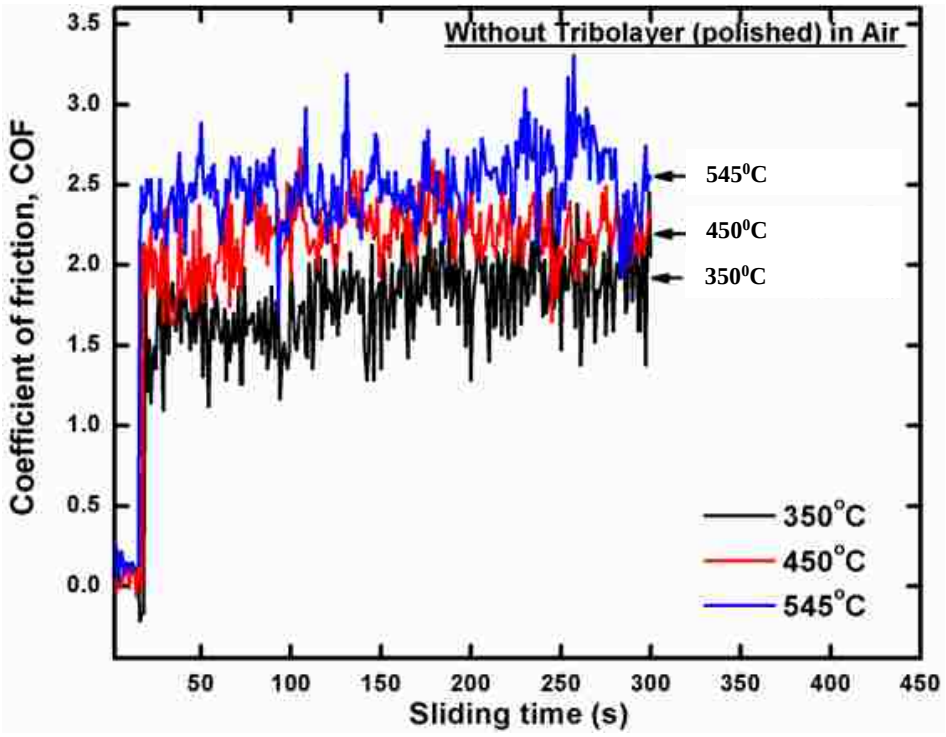

(b)

Figure 4.24 COF vs. sliding time plot for polished strips at three temperatures and strain rates of 4×10^{-2} s^{-1} in (a) argon and (b) in air.

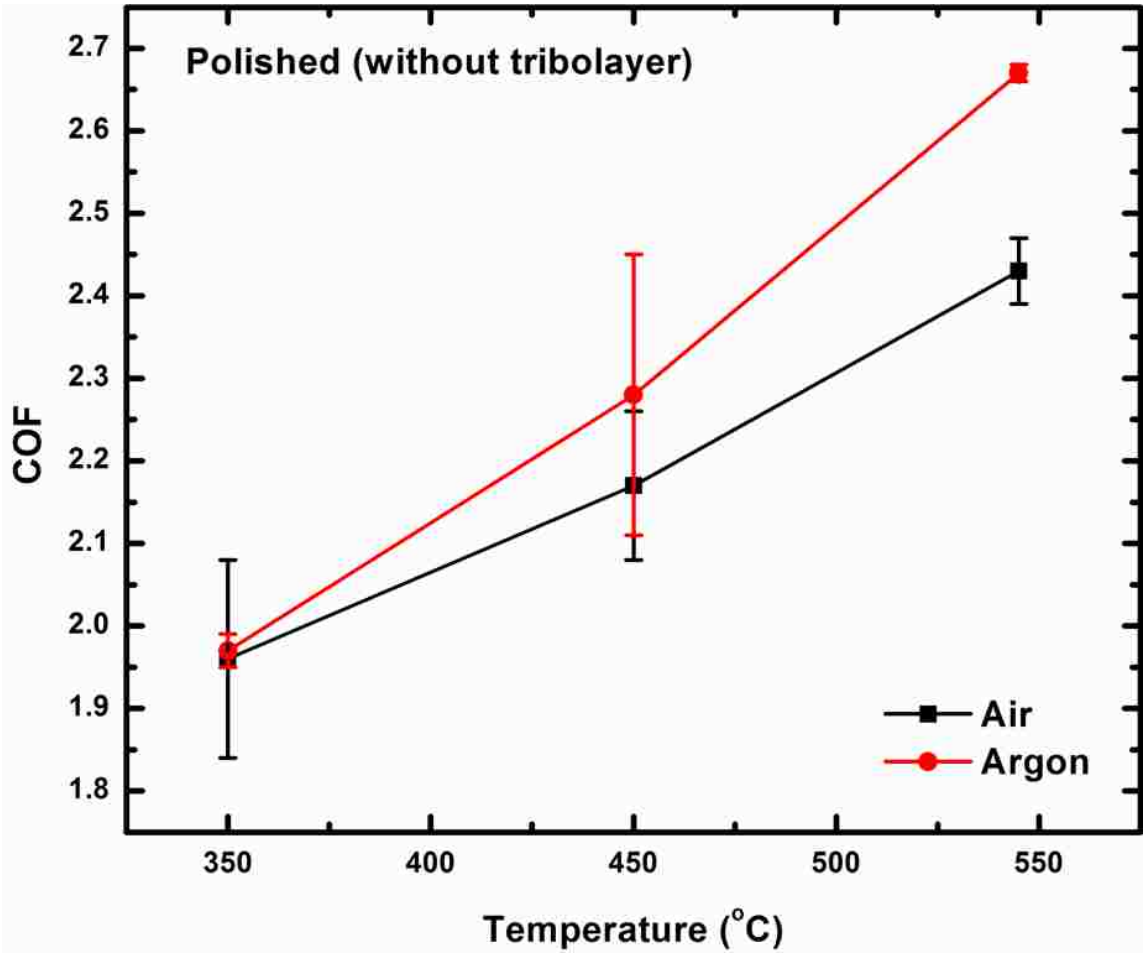

Figure 4.25 Average COF vs. temperature plot for polished strips at three temperatures and strain rates of 4×10^{-2} s^{-1} in argon and air, where error bars indicate range of fluctuations in mean COF values.

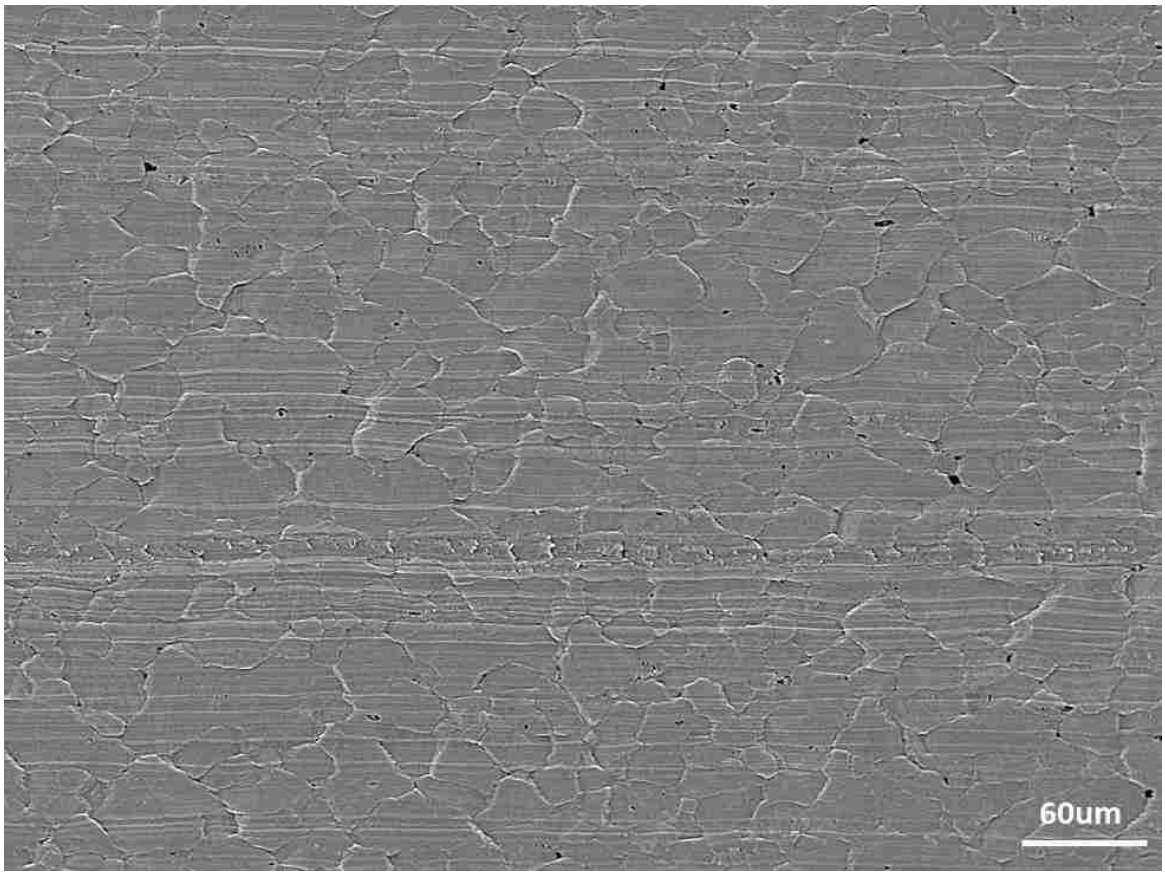

Figure 4.26 Secondary electron image showing the surface morphology of as-received AA6061 strip deformed at elevated temperatures in argon (545 °C and 4×10^{-2} s^{-1}).

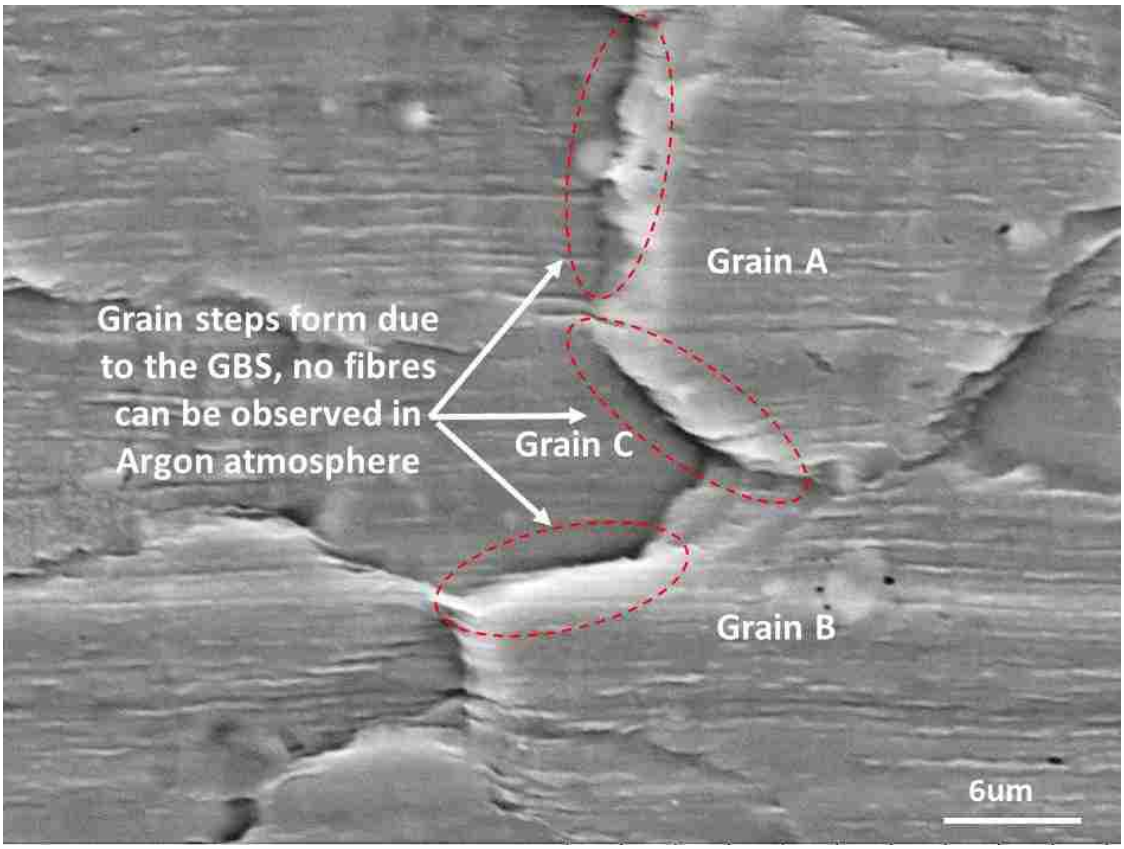

Figure 4.27 A higher magnification view of the sample surface deformed in argon at 545 °C and 4×10^{-2} s^{-1}. Surfaces offset formed due to GBS.

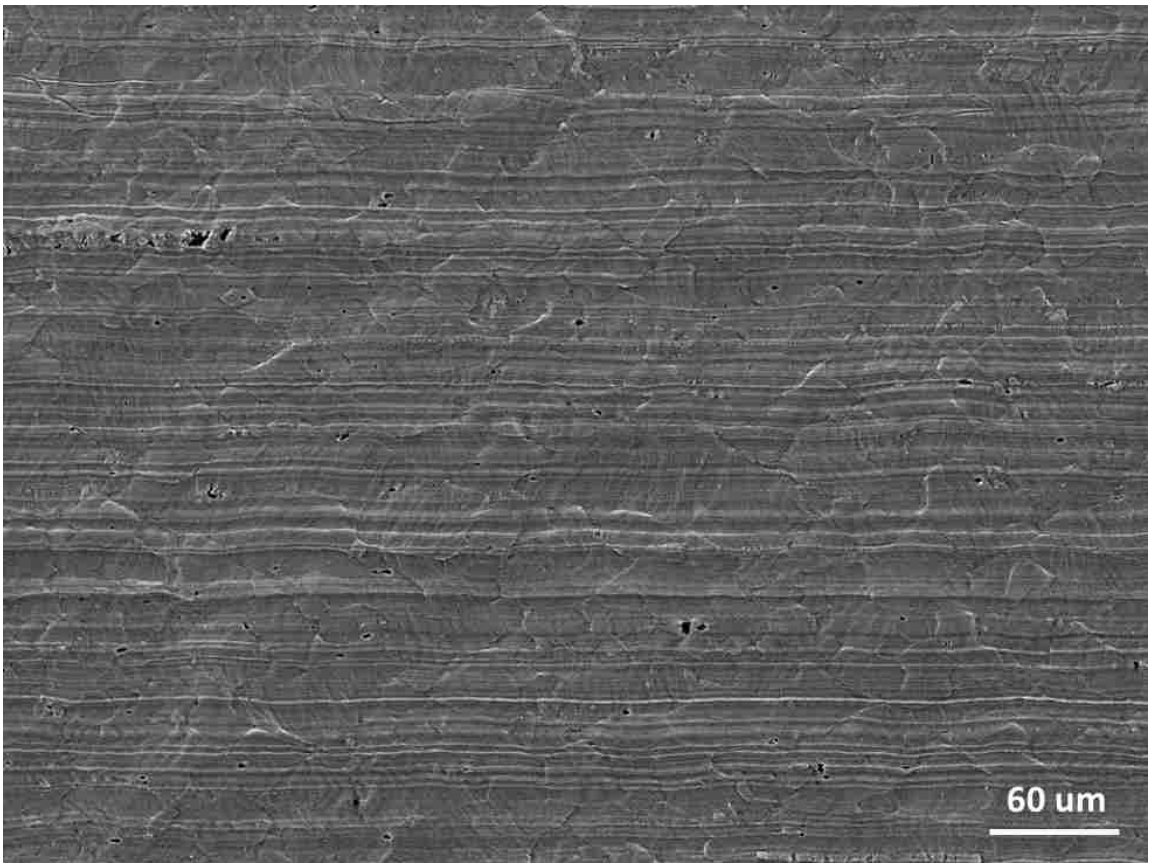

Figure 4.28 Secondary electron image showing the surface morphology of as-received AA6061 strip deformed at elevated temperatures in argon (350 °C and 4×10^{-2} s^{-1}).

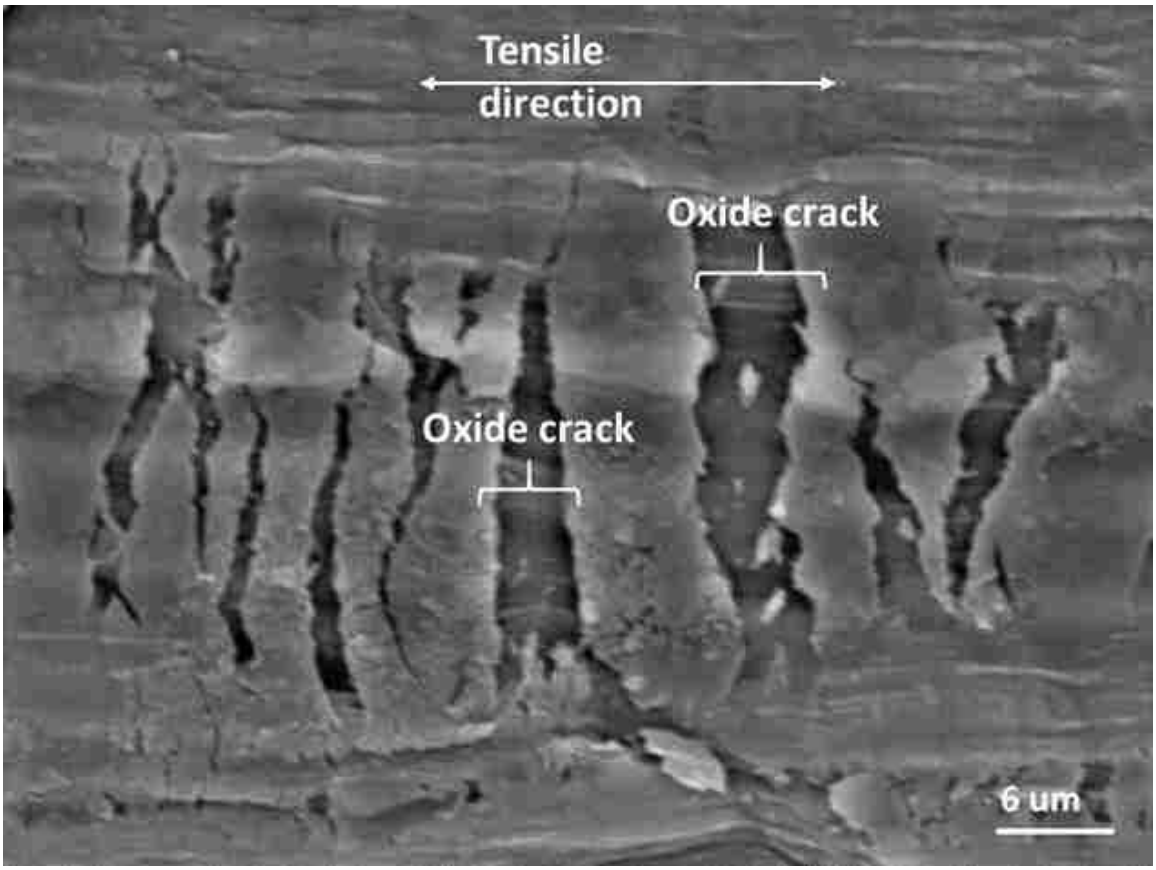

Figure 4.29 . SEM micrographs of the sample deformed in argon at 350 °C and 4×10^{-2} s^{-1}. Cracks in surface oxide indicate the brittle nature of the oxide at lower temperatures and no fibre formed in the crack.

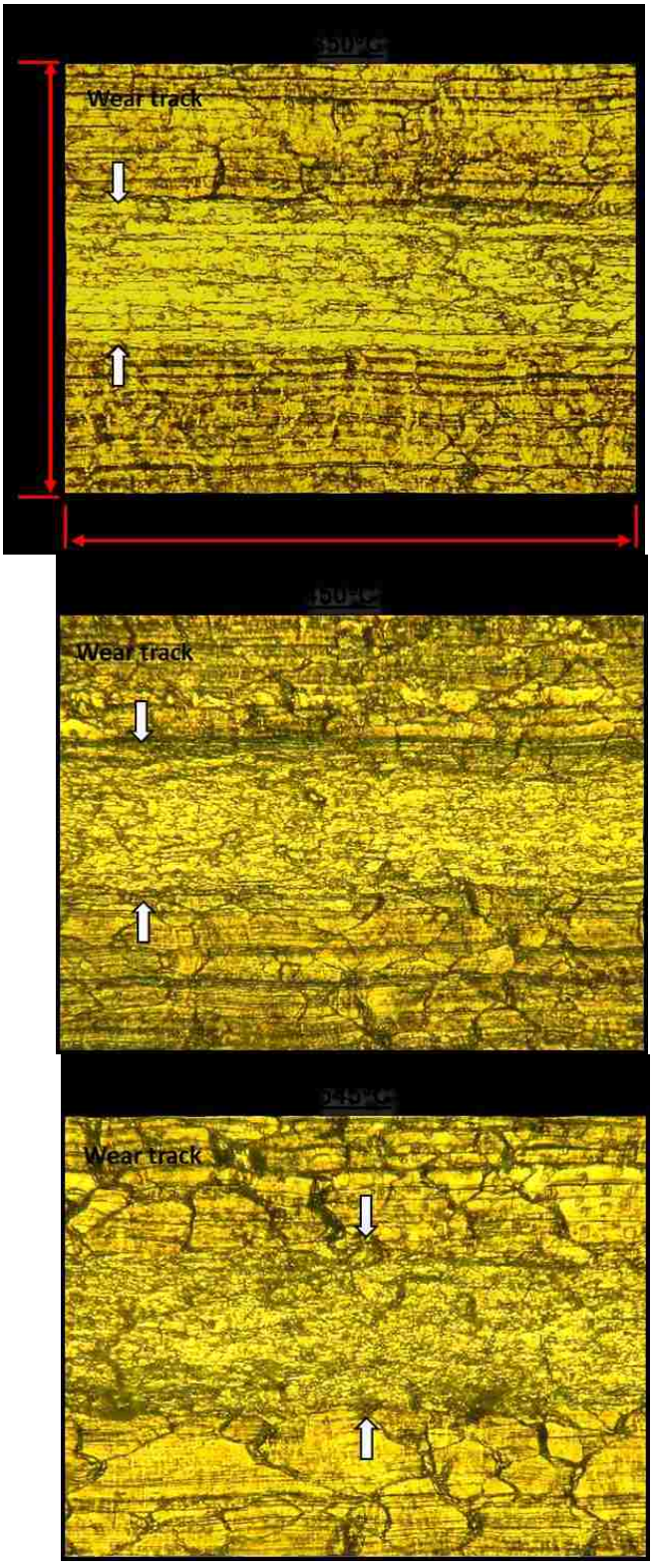

Figure 4.30 Optical microstructure of the wear tracks on unpolished AA6061strips taken from optical microscope obtained in argon at 0.04 s^{-1}: (a) at 350ºC, (b) at 450ºC, (c) at 545ºC.

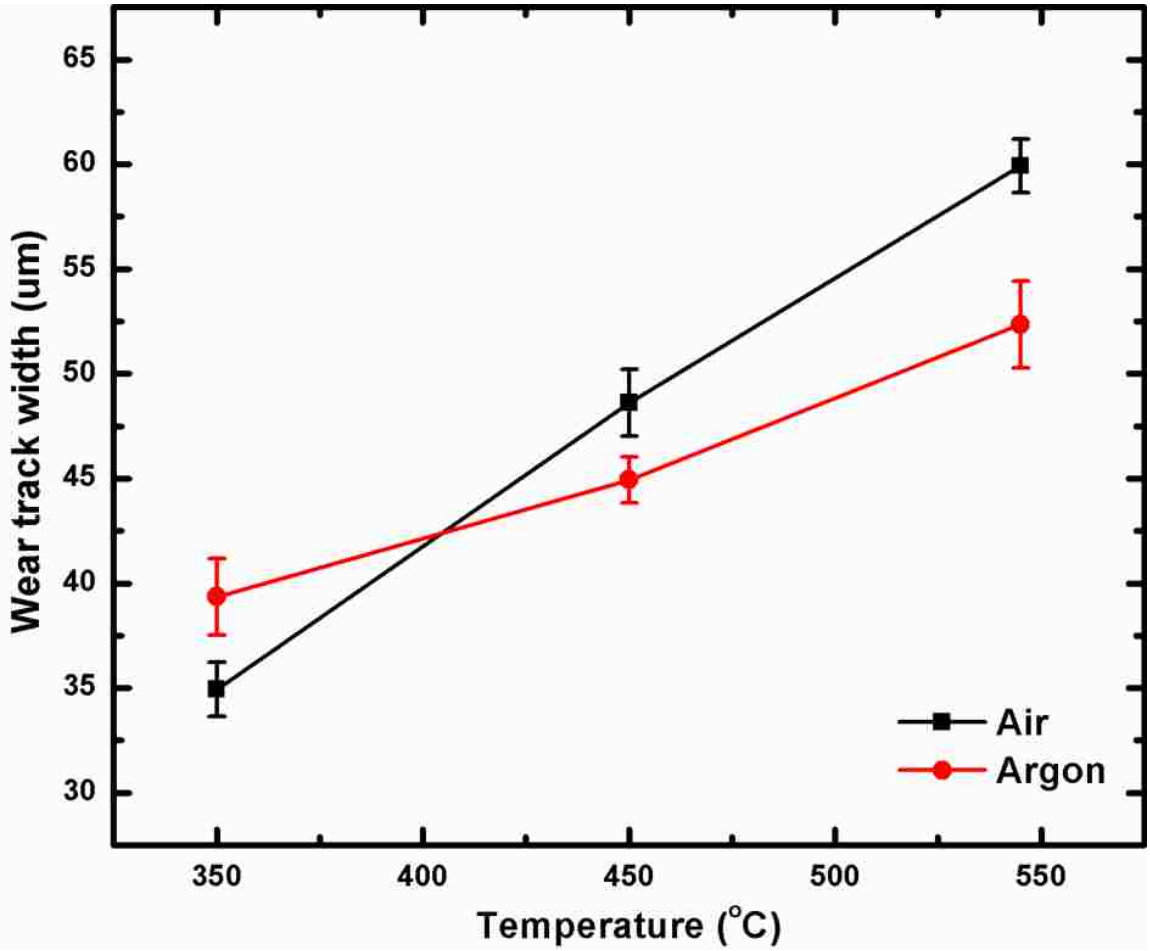

Figure 4.31 Changes in the width of the sliding induced wear track on the AA6061 strip unpolished condition in contact with the P20 steel pin at various temperatures in air and argon environment.

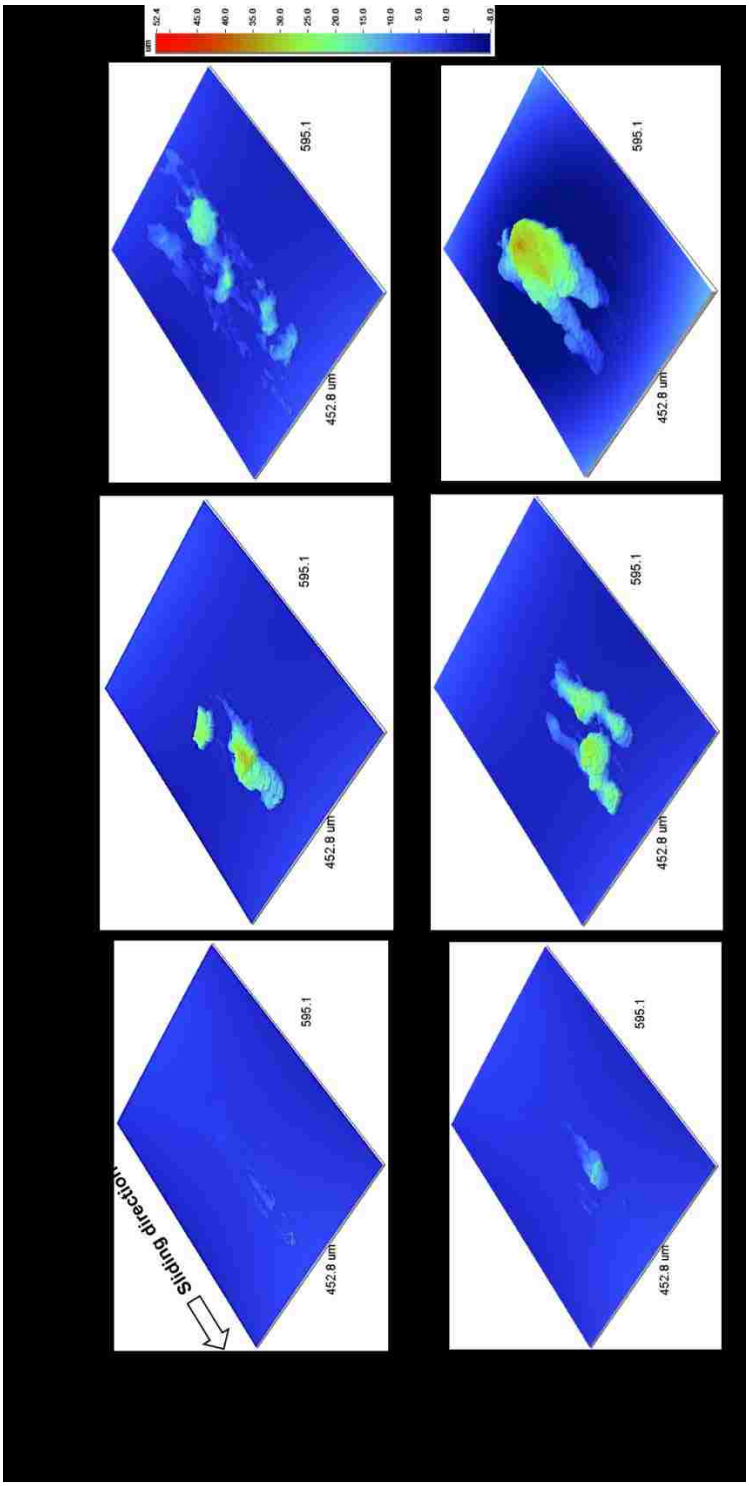

Figure 4.32 Comparison of 3-D profilometery images of material adhered to counterface P20 Pin while sliding against AA6061 strips with tribolayer in air and argon environment.

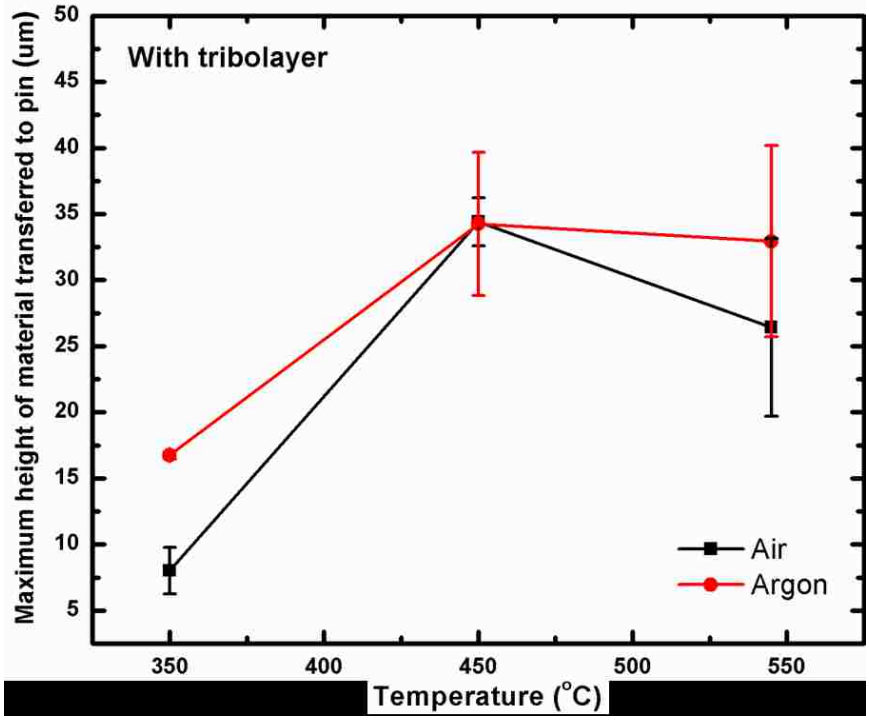

(a)

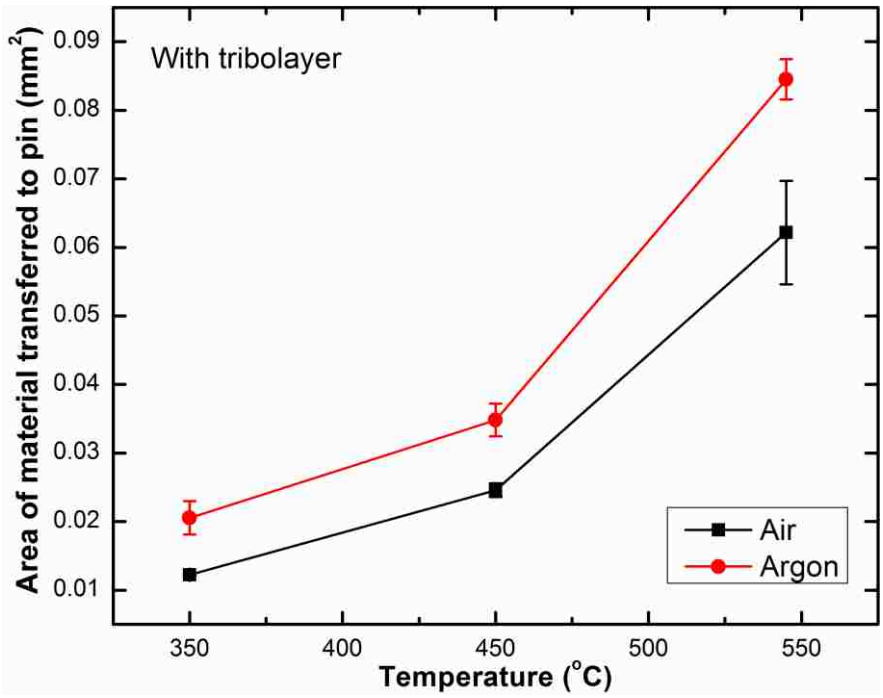

(b)

Figure 4.33 Comparison of transferred material to counterface: (a) maximum height of material transferred to counterface P20 pin while sliding against AA6061 Strips with tribolayer. (b) Area of material transferred to counterface P20 pin while sliding against AA6061 Strips with tribolayer.

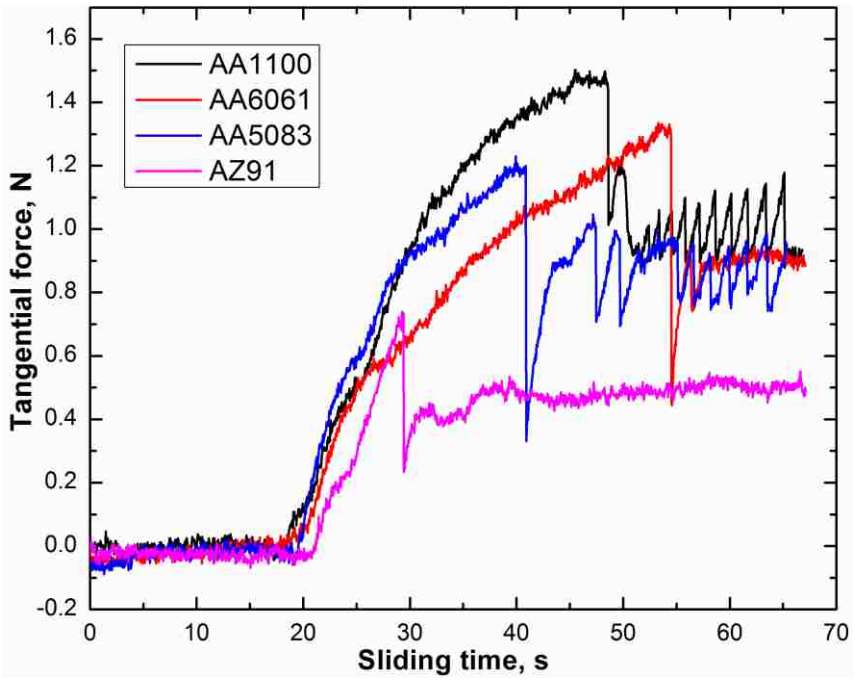

(a)

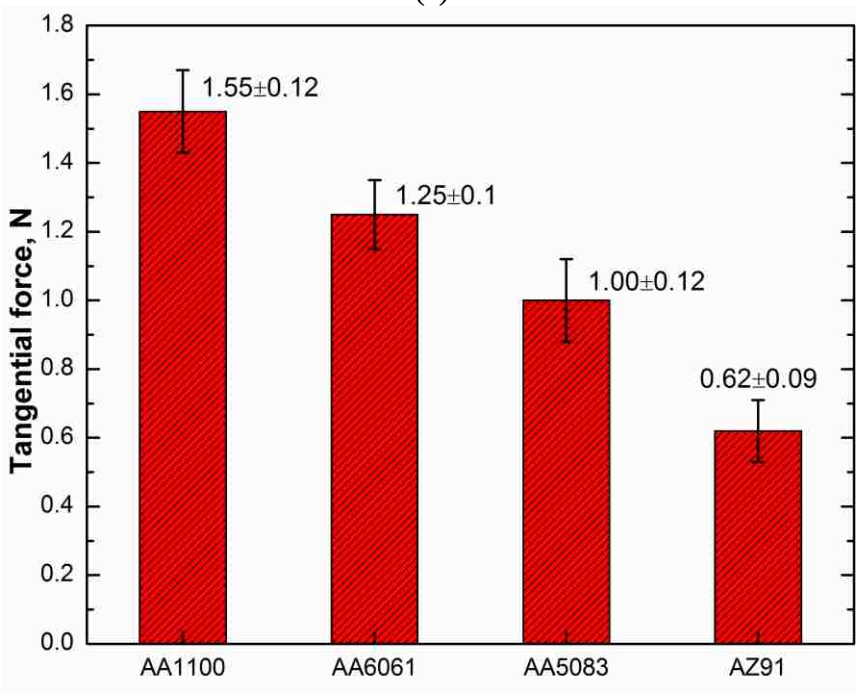

(b)

Figure 4.34 (a) The variations of the tangential forces versus time for each of the alloys tested in air. (b) Average values of junction strength for each alloy (maximum tangential stress reached before the failure of adhesive junction).

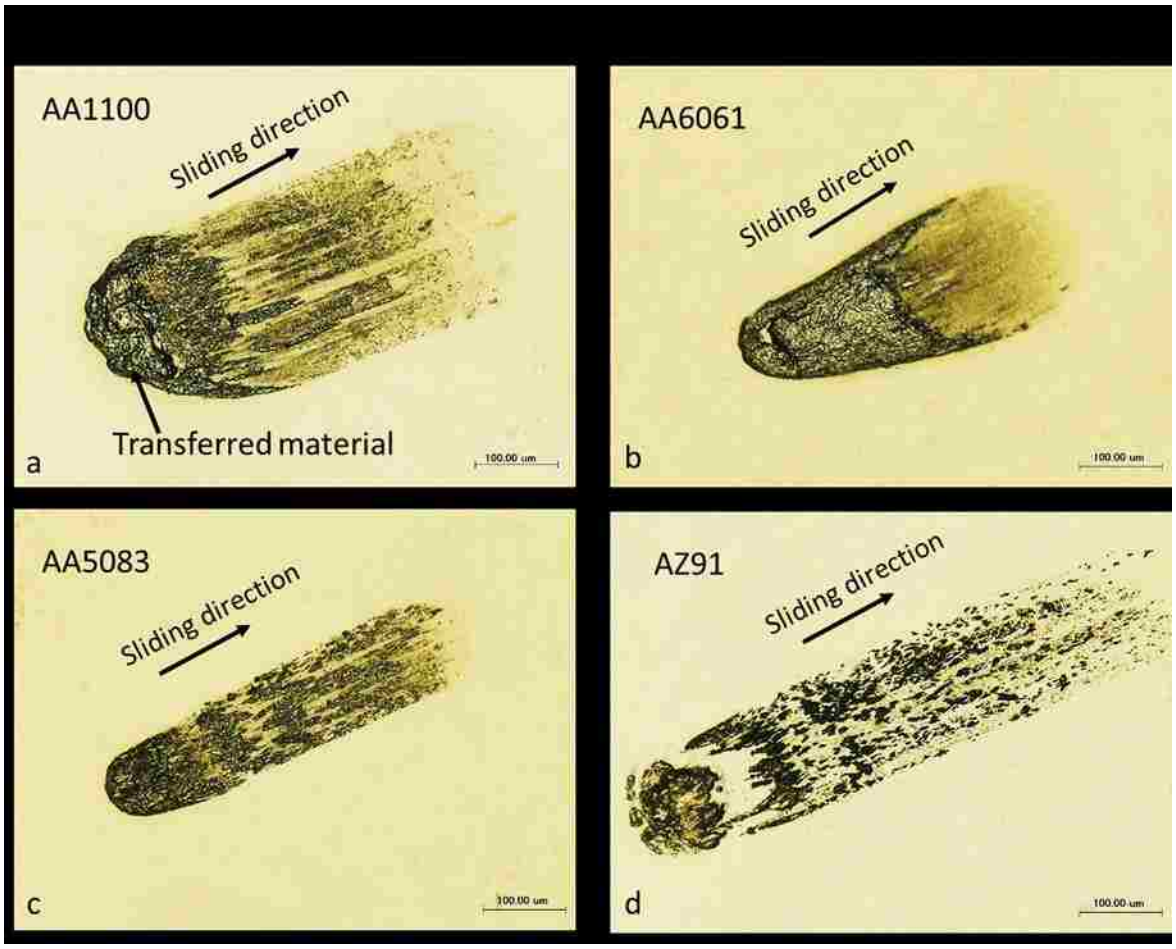

Figure 4.35 Microstructures of transferred material on M2 steel counterface surfaces tested against different alloys: (a) AA1100, (b) AA6061, (c) AA5083, (d) AZ91.

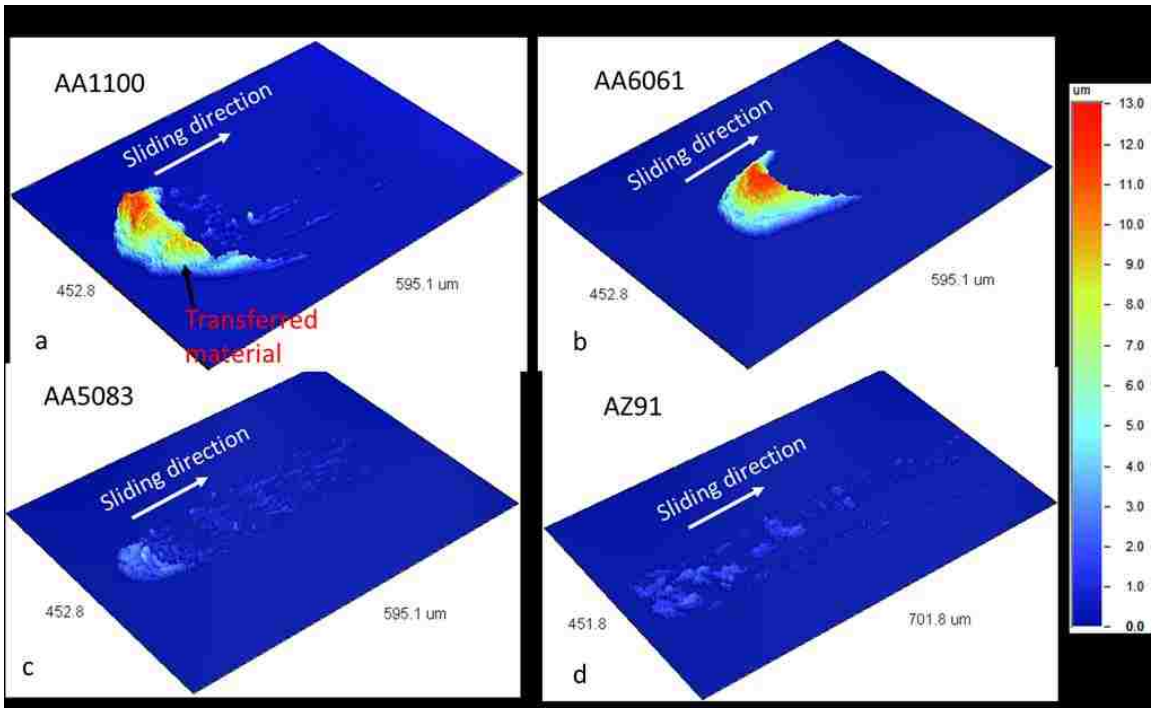

Figure 4.36 3-D profilometry images of the adhered material on the steel counterface surfaces tested against different alloys in air: (a) AA1100, (b) AA6061, (c) AA5083, (d) AZ91.

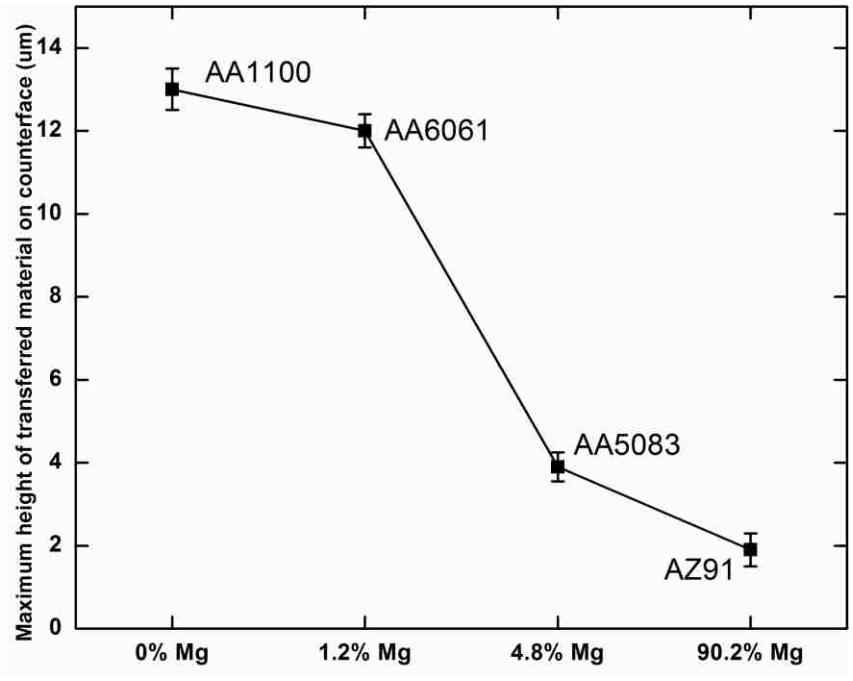

(a)

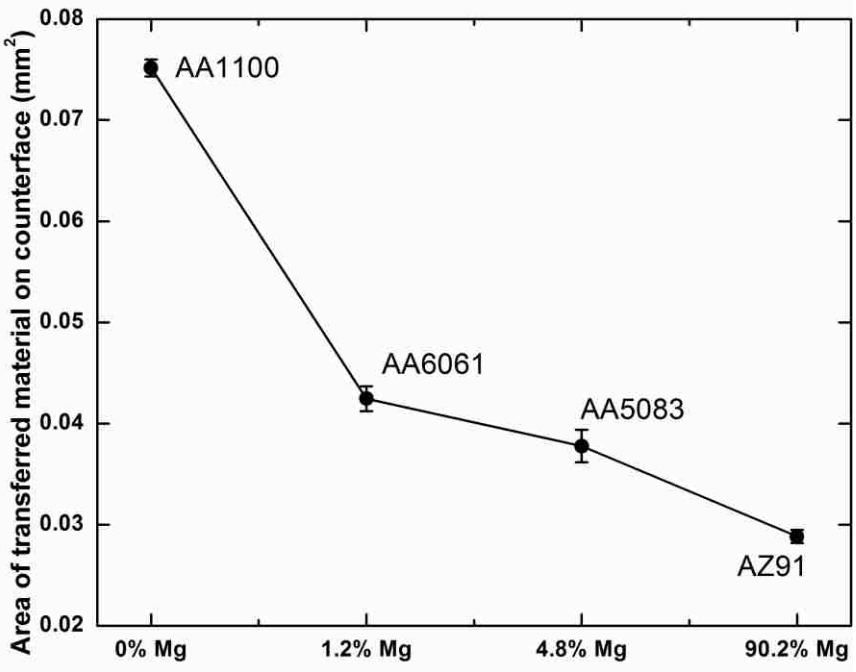

(b)

Figure 4.37 Comparison of transferred material to M2 steel counterface: (a) maximum height of material transferred to counterface sliding against alloys with different Mg content (b) Area of material transferred to counterface sliding against alloys with different Mg content.

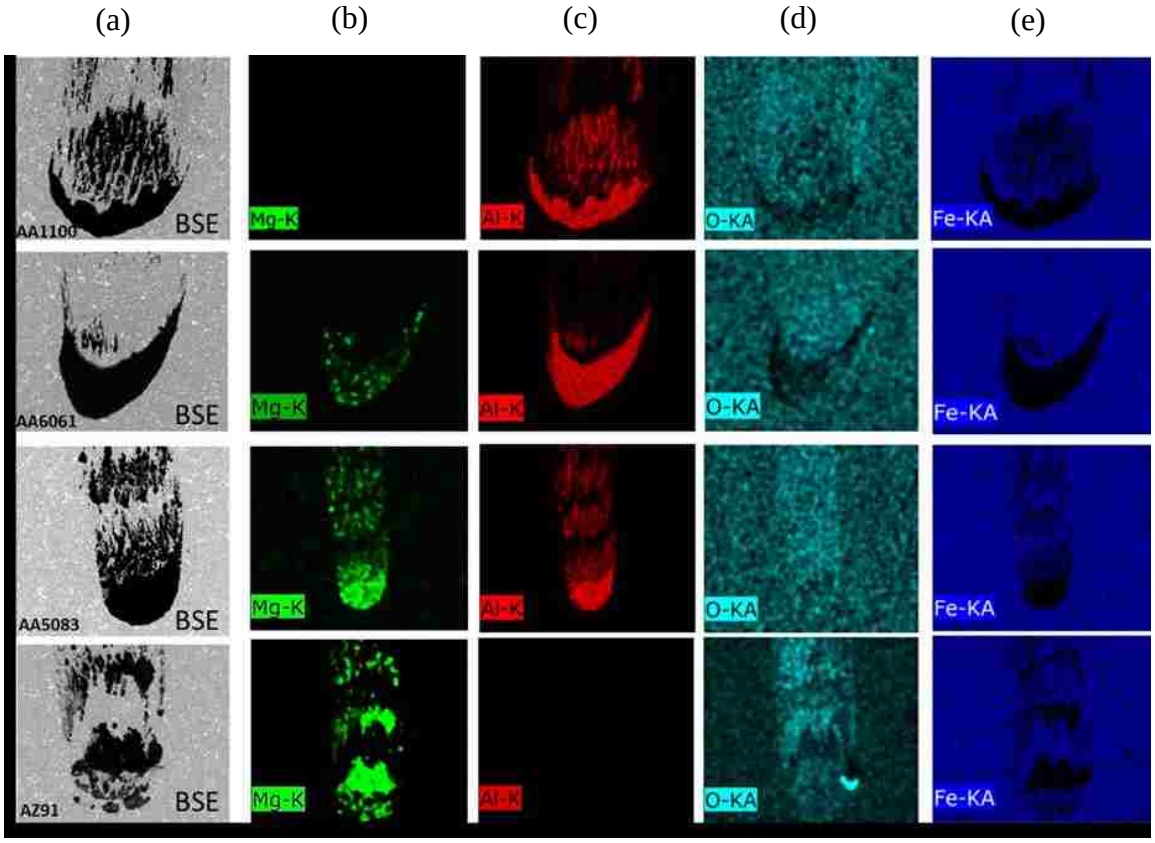

Figure 4.38 EDS maps of the elements, Al, Mg, Fe, O, found on the contact areas on steel counterface after testing against alloys with different magnesium content in air. The images on the column (a) are the BSE images of the same areas for each alloy tested, column (b) (c) (d) (e) are element maps of Mg, Al, O, Fe.

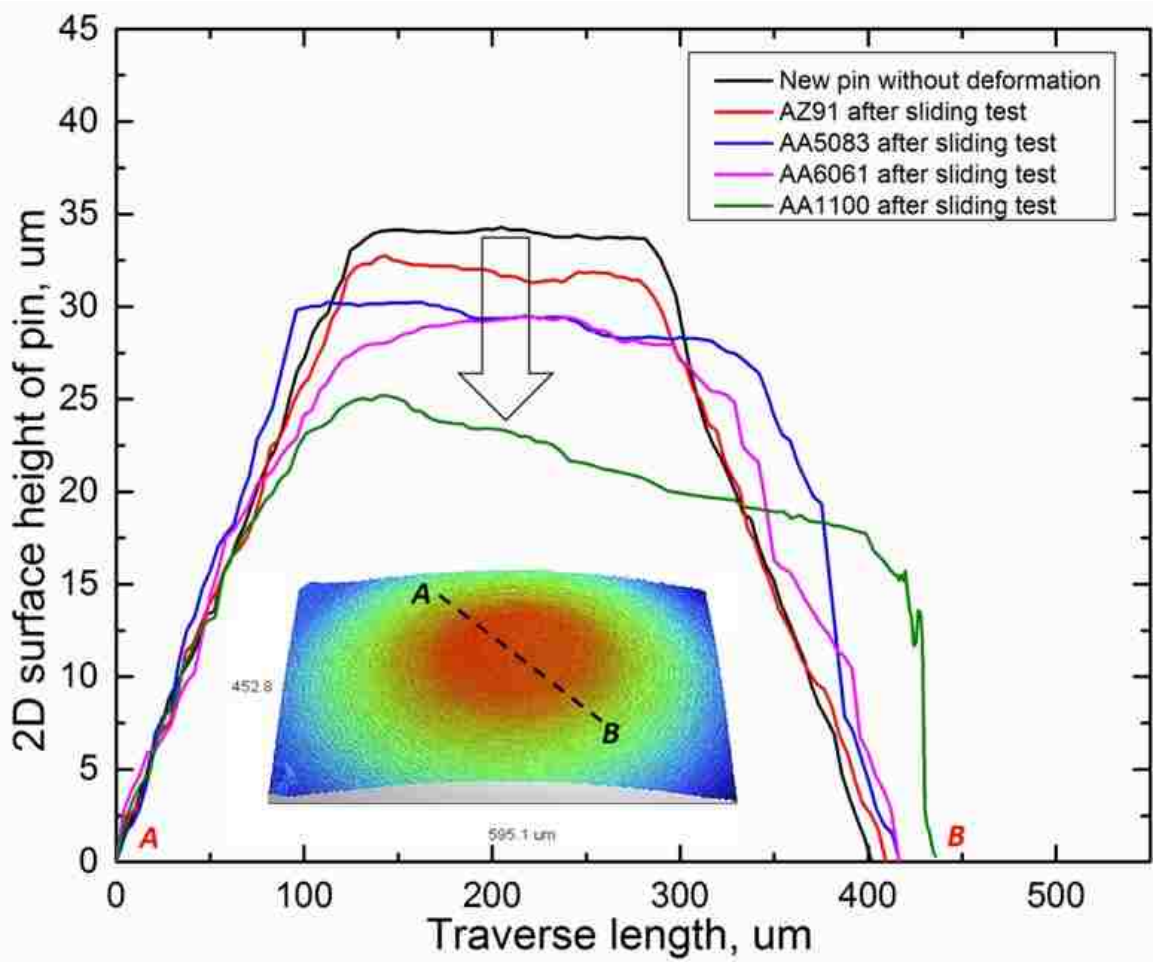

Figure 4.39 2-Dimensional surface profile measurements of the pin tips, starting from point A and continuing upto B of a representative tip (shown in the inset), after sliding tests.

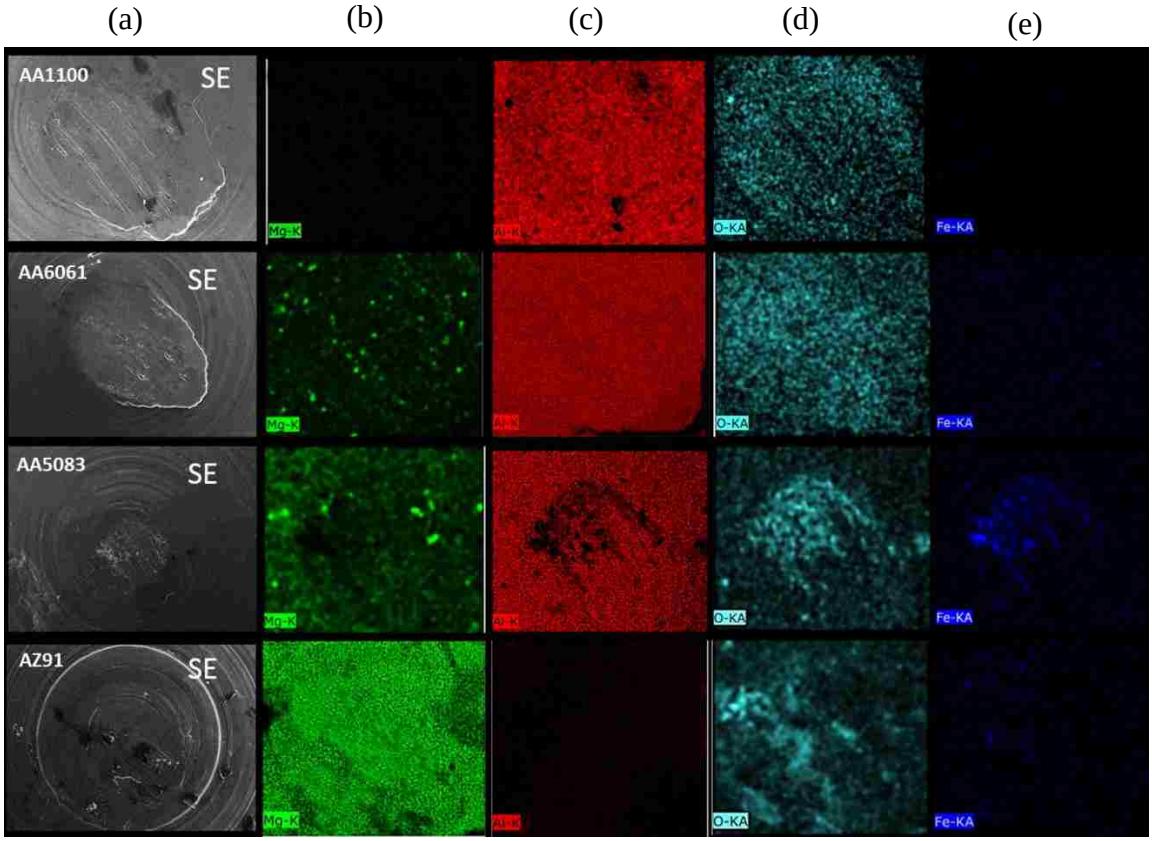

Figure 4.40 EDS maps of the elements, Al, Mg, Fe, O, found on the contact areas on alloy surface after testing against with counterface in air. The images on the column (a) are the SE images of the same areas for each alloy tested, column (b) (c) (d) (e) are element maps of Mg, Al, O, Fe.

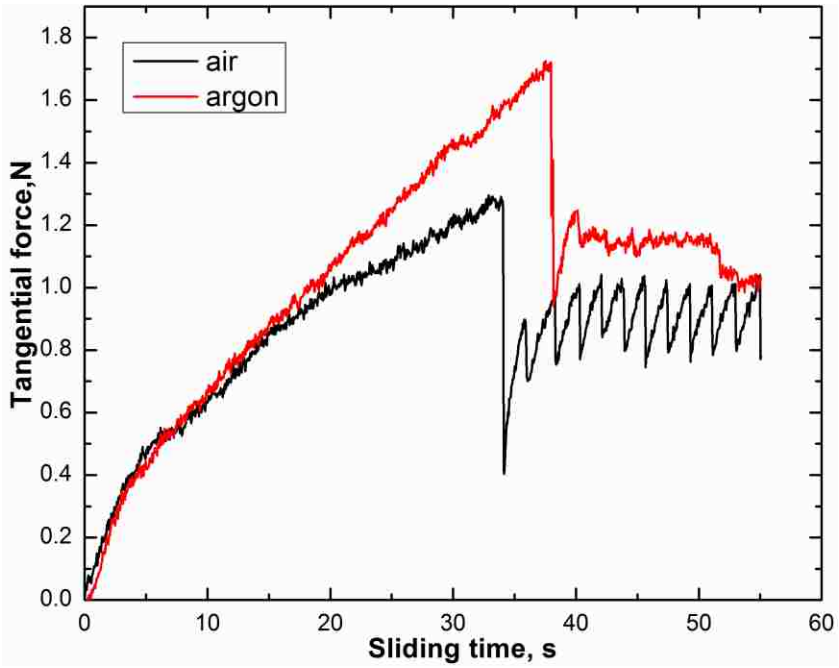

(a)

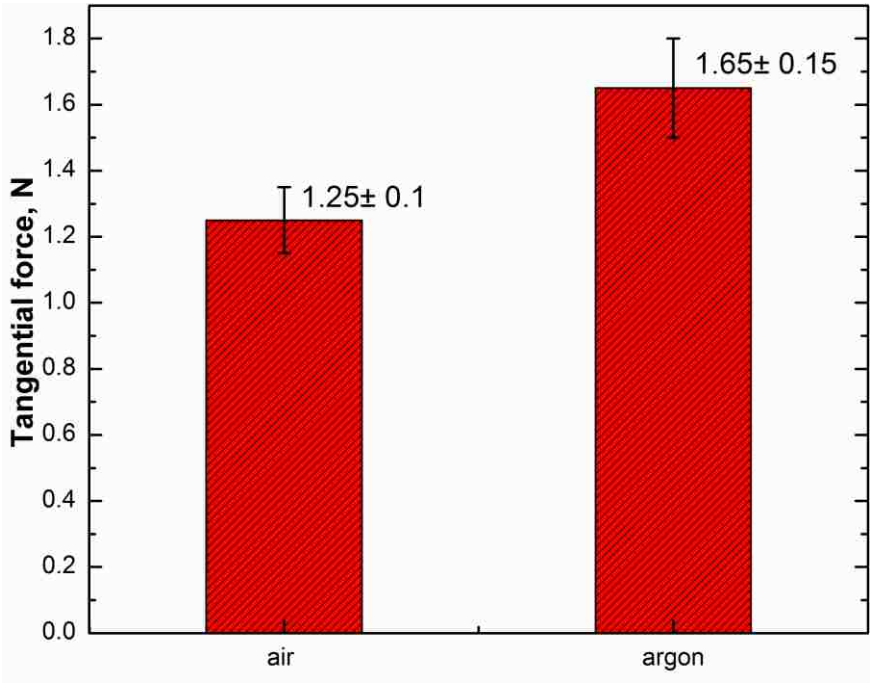

(b)

Figure 4.41 (a) The typical curve of tangential forces versus time for AA6061 tested in air and argon. (b) Average values of junction strength for AA6061 in air and argon (maximum tangential stress reached before the failure of adhesive junction).

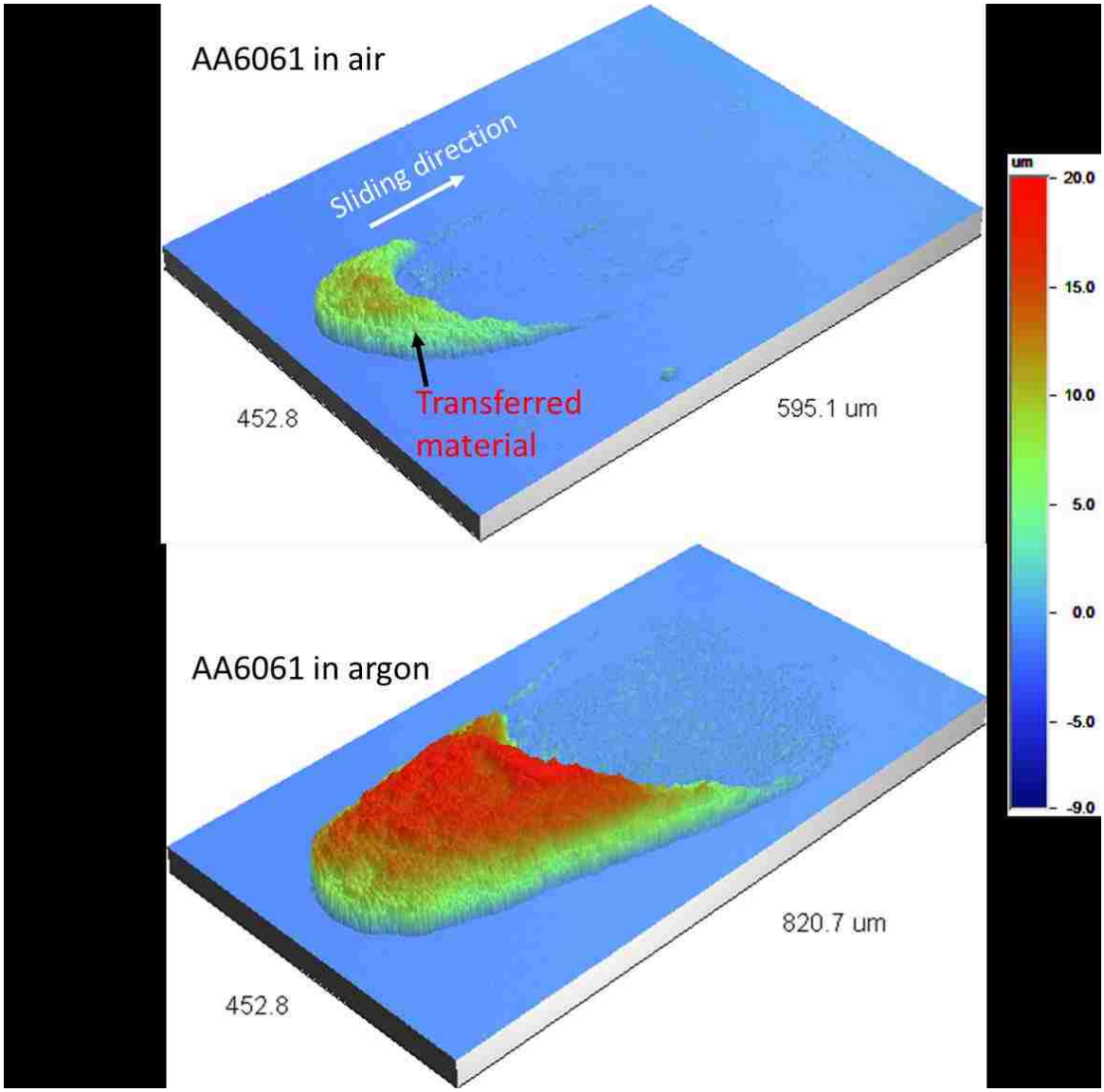

Figure 4.42 3-D profilometry images of the adhered material on the steel counterface surfaces tested against AA6061 alloys in (a) air, (b) argon

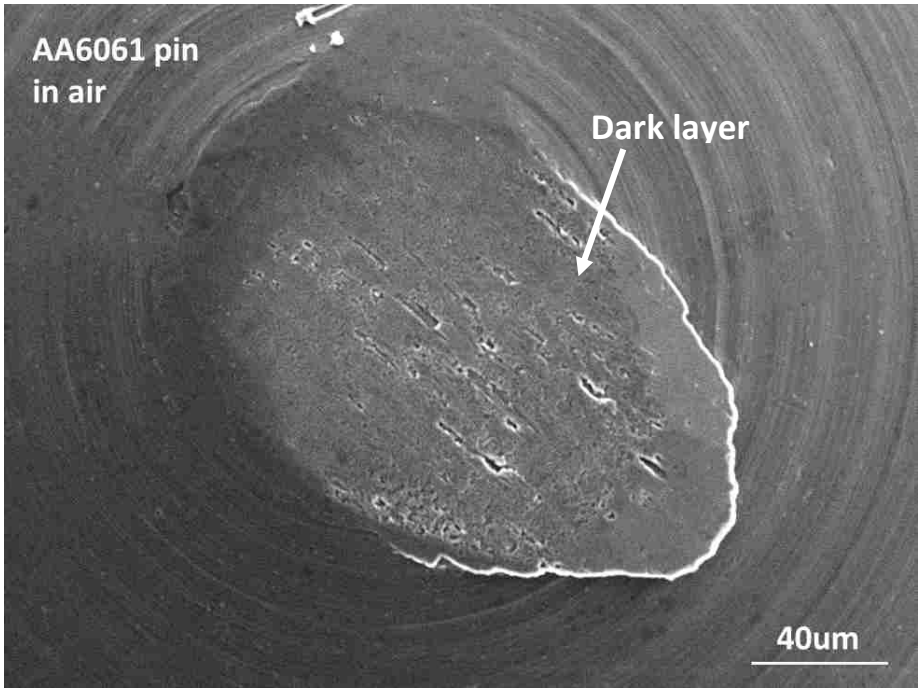

(a)

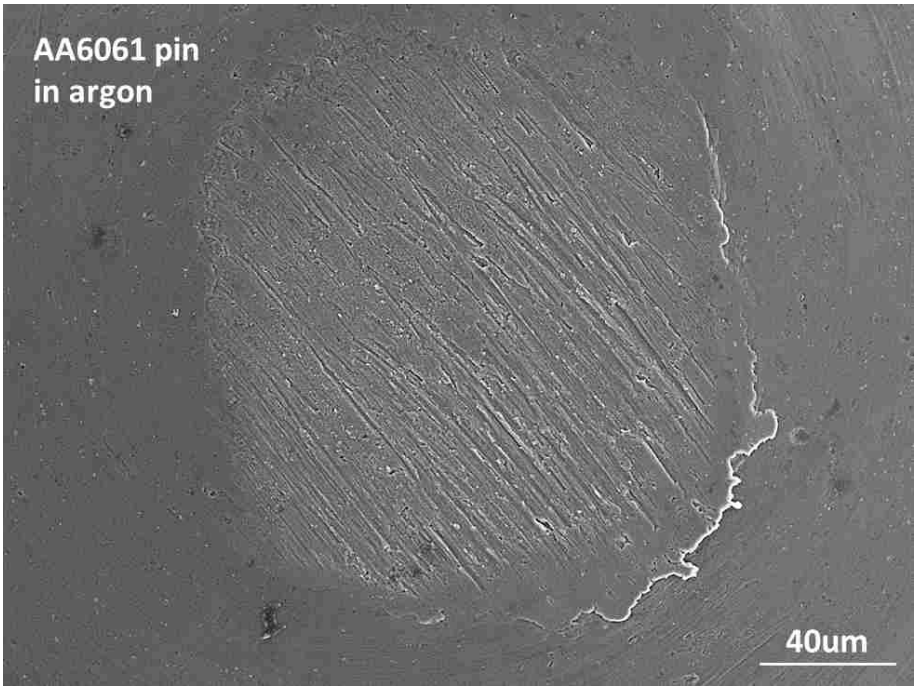

(b)

Figure 4.43 Secondary electron images showing the surface morphology of AA6061 pin deformed at 420^{o}C: (a) in air (b) in argon

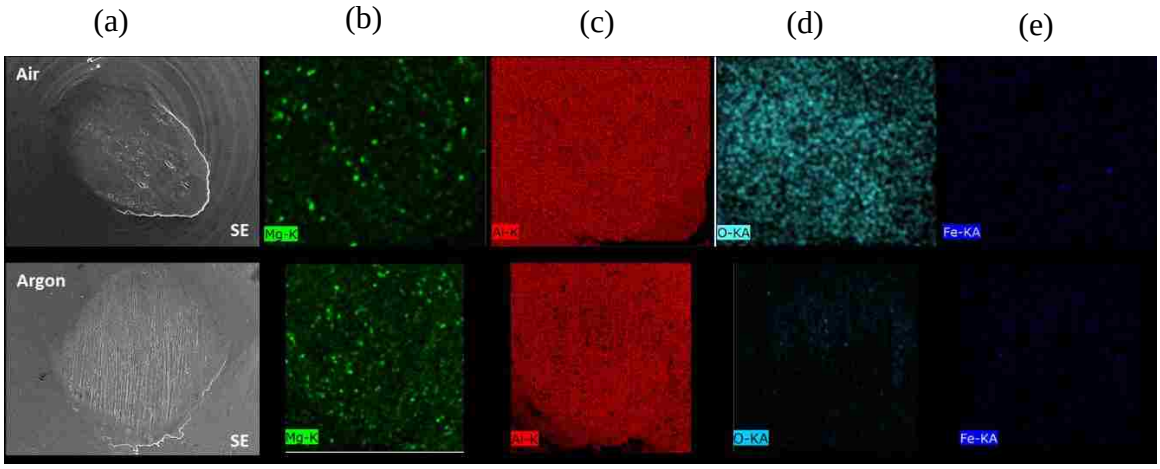

Figure 4.44 EDS maps of the elements, Al, Mg, Fe, O, found on the contact areas on AA6061 alloy surface after testing against with counterface in air and argon. The images on the column (a) are the SE images of the same areas for each alloy tested, column (b) (c) (d) (e) are element maps of Mg, Al, O, Fe.

CHAPTER 5: DISCUSSION

5.1 Introduction

In the previous chapter, the role of temperature and strain rate on friction behaviour of AA6061 alloy was studied by performing the friction test using hot-forming simulator and a COF map as well as a deformation mechanism map were constructed. The plastic deformation and surface damage mechanisms were identified and their relationship to the tribological behaviour of AA6061 alloy was established.

In this chapter, a discussion of the deformation mechanisms which operate at elevated temperatures, and how they influence the COF is provided. Accordingly, **Section 5.2** discusses the relationship between the COF of AA6061 alloy and its deformation behaviour. Also a discussion of the surface damage caused by the deformation at high temperature is given. **Section 5.3** provides a discussion of surface microstructures and morphologies of the deformed AA6061 in air and argon. **Section 5.4** focuses on the interpretation of the higher COF values obtained in argon in comparison with those obtained in air. **Section 5.5** discusses the adhesive metallic junction strength of the interface generated at the first contact between the working material and counterface.

5.2 Relationship between COF and deformation mechanisms

The dominant deformation mechanisms at various temperatures and strain rates were shown on a deformation mechanism map (DMM) **Figure 4.19**. It is important to use DMM to rationalize the friction behaviour at elevated temperatures. By analyzing the COF values simultaneously with the deformation mechanisms, a combined COF-deformation map (COF-DMM) was established as shown in **Figure 5.1**. This map combines COF contours plotted together with the deformation mechanism regimes and it indicates the

effect of the different deformation mechanisms on COF values. Accordingly, dislocation creep acts as the dominant mechanism in the narrow temperature and strain rate region, and where the COF is comparatively low, varying between 1.9 and 2.0. Deformation by power law creep (dislocation creep) does not induce the roughening of the strip surface to the same extent as GBS, which is evident from the comparison of the surface roughness (R_a) values (**Table 4.1**), and SEM images in **Figure 5.2**. The SEM images indicate that at 350^{o}C and 0.04s^{-1} (dislocation creep occurs) GBS is impeded when power law creep occurs. In addition, the highest flow stress of the alloy occurs in the dislocation creep controlled region (**Figure 4.17d**).

Diffusional flow mechanism covers all the temperature range at low strain rate, the COF increases from 1.73 (350 ^{o}C and 0.01 s^{-1}) to 1.94 (545 ^{o}C and 0.01 s^{-1}). Diffusional flow is also not expected to promote surface roughening, and the surface roughness values measured vary between 0.61μm (350 ^{o}C and 0.01 s^{-1}) and 0.74 μm (545 ^{o}C and 0.01 s^{-1}) (**Table 4.1**). The softening of the alloy as its flow stress decreases from 34.2 MPa (350 ^{o}C and 0.01 s^{-1}) to 3.4 MPa (545 ^{o}C and 0.01 s^{-1}) (**Figure 4.17d**) leads to the increase in COF in this region.

The GBS deformation mechanism operates at the widest temperature and strain rate range in the COF-DMM map (**Figure 5. 1**) and the COF value in this regime was as low as 1.85 (350^{o}C and 0.02s^{-1} – 0.25s^{-1}) up to 2.2 (545^{o}C and 0.04s^{-1}). GBS is responsible for the high surface roughness values due to the formation of the grain boundary steps on the surface see **Figure 4.21**. The surface grain topography could be distinctly observed using optical interferometry (**Figures 5.3a to d**). The average grain step height against strain rate is plotted in **Figure 5.4**, according to **Figure 5.4** an increase in the strain rate increased the

average grain boundary step height on the free surface. In addition, the experimental conditions shown in **Figure 5.3b to d** belong to high temperature and strain rate from $0.02s^{-1}$ to $0.04s^{-1}$. This is the regime that is operated by the GBS (see **Figure 4.21**). The grain steps increase due to grain boundary sliding and induce the surface roughening, and consequently high COF values are observed at the GBS regime.

A quantification of the grain boundary step height is provided by performing a statistical analysis at each temperature and strain rate. As shown in **Figure 5.5**, COF values are plotted against the grain boundary step heights divided by the flow stress. The data points in the plot are fitted by a red dashed line which reveals a linear relationship between the COF and the combination of step height and flow stress. In the other words, the COF in AA6061 alloy is a function of grain boundary step (or surface roughness) and flow stress of deformation. In summary, GBS increased with increasing temperature and strain rate, resulting in a higher surface roughness, and higher COF, due to the grain steps formed on at the grain boundaries on the surface.

5.3 Surface microstructure and morphology of the deformed alloy

In **Section 5.2** the temperature and strain rate dependence of COF has been discussed for AA6061 alloy. Also, a relationship between the deformation mechanisms and COF has been established. This section presents the effect of surface microstructure and morphology of the work piece deformed in air and argon atmosphere on COF.

5.3.1 Surface oxide damage mechanisms and oxide fibres formation in AA6061 alloy at 350 – 545ºC in air

In this section the surface damage mechanisms that operate in the oxide layer, which covered the AA6061 alloy's surface during the plastic deformation in the 350 – 545ºC range are discussed. Oxide ligaments, which have a thin fibrous structure were observed on samples that were underwent plastic deformation, especially at high temperatures and strain rates. Usually oxide fibres were between 1- 3 μm long and were elongated with a diameter of 146 ± 28nm without necking. The high length-to-diameter ratios (19 calculated the fibres formed in AA6061) of fibres indicated that superplastic deformation occurred during the formation of these fibres at 545ºC and $0.04s^{-1}$. These fibres were directly formed from the oxide layer on the material rather than the bulk alloy, and the fraction of surface covered by the fibres was calculated, which is 17%. This value is smaller than the reported value (42%) from Das [62] on 4.5% Mg alloy (AA5083) at the same experimental conditions. This is because the formation of the fibre at the grain boundaries in air needs sufficient Mg and GBS, for AA6061 (1.2% Mg) with grain size of 20 ± 3.4μm is larger than the grain size (5 ± 2.5μm) of AA5083 (4.5% Mg). Less GBS occurs on AA6061 than AA5083, and less diffused Mg on the surface facilitate the oxide fibres' formation.

A clarification is needed to distinguish between the plastic deformation of the bulk alloy and the deformation of the oxide layer. In the as received condition, the tribolayer covers the bulk material surface, and by applying a strain at high temperature GBS occurs. Due to GBS, surface offsets form, and application of plastic strain to the oxides causes stretching of the tribolayer over these sliding grain boundaries. In the presence of oxygen, the oxide is subjected to superplastic deformation at those locations, resulting in long oxide fibre formation (2.8 ± 0.39 μm). The length of the fibres was almost equal to the grain

boundary steps. As **Figure 4.11** shows, the length of the fibres increased with the increase in temperature at high strain rate. This is expected because GBS in the AA6061 alloys become more predominant at high temperatures and strain rates.

The oxide layer shows less ductile behaviour when T < 450 ^{o}C and strain rate higher than 0.03 s^{-1}. In this case, oxide layers fractured and few fibres could be observed. Oxide fibres are not expected to form at the grain boundaries because this mechanism did not lead to form the surface offsets. From another point of view, at low strain rates (for all test temperatures) the deformation mechanism is controlled by diffusional flow (with stress exponent n=1), and the surface roughness is low without any grain offset. In summary, large elongations stretching oxide fibres are caused by the GBS of the surface grains of the AA6061 alloy.

Two types of oxide damage features and oxide fibre formation that occurred in an air atmosphere are illustrated in **Figures 5.6 and 5.7**. According to **Figure 5.6**, cracks were formed in the tribolayer and some oxide fibres bridged the crack with a small amount of elongation (length-to-diameter ratio is 5.2), and some fibres fractured. This type of damage can be observed at temperatures below 450^{o}C and high strain rates. In **Figure 5.7**, superplastic oxide fibres were triggered by surface offsets due to GBS, where the fibres were observed to stretch across the edges of the crack without breaking. This type of damage can be observed at 545^{o}C and a high strain rate.

5.3.2 Surface oxide damage features and oxide fibres formation in AA6061 alloy at 350 – 545^{o}C in argon.

The surface oxide damage mechanisms in AA6061 alloy tested between 350 – 545^{o}C in air have been discussed in the previous section, which showed that considerable

amount of superplastic oxide fibres (oxide fibres covered an area up to 17%) formed in air. In addition, AA6061 alloy exhibited different friction behaviour in air and argon as was presented in **chapter 4**. In order to better understand the effect of the atmosphere on surface damage behaviour of AA6061 alloy, this section presents a general discussion which focuses on surface damage features and oxide fibres observation in the oxide layer which covered on the AA6061 alloy during the plastic deformation in the 350 – 545ºC range and at 0.04 s^{-1} in argon atmosphere.

No oxide fibre can be observed on samples that underwent plastic deformation in the 350 – 545ºC range and 0.04 s^{-1} in argon atmosphere. The difference has been clarified between the plastic deformation of the bulk alloy and the deformation of oxide layer. Thus, the DMM established in air atmosphere is still valid in argon atmosphere. Under the as received condition, the oxide layer covers on the bulk material surface, and GBS occurs when applying a strain at high temperature. Although high temperature and the initiation of GBS will facilitate the diffusion of Mg to the free surface, in the absence of oxygen the diffused Mg on the free surface cannot form fibre-like oxide under the applied plastic strain.

The oxide layer also shows less ductile behaviour in argon gas when T < 450 ºC and strain rate higher than 0.03 s^{-1}, oxide layer fractured and no fibre can be observed in the cracks. Oxide fibres are not expected to form at the grain boundaries because (i) the experimental conditions are not conductive to forming surface offsets (ii) in the absence of oxygen the diffused Mg on the free surface cannot form fibre-like oxide under the applied plastic strain.

Two types of oxide damage features in argon are illustrated in **Figures 5.8 and 5.9**. In **Figure 5.8**, cracks formed in the tribolayer and no oxide fibre formed in the crack. This

type of damage can be observed at temperatures below 450^{o}C and at high strain rates. In **Figure 5.9**, surface offset triggered by GBS, however, no oxide fibre formation occurs in argon. This type of damage can be observed at 545^{o}C and high strain rate.

5.4 Variation of COF in air and argon

5.4.1 Friction test with tribolayer in air and argon.

The effect of atmosphere on the surface damage features of AA6061 alloy has been discussed in **Section 5.3**. By the presence of oxygen, for the sample covered by the oxide layer, considerable oxide fibres can be observed on the surface when GBS is the dominant deformation mechanism. While, by the absence of oxygen (in argon), no fibre can be detected on the worn surface. The atmosphere plays an important role on the oxide formation and surface damage mechanism. In order to study the effect of atmosphere on the friction behaviour of AA6061alloy, the friction experiments were performed in air and argon respectively at 0.04s^{-1} and temperature from 350^{o}C to 545^{o}C for polished and as-received samples.

The average COF values of as-received strip in air and argon are plotted against different temperatures in **Figure 4.23**. Under the present experimental condition, the COF value increased with temperature at the constant strain rate of 4×10^{-2} s^{-1} in air and argon, and the mean COF value measured in argon environment at each temperature was higher than that in air. As mentioned before, the atmosphere plays an important role on the oxide behaviour, thus an analysis which focus on the wear track is necessary. **Figure 5.10** presents the secondary electron images of sliding track induced on unpolished AA6061 alloy at 545^{o}C 0.04s^{-1} in air and argon. At the present experimental conditions, the displacement of plastically deformed material was observed to form shingle-like features

inside the sliding track in air and argon atmosphere. In addition, no oxide fibres formation was observed within the sliding track in all conditions. EDS map of the worn surfaces which include the sliding track is shown in **Figure 5.11**. The selected mapping area covers the sliding track and the part outside sliding track, aluminum, magnesium and oxygen can be detected in the selected area in air. While, less magnesium and few oxygen can be detected in argon, especially in the sliding track, oxides observed in the mapping area was due to the existing tribolayer. In the other word, within the sliding track, no fresh oxide formation during the P20 steel pin sliding against the strip surface. In this situation, more metal to metal contact between the pin and strip due to no fresh oxide layer formed between the pin and strip surface. And it is consistent with the higher COF value observed in **Figure 4.23**.

5.4.2 Effect of surface condition on friction behaviour in air

The surface condition of AA6061 alloy during elevated temperature sliding contact deformation also influences the friction between the alloy and the steel die. **In Air**, the average COF measured on the polished sample is higher than that of unpolished sample. This is due to the formation of the tribolayers on the surface of the alloy during the prior deformation processes appears to be an advantage in reducing friction and adhesion, and the removal of tribolayers generated during hot rolling from the surface could be attributed to the formation of stronger adhesive force. The morphology of the material adhesion to the P20 pin displayed in **Figure 5.12**, that is another clew which could interpret the difference in COF values of the polished and traibolayer covered samples. The morphology of the material transferred to P20 pin from the unpolished strip was discontinuously distributed over a wide area, while material adhesion from to pin to the polished strip was localised and continuous, and it can be described as a stick-slip when a polished surface comes into sliding contact with the counterface the adhesion force are higher (the adhesion

force will be discussed in **Section 5.5**), this would suggest that the surface condition would in turn affect the COF. A detail should be noticed on the morphology of the adhered area of the polished surface, the red dash circles marked on the 3D profiles indicated the initial contact area on the pin, and it increases with temperature. This increase would increase the COF of the polished surface compared with the tribolayer covered surface.

5.4.3 Friction test without tribolayer in air and argon.

The friction tests on polished strips performed in argon atmosphere at the constant strain rate of 4×10^{-2} s^{-1} in have been described in **Section 4.7**. The similar COF trend is observed, which the COF value increased with temperature at the constant strain rate of 4×10^{-2} s^{-1} in air and argon, and the mean COF value measured in argon environment at each temperature was higher than that in air. An average COF of 2.67 ± 0.01, which is the highest COF value was measured under present experimental conditions. **Figure 5.13** presents the secondary electron images of sliding track induced on polished AA6061 alloy at 545^{o}C 0.04s^{-1} in air and argon. At the present experimental conditions, the displacement of plastically deformed material is more severe than the tribolayer covered sample, and more shingle-like features inside the sliding track is observed in air and argon atmosphere under polished condition.

In addition, no oxide fibres formation can be observed within the sliding track in all conditions. EDS map of the worn surfaces which include the sliding track is shown in **Figure 5.14**. The selected mapping area covers the sliding track and the part outside sliding track. In air, less magnesium and oxygen occurs outside the wear due to the removal of the oxide layer before the test compared with the tribolayer covered sample in **Figure 5.11**. A detail should be noticed within the wear track as shown in **Figure 5.14**. Although the

tribolayer has been removed before the sliding tests, the oxides still can be detected in the sliding track in air and this is due to the Al and diffused Mg reacted with the oxygen in the ambient. While, no oxygen can be detected in the sliding track in argon, in the other word, within the sliding track, no oxide formation during the P20 steel pin sliding against the strip surface. In this situation, metal to metal contact between the pin and strip due to no oxide layer formed between the pin and strip surface. By the absence of the oxide layer acts as the solid lubrication in argon, and the higher adhesion force occurred between the polished surface and counterface, the highest COF is generated at this experimental conditions.

5.5 Adhesion and surface oxidation in junction strength tests

In previous sections (**Section 5.2** and **5.3**) the temperature and strain rate dependence of COF was discussed for AA6061 in both air and argon. Also, a relation between the mechanisms of deformation and COF was established. Accordingly, in order to understand the localized junction formation due to material adhesion and transfer during the sliding experiments, junction strength tests of AA6061 were performed in air and argon atmospheres to study the effect of atmosphere on junction strength. In addition to AA6061, the adhesion behaviour of oxides formed by using alloys with increasing Mg content were also investigated. This section discusses the adhesion of material to the counterface in different atmospheres (air and argon), the characteristic features developed on both of the counterface and the alloys' surfaces and how these surface oxides affect the adhesion and friction.

5.5.1 Effect of Mg content on adhesion and surface oxidation

It was observed that the junction strength decreased with the increase in Mg content in the Al-Mg alloys against steel counterface when tested in air. The contact areas on the

steel counterface were analyzed using EDS, and for alloys containing lower amounts of Mg also contained less oxygen, therefore MgO formation was not observed for AA1100 (0% Mg). Considering the Mg and O-maps of AA6061, AA5083 and AZ91 shown in **Figure.4.38**, oxide rich layers formed on these alloys. **Figure.4.40** provides the evidence from the deformed alloys' surface, for AZ91, the main oxide covered on the deformed surface is MgO; for AA5083 and AA6061 alloys, MgO and Al_xO_y were observed on the alloys surface; for AA1100, the oxides occur in the form of Al_xO_y rather than MgO. The existence of a magnesium-rich surface oxide reduced the junction strength, and accordingly, the maximum height and area of the material transferred to the counterface decreased with the increase in Mg content.

5.5.2 Effect of atmosphere on adhesion and surface oxidation

Experiments using the hot-forming simulator showed lower COF in air for AA6061 than that in an argon atmosphere under the same homologous deformation temperature. The junction strength experiments conducted on AA6061 in air and argon atmospheres confirmed that the junction strength of AA6061 in air is lower than the junction strength in argon and the generated tangential force after the first junction broke in argon (average 1.2N) was higher than that in air (average 0.8N) as in **Figure 4.41**. In addition, the area covered with the transferred material in argon is larger than that in air, the same phenomenon was also observed in the hot forming test in argon atmosphere.

EDS elemental maps taken from the contact surfaces of the alloy after each test shown in **Figure.4.44.** It was observed that the contact areas for AA6061 deformed in argon contained less (negligible) oxygen than that in air, therefore oxide formation was not observed for AA6061 in argon atmosphere. In the absence of the oxide layer formation,

more metal to metal contact between the alloy and the steel couterface, consequently, result in higher junction strength, higher tangential force after the first junction broke, and more material transferred to steel counterface.

In summary, the surface of AA1100, AA6061, AA5083, and AZ91 alloys that produce the contact interface with the die surface were covered with a layer of oxide in air atmosphere. The alloy with high magnesium content provides magnesium rich oxides to reduce the material transfer and COF. The junction strength and the material transfer of AA6061 in argon is higher than that measured in air due the absence of Mg oxide layer on the surface of the alloy. This is consistent with the higher COF values obtained in argon.

The current study examines the tribological behaviour of AA6061 alloy sheets at elevated temperatures including a study of the deformation mechanisms and their effects on friction behaviour. The role of the atmosphere is given particular importance when studying the surface morphology and that developed during high temperature deformation. Sliding contact experiments were performed using a hot forming simulator with an operating temperature range of 350 to 545°C, using strain rates between $1x10^{-2}$ and $4x10^{-2}s^{-1}$. The coefficient of friction (COF) of AA6061 alloy was measured during plastic deformation by considering the simultaneous effects of temperature and strain rate both in air and argon atmosphere. The measured COF in argon was higher than that in air due to the absence of fresh oxide layer formed inside the sliding track. The effect of the tribolayer on the hot forming process was identified by studying the variation of the COF and the characteristic of material transfer on the pin. In order to study the localized junction formation due to material adhesion and transfer, the junction strength i.e., tangential force required to break adhesive metallic junction was measured in air and argon for the AA6061

alloy. The formation of oxides with increasing Mg content was also investigated using alloys with different Mg contents. These alloys consisted of AA1100, AA6061, AA5083 and AZ91. The junction strength of AA6061 in argon is higher than that measured in air as no oxide layer formed on the surface of alloy. EDS analyses provide good evidences to support this interpretation. Deformation mechanisms were identified for AA6061. Coefficient of friction-deformation mechanism map (COF-DMM) presented the relationship between the tribological behaviour and mechanisms controlling deformation. GBS induced high surface roughness, resulting in high COF. Therefore, this study on plastic deformation mechanism and surface damage, and their relation with tribological behaviour gave a better understanding of hot forming.

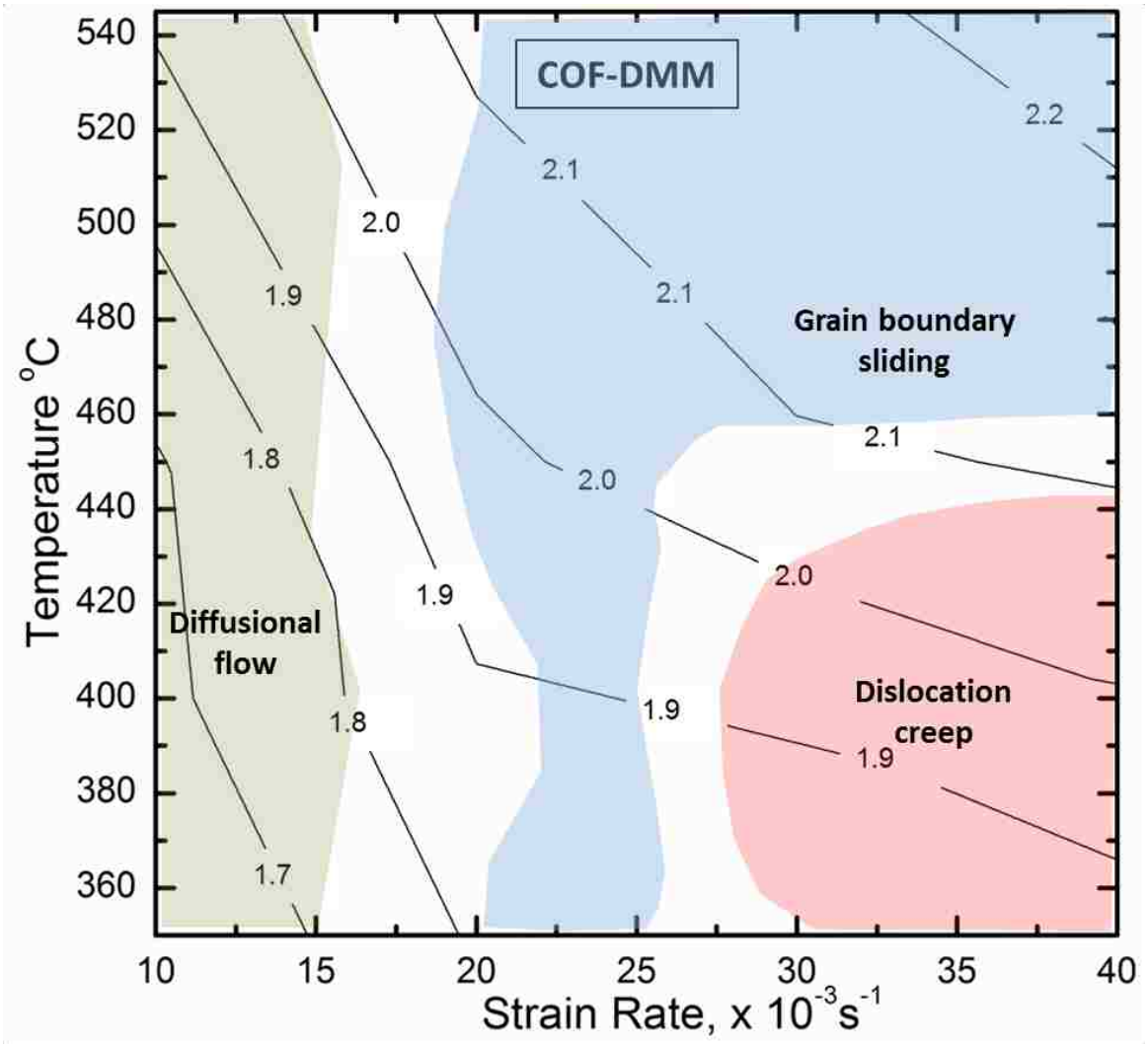

Figure 5.1 The combined coefficient of friction-deformation mechanism map (COF-DMM) for AA6061 alloy plotted on temperature vs. strain rate axes, where the COF values from Figure 4.3 are superimposed on the DMM from Figure 4.19. The contours represent iso-COF values.

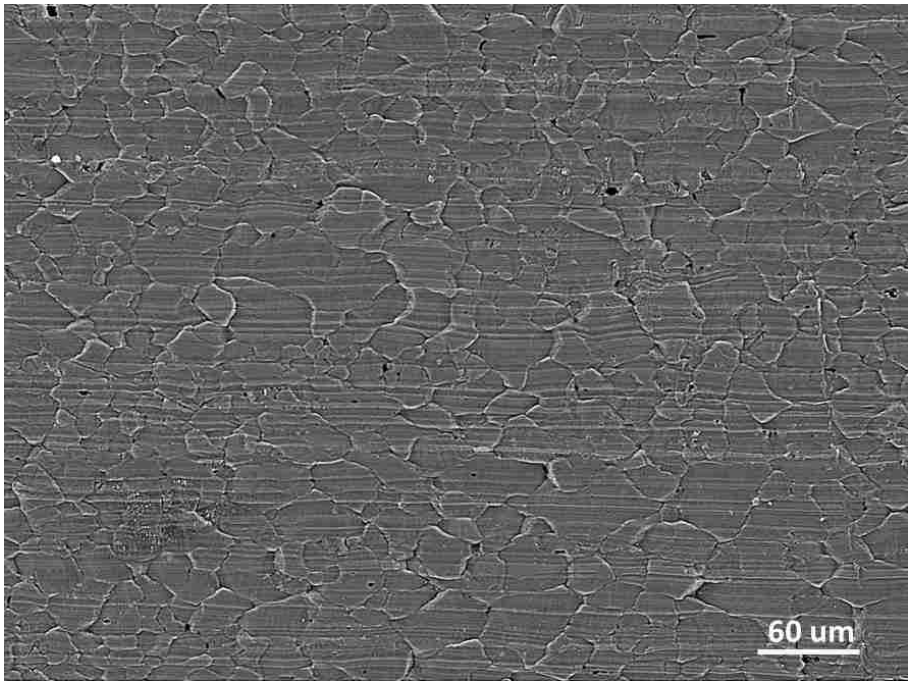

(a)

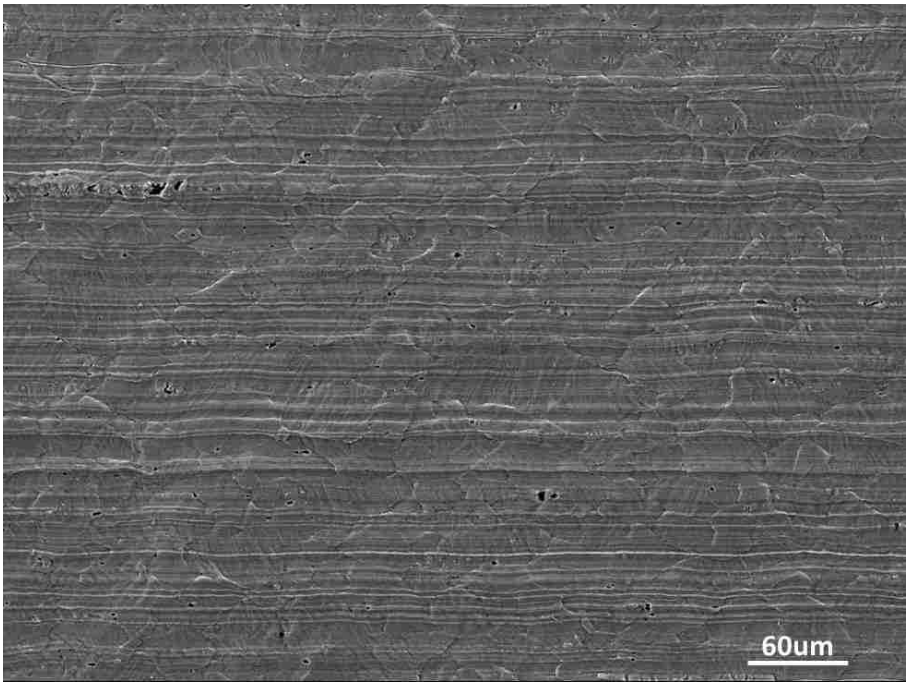

(b)

Figure 5.2 Secondary electron image showing the surface morphology of tribolayer covered AA6061 strip: (a) deformed at 545 °C and 4×10^{-2} s^{-1} GBS occurs (b) deformed at 350 °C and 4×10^{-2} s^{-1} power law creep occurs.

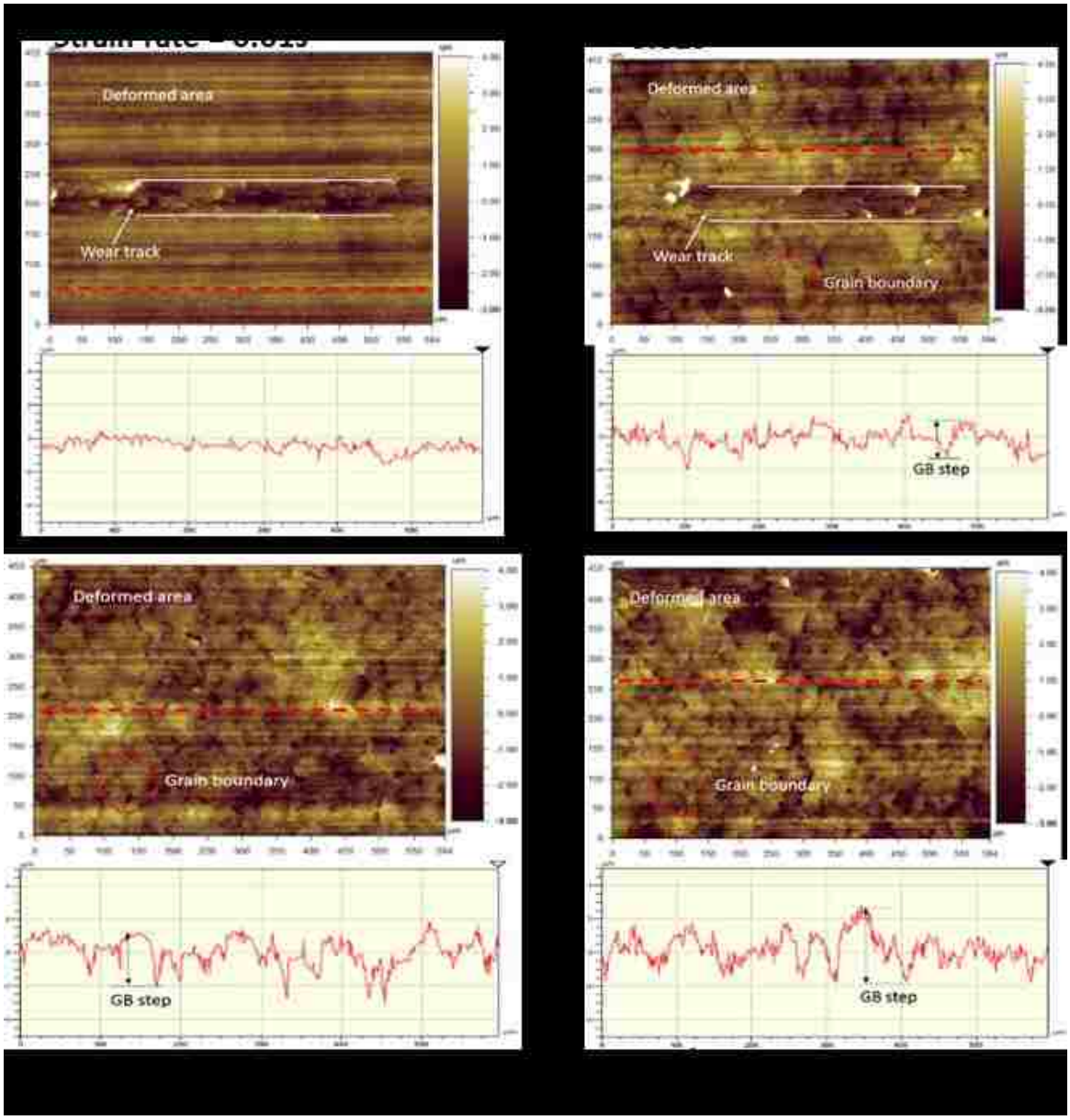

Figure 5.3 3-D optical surface interferometry profiles of the surfaces of AA6061 alloy strips deformed at 545 °C and (a) 1×10^{-2} s^{-1}, (b) 2 × 10-2 s-1 and (c) 3×10^{-2} s^{-1}; (d) 4×10^{-2} s^{-1} .The plots below the 3-D profiles are 2-D profiles that show grain boundary step heights on the strip surface. The dash line indicates the traverse length.

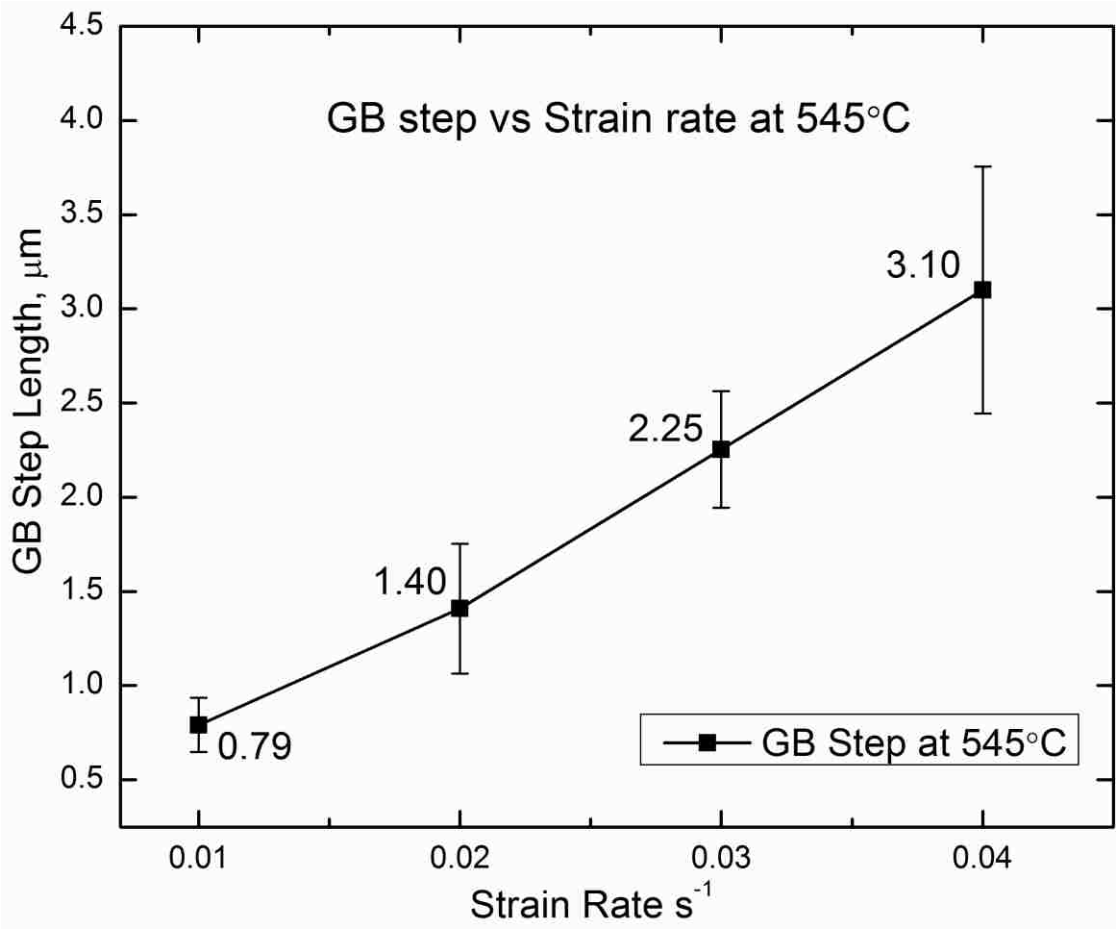

Figure 5.4 Variation of the step height against the against strain rate at 545ºC.

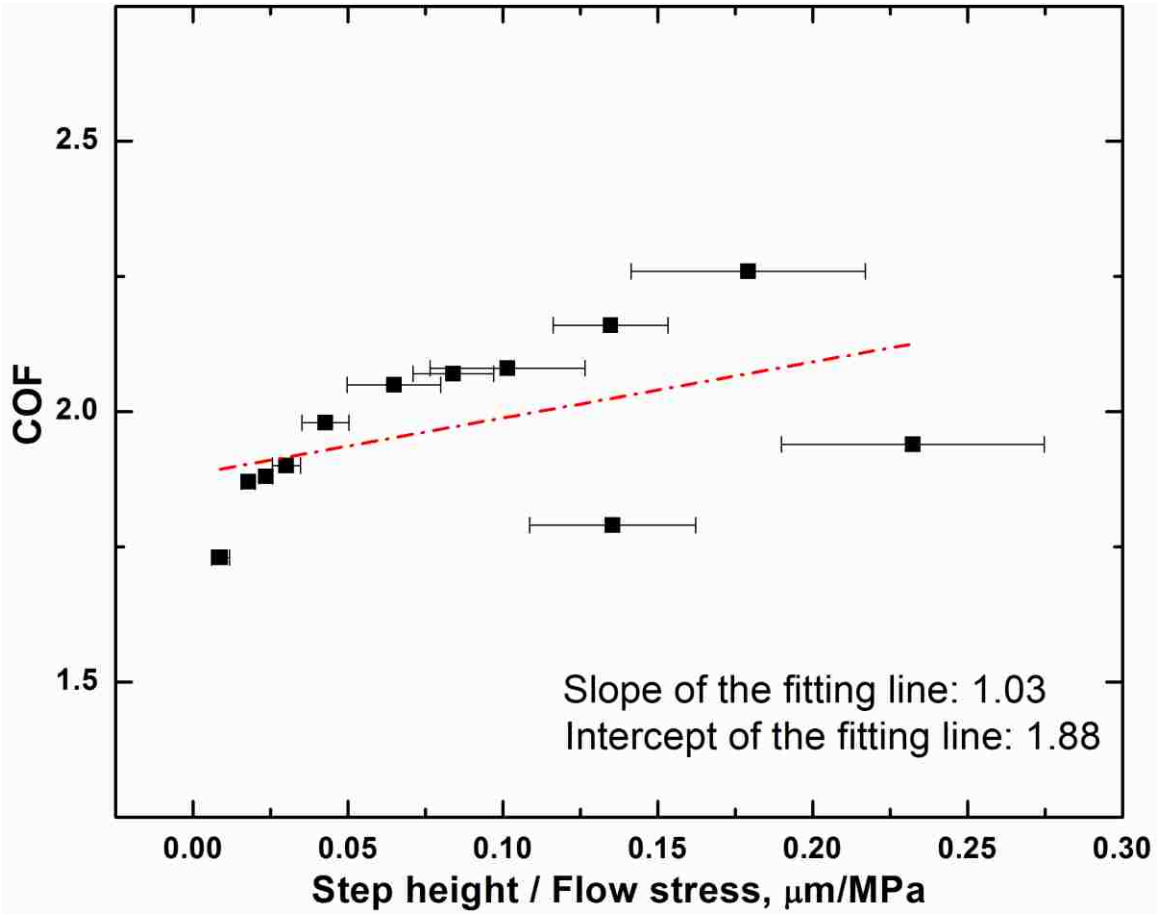

Figure 5.5 COF as a function of (step height/ flow stress) showing the combined effect of surface characteristics and mechanical behaviour on COF.

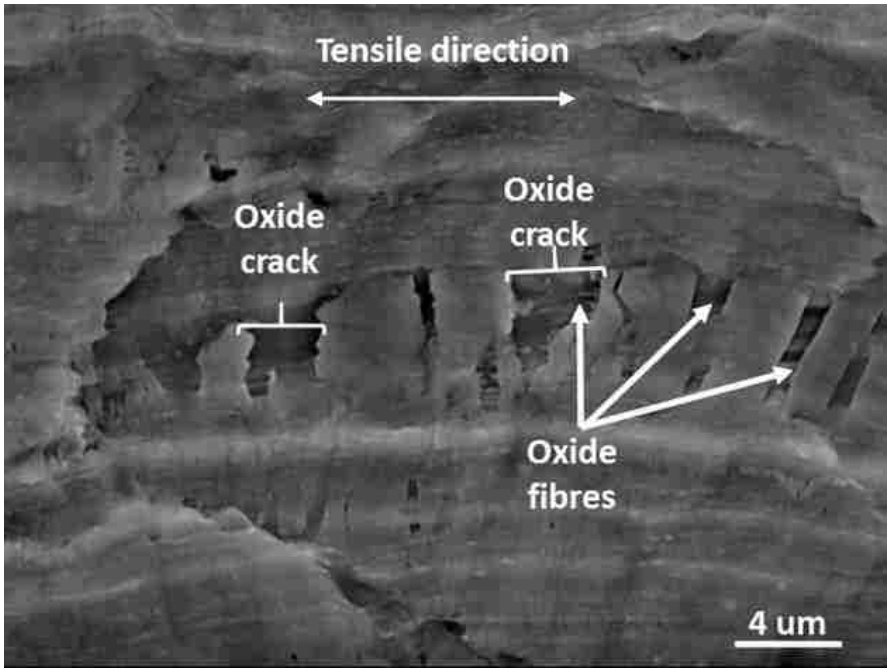

(a)

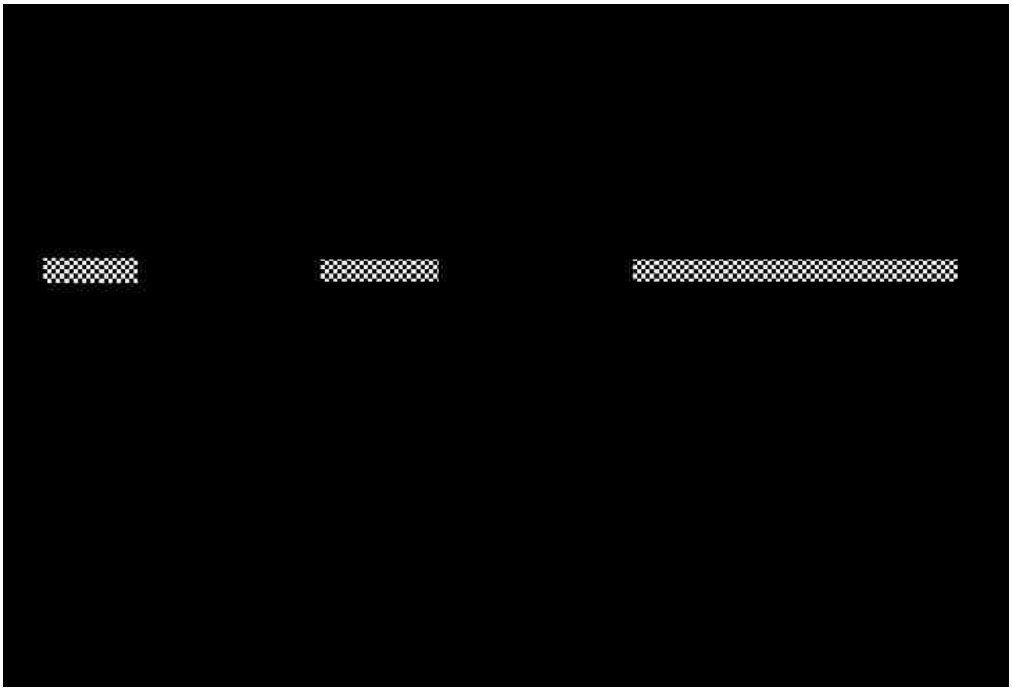

(b)

Figure 5.6 Crack formed on the oxide layer in air at 350^{o}C with fractured fibres (a) SEM observation on the oxide layer at 350 °C and (b) The schematic representation of surface damage features at 350 °C.

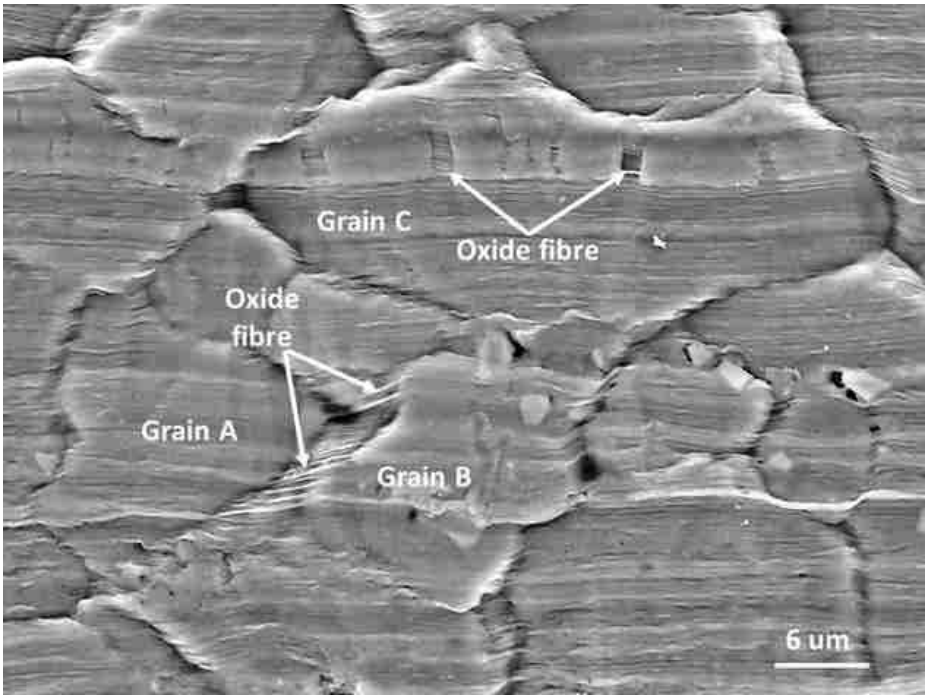

(a)

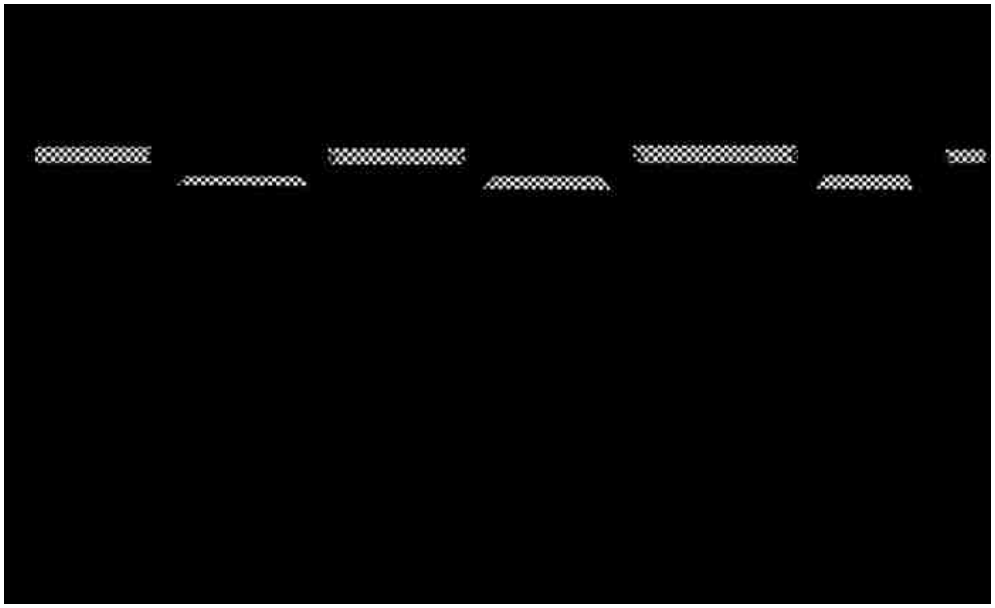

(b)

Figure 5.7 Superplastic oxide fibres triggered by surface offset due to GBS in air (a) SEM observation on the oxide layer at 545 °C and (b) The schematic representation of surface damage features at 545 °C.

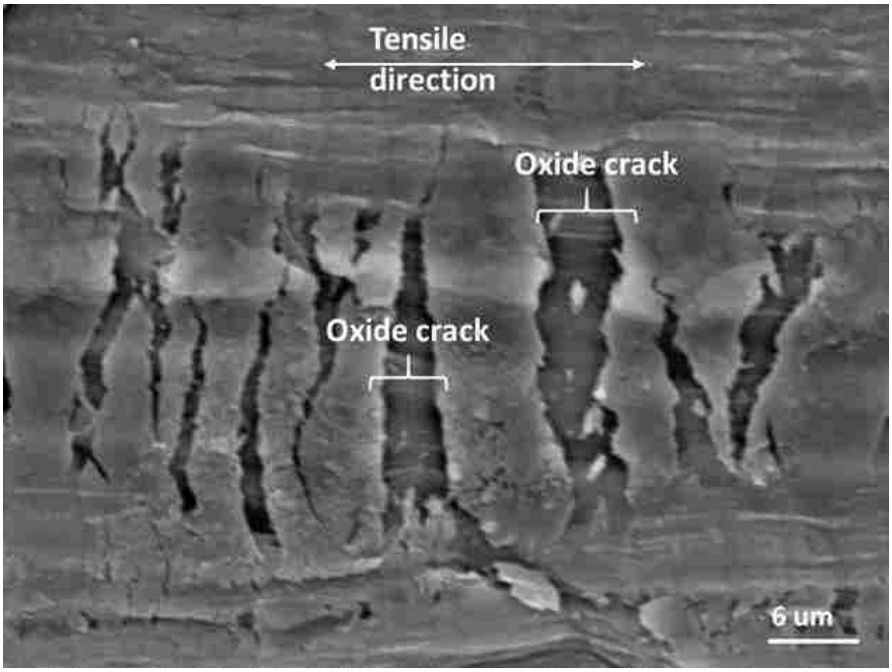

(a)

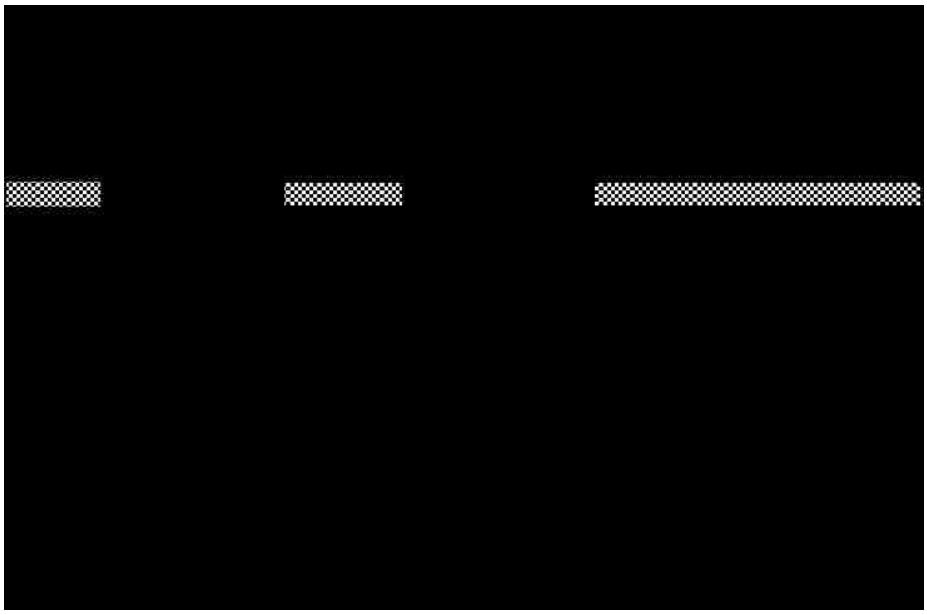

(b)

Figure 5.8 Crack formed on the oxide layer in argon at 350^{o}C with no fibre formation (a) SEM observation on the oxide layer at 350 °C and (b) The schematic representation of surface damage features at 350 °C.

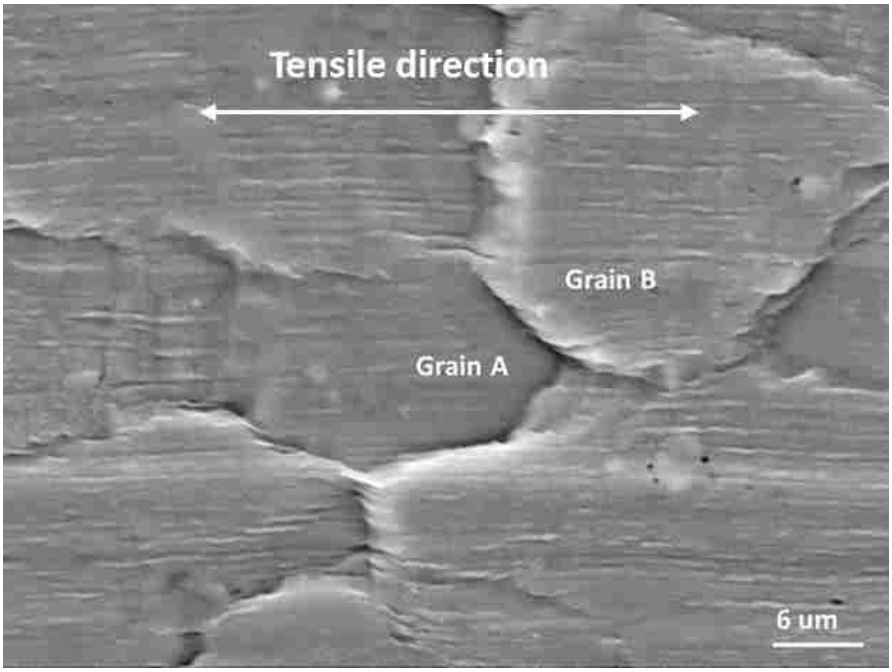

(a)

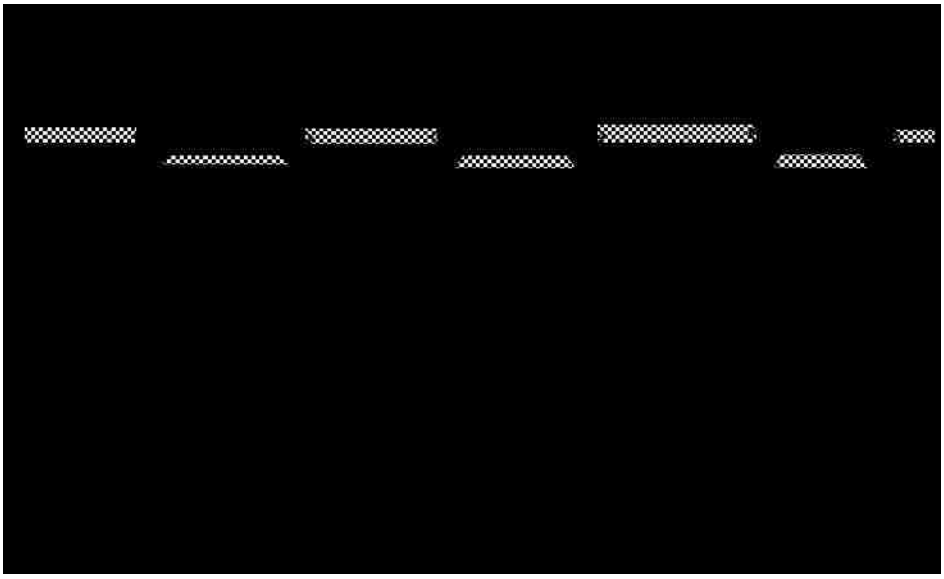

(b)

Figure 5.9 Surface offset due to GBS, however, no oxide fibre formation in argon (a) SEM observation on the oxide layer at 545 °C and (b) The schematic representation of surface damage features at 545 °C.

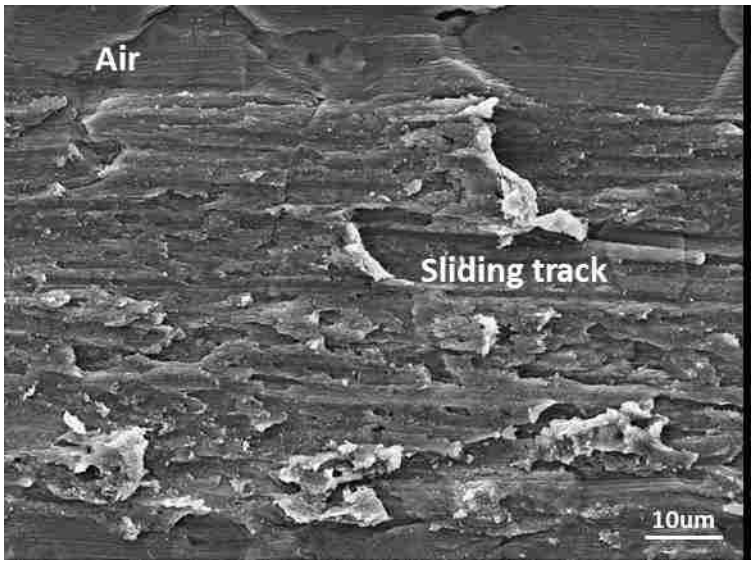

(a)

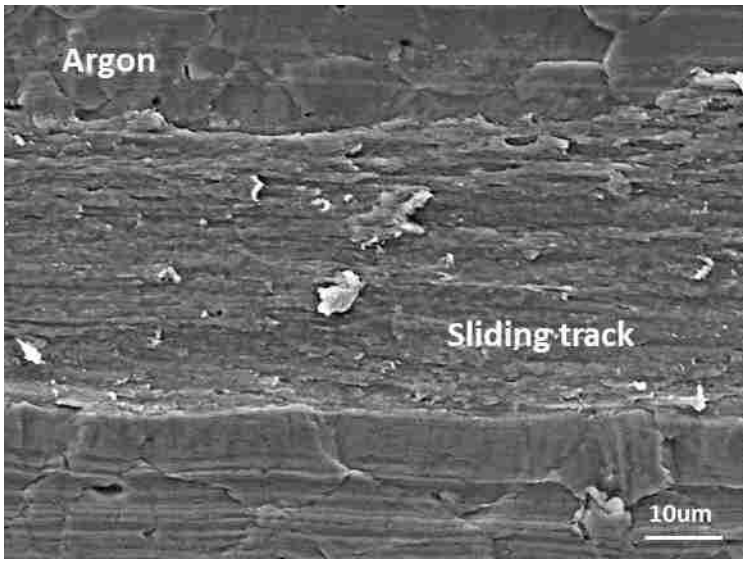

(b)

Figure 5.10 Secondary electron images of sliding track induced on unpolished AA6061 alloy at 545ºC 0.04s-^{1} (a) in air, (b) in argon

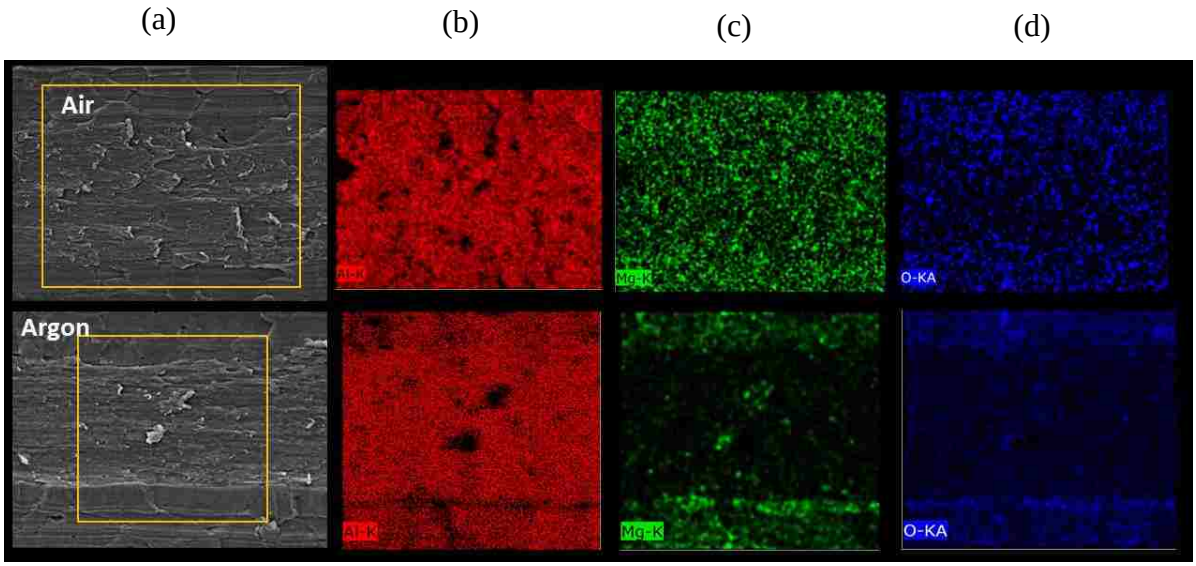

Figure 5.11 EDS maps of the elements, Al, Mg, O, found on the sliding track on as-received AA6061 alloy after testing against P20 steel pin in air and argon atmosphere. The images in column (a) are the SE images of the sliding track, column (b) (c) (d) are element maps of Al, Mg, O.

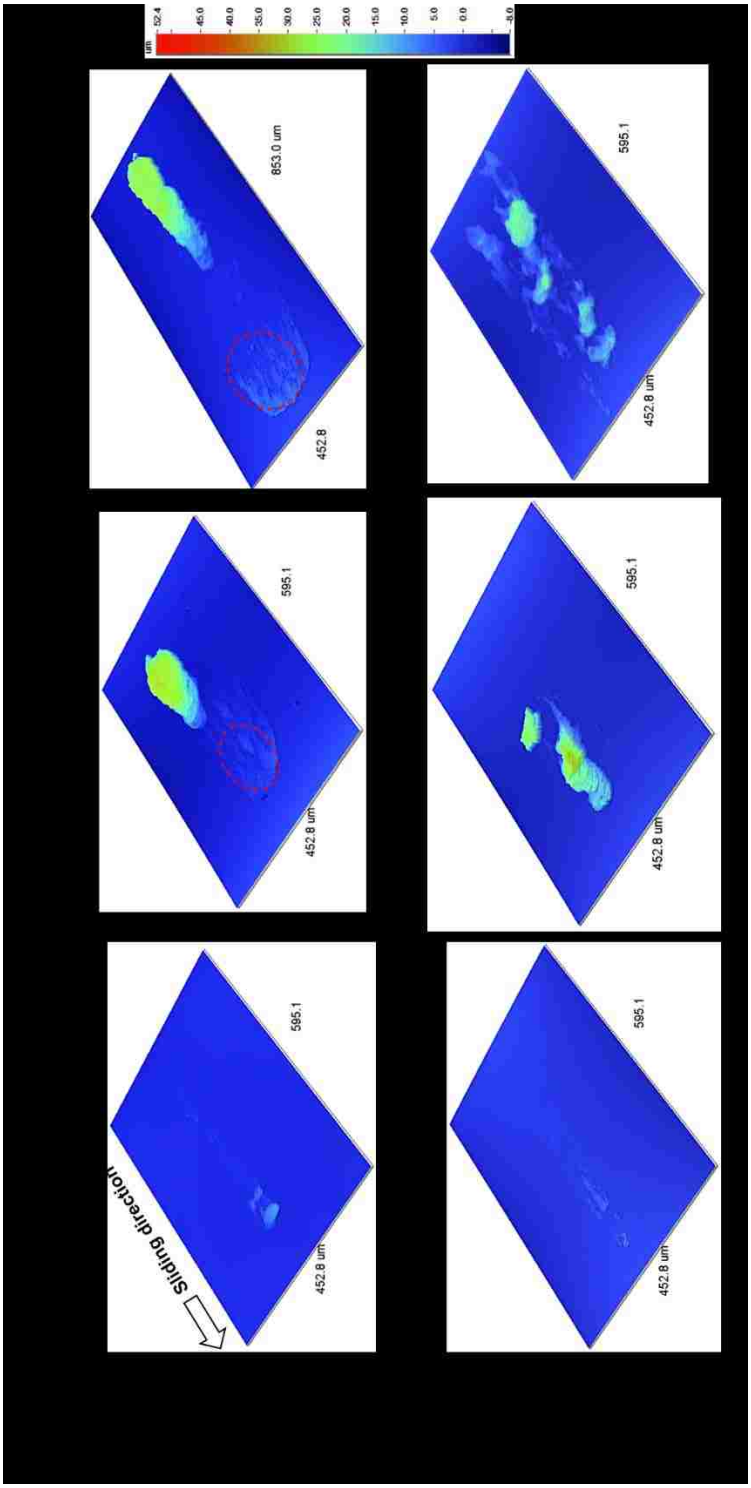

Figure 5.12 Comparison of 3-D profilometery images of material adhered to counterface P20 Pin while sliding against AA6061 strips in air with and without tribolayer.

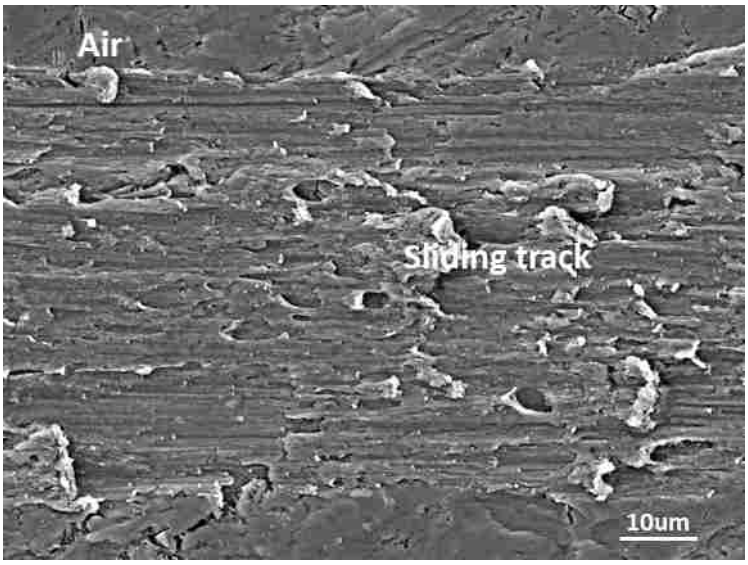

(a)

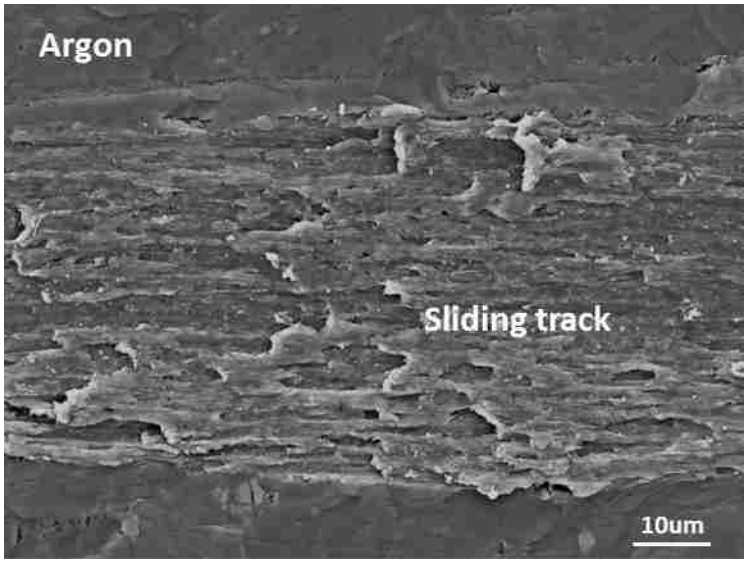

(b)

Figure 5.13 Secondary electron images of sliding track induced on polished AA6061 alloy at 545^{o}C 0.04s^{-1} (a) in air, (b) in argon

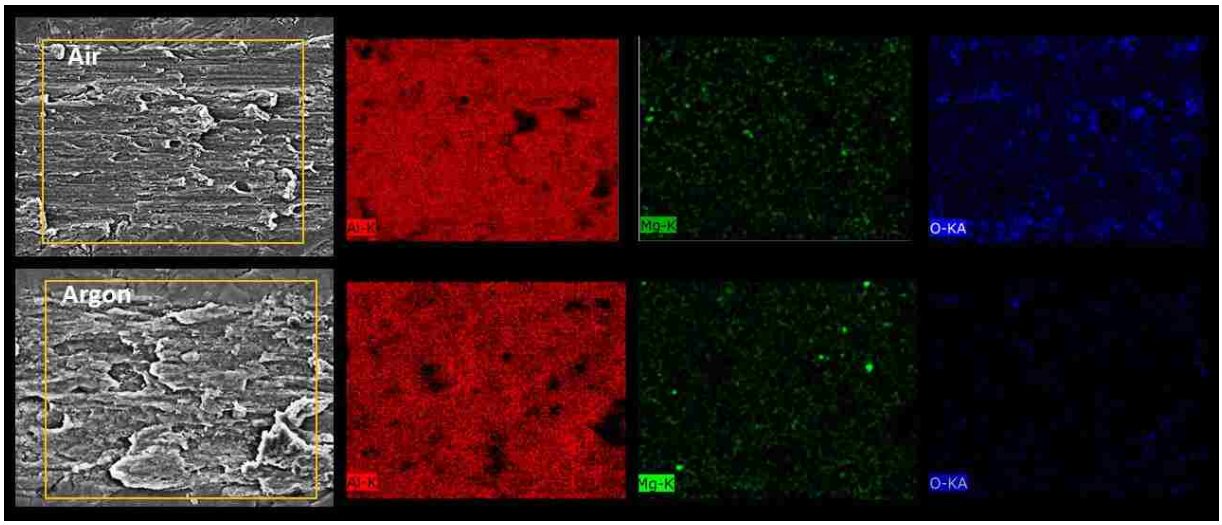

Figure 5.14 EDS maps of the elements, Al, Mg, O, found on the sliding track on polished AA6061 alloy after testing against P20 steel pin in air and argon atmosphere. The images on the column (a) are the SE images of the sliding track, column (b) (c) (d) are element maps of Al, Mg, O.

CHAPTER 6: SUMMARY AND RECOMMENDATIONS

6.1 Summary

Simulated hot forming and junction strength experiments were conducted using aluminum alloy AA6061 to study the tribological behaviour at elevated temperatures. Studies included the effect of deformation mechanisms on the friction behaviour, the effect of atmosphere on the tribological behaviour, and the effect of surface conditions during high temperature deformation. The results can be summarised as follows:

1. Friction experiments conducted on AA6061 strips showed that the COF increased with increasing the temperature and strain rate both in air and argon.
2. The mean COF value measured in argon environment at each temperature was higher than that in air for both tribolayer covered (COF increased by 5%) and polished samples.
3. The measured COF values were plotted with respect to temperature and strain rate to establish COF-DMM that represent the general relationship between the tribological behaviour and mechanisms controlling deformation under the present experimental conditions. Three deformation mechanisms were identified: (i) diffusional flow, (ii) grain boundary sliding (GBS) and (iii) dislocation creep, which were induced in the temperature range of 350^{o}C to 545^{o}C and strain rate range of $1x10^{-2}$ to $4x10^{-2}s^{-1}$.
4. GBS increased with increasing temperature and strain rate, resulting in a higher surface roughness, and higher COF, due to the grain steps formed on at the grain boundaries on the surface.
5. Low average roughness reduced COF in diffusional flow and dislocation creep region.

6. In air, for AA6061 at high temperature (>450^{o}C), the formation of GBS-induced steps on the surface led to the formation of superplastic fibres with 1- 3 μm length and a length-to-diameter ratio of 19. At low temperatures (<400^{o}C), surface oxide cracks formed along the grain boundaries and normal to tensile direction, few fractured oxide fibres could be observed within the cracks.
7. The fraction of surface covered by the fibres was calculated at 545^{o}C and $4x10^{-2}s^{-1}$, which was 17%. This value is smaller than the reported value (42%) [62] on 4.5% Mg alloy (AA5083) at the same experimental conditions. This is due to the larger grain size of AA6061 (20 ± 3.4μm) than AA5083 (5 ± 2.5μm) and smaller Mg content than AA5083 (1.2% Mg for AA6061, 4.5% Mg for AA5083). As a result, less GBS occurred in AA6061 than AA5083, and less Mg diffused to the surface to facilitate the oxide fibres' formation.
8. In argon, no oxide fibre were observed on samples undergone a plastic deformation in the 350 – 545^{o}C range and at 0.04 s^{-1}. High temperature and the initiation of GBS would facilitate the diffusion of Mg to free surface, however, by the absence of oxygen the diffused Mg on the free surface cannot form fibre-like oxide under the applied plastic strain.
9. Magnesium oxides were observed on the contact surface during junction strength tests and indicated that the adhesion force of Al-Mg alloys depends on the alloy's magnesium content. The junction strength between the Al-Mg alloys and steel counterface decreased as the magnesium content of the alloy increased.
10. The junction strength of AA6061 in argon is higher than that measured in air as no oxide layer was formed on the surface of alloy. This was consistent with the higher COF values obtained in argon.

6.2 Recommendations for future work

1. In-situ observation can be introduced in junction strength tests to systematically study the oxide formation on the interface and the effect of the atmosphere and magnesium content of aluminum alloys on their adhesion to steel die surfaces.

2. The experiments can be extended to study the friction behaviour for another experimental working window where different coating/solid lubricants can be applied on the pin material and alloy's surface. Extension of the work would help to optimise the selection of the coatings and solid lubricants.

3. The junction strength experimental set up can be used to study the effect of oxide fibre formation on the reduction of the junction strength. This work would give more understanding of how the oxide fibres effect on the tribological behaviour at elevated temperatures.

LIST OF REFERENCES

[1] M. Merklein, J. Lechler, Investigation of the thermo-mechanical properties of hot stamping steels, Journal of Materials Processing Technology, 177 (2006) 452-455.

[2] M.P. Groover, Fundamentals of modern manufacturing: materials processes, and systems, John Wiley & Sons, 2007.

[3] H. Le, M. Sutcliffe, J. Williams, Friction and material transfer in micro-scale sliding contact between aluminium alloy and steel, Tribology Letters, 18 (2005) 99-104.

[4] G.E. Dieter, Mechanical metallurgy, (2015).

[5] H.R. Shakeri, Superplastic forming of Aluminium alloys: Report, (2004).

[6] P. Krajewski, Research opportunities for automotive superplastic forming alloys, Advances in Superplasticity and Superplastic Forming, Charlotte, NC. ed, (2004) 173-183.

[7] A. Gholinia, F. Humphreys, P. Prangnell, Production of ultra-fine grain microstructures in Al–Mg alloys by coventional rolling, Acta materialia, 50 (2002) 4461-4476.

[8] Z. Horita, M. Furukawa, M. Nemoto, A. Barnes, T. Langdon, Superplastic forming at high strain rates after severe plastic deformation, Acta Materialia, 48 (2000) 3633-3640.

[9] H. McQueen, The production and utility of recovered dislocation substructures, Metallurgical Transactions A, 8 (1977) 807-824.

[10] M.D. Hanna, Tribological evaluation of aluminum and magnesium sheet forming at high temperatures, Wear, 267 (2009) 1046-1050.

[11] P.E. Krajewski, A.T. Morales, Tribological issues during quick plastic forming, Journal of materials engineering and performance, 13 (2004) 700-709.

[12] M.S. Rashid, C. Kim, E.F. Ryntz, F.I. Saunders, R. Verma, S. Kim, Quick plastic forming of aluminum alloy sheet metal, US Patent US6253588 B1, 2001.

[13] J.G. Schroth, General Motors' quick plastic forming process, Advances in Superplasticity and Superplastic Forming, 9 (2004).

[14] J. McFarlane, D. Tabor, Adhesion of solids and the effect of surface films, Proceedings of the Royal Society of London A: Mathematical, Physical and Engineering Sciences, The Royal Society, 1950, pp. 224-243.

[15] D. Tabor, The Friction and Lubrication of solids, Oxford University Press, Oxford), I, 1950.

[16] M. Zayan, O. Jamjoom, N. Razik, High-temperature oxidation of Al-Mg alloys, Oxidation of Metals, 34 (1990) 323-333.
[17] A. Morales, Evaluation of Die Coatings for Superplastic Forming Processes, March, 2004, pp. 14-18.
[18] P.E. Krajewski, Lubrication system for hot forming, US Patent US5819572 A, 1998.
[19] J. Edwards, Coating and surface treatment systems for metals: a comprehensive guide to selection, (1997).
[20] T. Nieh, J. Wadsworth, 0. D. Sherby: Superplasticity in Metals and Ceramics, Cambridge University Press, Cambridge, United Kingdom, 1997.
[21] F.K. Abu-Farha, M.K. Khraisheh, An integrated approach to the superplastic forming of lightweight alloys: towards sustainable manufacturing, International Journal of Sustainable Manufacturing, 1 (2008) 18-40.
[22] S. Han, The influence of tool geometry on friction behavior in sheet metal forming, Journal of materials processing technology, 63 (1997) 129-133.
[23] P.L. Menezes, K. Kumar, S.V. Kailas, Influence of friction during forming processes—a study using a numerical simulation technique, The International Journal of Advanced Manufacturing Technology, 40 (2009) 1067-1076.
[24] P. Carlsson, Surface engineering in sheet metal forming, (2005).
[25] O. Gali, A. Riahi, A. Alpas, The tribological behaviour of AA5083 alloy plastically deformed at warm forming temperatures, Wear, 302 (2013) 1257-1267.
[26] S. Das, A. Morales, A. Riahi, X. Meng-Burany, A. Alpas, Role of plastic deformation on elevated temperature tribological behavior of an Al-Mg alloy (AA5083): a friction mapping approach, Metallurgical and Materials Transactions A, 42 (2011) 2384-2401.
[27] J. McFarlane, D. Tabor, Relation between friction and adhesion, Proceedings of the Royal Society of London A: Mathematical, Physical and Engineering Sciences, The Royal Society, 1950, pp. 244-253.
[28] A.T. Gwathmey, H. Leidheiser, G.P. Smith, Influence of crystal plane and surrounding atmosphere on chemical activities of single crystals of metals, (1948).
[29] R. Holm, B. Kirschstein, Über das Haften zweier Metallflächen aneinander im Vakuum und die Herabsetzung des Haftens durch gewisse Gase, Wissenschaftliche Veröffentlichungen aus den Siemens-Werken, Springer, 1936, pp. 122-127.

[30] B. Podgornik, S. Hogmark, O. Sandberg, Influence of surface roughness and coating type on the galling properties of coated forming tool steel, Surface and Coatings Technology, 184 (2004) 338-348.
[31] O. Gali, A. Riahi, A. Alpas, The effect of surface conditions on the elevated temperature sliding contact deformation of AA5083 alloy, Wear, 330 (2015) 309-319.
[32] G.E. Totten, D.S. MacKenzie, Handbook of Aluminum: Vol. 1: Physical Metallurgy and Processes, CRC Press, 2003.
[33] M. Kassner, M.-T. Pérez-Prado, Five-power-law creep in single phase metals and alloys, Progress in Materials Science, 45 (2000) 1-102.
[34] O.D. Sherby, J. Wadsworth, Superplasticity—recent advances and future directions, Progress in Materials Science, 33 (1989) 169-221.
[35] F. Nabarro, Deformation of crystals by the motion of single ions, Report of a Conference on Strength of Solids, 1948, pp. 75-90.
[36] M. Ashby, R. Verrall, Diffusion-accommodated flow and superplasticity, Acta Metallurgica, 21 (1973) 149-163.
[37] H. Lüthy, R.A. White, O.D. Sherby, Grain boundary sliding and deformation mechanism maps, Materials Science and Engineering, 39 (1979) 211-216.
[38] G.E. Deiter, Mechanical metallurgy, McGraw-Hill, (1986) 221-227.
[39] A. Ball, M. Hutchison, Superplasticity in the aluminium–zinc eutectoid, Metal Science, 3 (1969) 1-7.
[40] J. Fisher, On the strength of solid solution alloys, Acta metallurgica, 2 (1954) 9-10.
[41] A. Cottrell, M. Jaswon, Distribution of solute atoms round a slow dislocation, Proceedings of the Royal Society of London A: Mathematical, Physical and Engineering Sciences, The Royal Society, 1949, pp. 104-114.
[42] H.J. Frost, M.F. Ashby, Deformation mechanism maps: the plasticity and creep of metals and ceramics, (1982).
[43] W.-J. Kim, E. Taleff, O.D. Sherby, A proposed deformation mechanism for high strain-rate superplasticity, Scripta metallurgica et materialia, 32 (1995) 1625-1630.
[44] C. Herring, Diffusional viscosity of a polycrystalline solid, Journal of applied physics, 21 (1950) 437-445.

[45] G. Requena, D. Telfser, C. Hörist, H. Degischer, Creep behaviour of AA 6061 metal matrix composite alloy and AA 6061, Materials science and technology, 18 (2002) 515-521.
[46] A. Khamei, K. Dehghani, R. Mahmudi, Modeling the Hot Ductility of AA6061 Aluminum Alloy After Severe Plastic Deformation, JOM, 67 (2015) 966-972.
[47] M. Frolish, J.C. Walker, C. Jiao, W. Rainforth, J. Beynon, Formation and structure of a subsurface layer in hot rolled aluminium alloy AA3104 transfer bar, Tribology international, 38 (2006) 1050-1058.
[48] R. Ambat, A.J. Davenport, A. Afseth, G. Scamans, Electrochemical behavior of the active surface layer on rolled aluminum alloy sheet, Journal of the Electrochemical Society, 151 (2004) B53-B58.
[49] X. Zhou, Y. Liu, G. Thompson, G. Scamans, P. Skeldon, J. Hunter, Near-surface deformed layers on rolled aluminum alloys, Metallurgical and Materials Transactions A, 42 (2011) 1373-1385.
[50] M. Fishkis, J. Lin, Formation and evolution of a subsurface layer in a metalworking process, Wear, 206 (1997) 156-170.
[51] G. Buytaert, H. Terryn, S. Van Gils, B. Kernig, B. Grzemba, M. Mertens, Study of the near-surface of hot-and cold-rolled AlMg0. 5 aluminium alloy, Surface and interface analysis, 37 (2005) 534-543.
[52] M. Frolish, M. Krzyzanowski, W. Rainforth, J. Beynon, Oxide scale behaviour on aluminium and steel under hot working conditions, Journal of Materials Processing Technology, 177 (2006) 36-40.
[53] K. Li, X.R. Zhou, G.E. Thompson, J.A. Hunter, Y.D. Yuan, Evolution of Near-Surface Deformed Layers on AA3104 Aluminium Alloy, Materials Science Forum, Trans Tech Publ, 2013, pp. 358-362.
[54] G. Scamans, Shear processing of aluminium alloy surfaces and its influence on corrosion, Aluminium International Today, 19 (2007) 26.
[55] X. Xia, Precipitation and recrystallization in Al-Mn AA3104 alloy, Scripta metallurgica et materialia, 28 (1993) 1213-1218.

[56] L. Philippe, H. Terryn, J. de Wit, L. Katgerman, Understanding the electrochemical, microstructural and morphological changes during hot rolling from a corrosion perspective, Surface and Coatings Technology, 201 (2006) 828-834.
[57] C. Lea, J. Ball, The oxidation of rolled and heat treated Al-Mg alloys, Applications of Surface Science, 17 (1984) 344-362.
[58] K. Holub, L. Matienzo, Magnesium diffusion in several aluminum alloys, Applications of Surface Science, 9 (1981) 22-38.
[59] A. Riahi, A. Edrisy, A. Alpas, Effect of magnesium content on the high temperature adhesion of Al–Mg alloys to steel surfaces, Surface and Coatings Technology, 203 (2009) 2030-2035.
[60] M. Schütze, Protective oxide scales and their breakdown, Wiley, 1997.
[61] S. Das, Plastic Deformation and Surface Damage Mechanisms during Hot-forming of Al and Mg Alloy Sheets, (2011).
[62] S. Das, A. Riahi, X. Meng-Burany, A. Morales, A. Alpas, High temperature deformation and fracture of tribo-layers on the surface of AA5083 sheet aluminum–magnesium alloy, Materials Science and Engineering: A, 531 (2012) 76-83.
[63] S. McFadden, R.S. Mishra, R. Valiev, A. Zhilyaev, A. Mukherjee, Low-temperature superplasticity in nanostructured nickel and metal alloys, Nature, 398 (1999) 684-686.
[64] H. Gleiter, Nanocrystalline materials, Progress in Materials Science, 33 (1989) 223-315.
[65] F.A. Mohamed, H. Yang, Deformation mechanisms in nanocrystalline materials, Metallurgical and Materials Transactions A, 41 (2010) 823-837.
[66] F. Czerwinski, The oxidation behaviour of an AZ91D magnesium alloy at high temperatures, Acta Materialia, 50 (2002) 2639-2654.
[67] M. Banares, I. Wachs, Molecular structures of supported metal oxide catalysts under different environments, Journal of Raman Spectroscopy, 33 (2002) 359-380.
[68] H.-K. Oh, K.-H. Yeon, H.Y. Kim, The influence of atmospheric humidity on the friction and wear of carbon steels, Journal of Materials Processing Technology, 95 (1999) 10-16.
[69] D. Kim, T. Fischer, B. Gallois, The effects of oxygen and humidity on friction and wear of diamond-like carbon films, Surface and Coatings Technology, 49 (1991) 537-542.

[70] W. Cao, X. Lu, H. Conrad, Whisker formation and the mechanism of superplastic deformation, Acta materialia, 44 (1996) 697-706.
[71] Y. Takayama, T. Tozawa, H. Kato, Superplasticity and thickness of liquid phase in the vicinity of solidus temperature in a 7475 aluminum alloy, Acta materialia, 47 (1999) 1263-1270.
[72] W. Shaw, The role of microsuperplastic flow in high temperature fracture of AL-9021 mechanically alloyed aluminium, Journal of materials science, 24 (1989) 4114-4119.
[73] M. Zelin, On micro-superplasticity, Acta materialia, 45 (1997) 3533-3542.
[74] C. Constantinou, M.M. Chaudhri, Optical observations of "junction growth" in asperities of copper, aluminium, PTFE and nylon under combined normal and tangential stresses, Journal of materials science, 24 (1989) 4279-4292.

VITA AUCTORIS

NAME: Zeyuan Cui

PLACE OF BIRTH: Luoyang, Henan

YEAR OF BIRTH: 1988

EDUCATION: Anyang normal university, Henan
2008 – 2012 B.Sc.
University of Windsor, Windsor, Ontario
2014-2016 M.Sc.